The agglomeration of fine iron particles in a fluidised bed cascade

Daniel Laurence Blundell
University of Wollongong

THE AGGLOMERATION OF FINE IRON PARTICLES IN A FLUIDISED BED CASCADE

A thesis submitted in fulfilment of the
requirements for the award of the degree

DOCTOR OF PHILOSOPHY

from

UNIVERSITY OF WOLLONGONG

by

Daniel Laurence Blundell

DEPT. OF MECHANICS, MATERIALS AND MECHATRONICS

2005

THESIS CERTIFICATION

I, Daniel Laurence Blundell, declare that this thesis, submitted in fulfilment of the requirements for the award of Doctor of Philosophy, in the Department of Mechanics, Materials and Mechatronics, University of Wollongong, is wholly my own work unless otherwise referenced or acknowledged. The document has not been submitted for qualifications at any other academic institution.

Daniel Laurence Blundell

23rd September 2005

Table of Contents

Lists of Figures

List of Tables

List of Abbreviations

AFM:	Atomic Force Microscopy
BCC:	Body Centred Cubic
CPA:	Coupled Plasmon Approach
DMT:	Derjaguin-Muller-Toporov
DRI:	Directly Reduced Iron
FCC:	Face Centred Cubic
FIB:	Focused Ion Beam
Gleeble:	Gleeble Thermo-mechanical Simulator
HBI:	Hot Briquette Iron
HLSCM:	High temperature Laser Scanning Confocal Microscopy
JIC:	Jump Into Contact
JKR:	Johnson-Kendall-Roberts
MSD:	Multiple Scratch Decay
SEM:	Scanning Electron Microscope
SSD:	Single Scratch Decay
TEM:	Transmission Electron Microscope
vdW:	van der Waal's

Abstract

The research topic presented here is that of the tendency of iron ore particles in a fluidized bed reactor during the DRI process, to form agglomerates, giving rise to sticking of iron ore particles resulting in the defluidisation of fluidised bed iron ore reactors. The particles are capable of sticking to one another, to reactor walls, and to adhere to the interior of standpipes, as they pass from one reactor bed to another.

The general mechanism of the agglomeration of fine iron ore particles is by sintering. A study of the sticking of iron ore particles has been conducted by delineating the sub-mechanisms involved in sintering such as van der Waal's adhesion and surface diffusion, and endeavouring to quantify these attributes for iron.

In this study, van der Waal's forces and the work of adhesion for iron surfaces in contact has been evaluated using atomic force microscopy. It was shown that the pressure exerted at a local infinitesimal point on one iron particle by another was higher than the yield stress of iron and probably leads to plastic deformation of the surface, giving rise to large contact areas between them.

In this study, a new and more efficient technique of quantifying surface diffusion rates in metals has been developed using confocal microscopy and ion beam milling. Surface diffusion rates in iron were measured and benchmarked against earlier quantities. The new quantities compared well with the old values, considering the difficulty involved in repeating surface diffusion experiments.

It was found that quantities of carbon higher than 0.5%C led to a 100-fold decrease in surface diffusion rates. It is concluded that high carbon content will retard the transport of iron material to a contact site between two particles.

A high-temperature sticking test was developed in this study to test and quantify observations made at BHP-Billiton. It was found that in commercial carbon-steel conforming to a carbon content of approximately 0.8%C, a distinct difference exists between sticking quantities of contacts made below and above the eutectoid temperature. Sticking stress was observed to be higher above the eutectoid temperature and it is inferred that the gamma phase of iron is highly susceptible to sticking. This is in contrast to the high carbon steel. It is shown here that Fe-1.5%C steel shows less potential to stick. Iron powders from port Hedland showing minimal sticking are covered in a thin layer of cementite. Thus, the low sticking strength of the high carbon steel is probably due to its content of cementite.

Sintering diagrams were constructed for iron to study the combined effect of surface diffusion and van der Waal's adhesion between iron particles. Two main insights were gained from this. Firstly, the potential to form inter-particle contacts via van der Waal's adhesion were not constant with temperature and would vary according to the change in plastic yield strength. It was found that over all that inter-particle contacts grew larger with increasing temperature. Secondly, van der Waal's adhesive properties were more significant when operating on smaller sub-micron particle contacts. In larger particles, the formation of inter-particle contacts relies more of the rates of surface diffusion.

Acknowledgments

I would firstly like to thank Professor Rian Dippenaar who has been what I could only describe as the most generous supervisor one could hope for in terms of his time and attention to his supervisory role. Professor Dippenaar has, during the course of this thesis, provided input, guidance and feedback of incalculable value. Professor Dippenaar has also been exemplary, as an academic role model to myself, upholding the true spirit of science and academic research in a world where economic rationalism is eroding these principles away. He has also assisted me in becoming properly familiar with the relevant metallurgical background knowledge, vital to the completion of this thesis.

I would like to thank BHP-Billiton for providing this thesis topic, for allowing me access to confidential information and for providing partial funding to this project. In particular I would like to thank my industry supervisor Dr. Tom Honeyands for his guidance and useful discussions during this project and for acting as a liaison to the various departments of research and people at BHP-Billiton laboratories. I would also like to thank Damien O'Dea and Dean Crawford at BHP-Billiton for providing useful discussions and information to me during this project.

A special thanks is extended to Mark Reid for his generous input of time in assisting me in various experiments during my thesis and for useful tips and advice from his extensive knowledge and experience.

Thank you to Dominic Phelan for useful discussions and advice on various matters relating to experiments and metallurgical theory.

Thanks also go to Lorelle Pollard in the Faculty of Engineering administration for being continually helpful in administrative matters and the endless paperwork that is associated with undergoing a PhD. Lorelle has always been diligent in providing information to the staff and students on their rights and resources available to them.

Finally, I would like to acknowledge Sandrine Therese for her love and support during this thesis. To her I owe my sanity and my disposition of being less agitated than I once was.

Chapter 1:

Agglomeration of Iron Ore Particles in a Fluidised Bed Cascade

Introduction and Overview

Chapter 1: Agglomeration of Iron Ore Particles in a Fluidised Bed Cascade- Introduction and Overview

1. Introduction

Australia is a major exporter of fine iron ore and BHP-Billiton has constructed what was to become the world's largest merchant plant to produce directly reduced iron (DRI) from fine iron ores in the form of hot briquetted iron (HBI) at Port Hedland in Western Australia. The first briquettes were produced on 18 February 1999 and the first cargo of 22 500 tones of HBI was shipped to POSCO in Korea on 10 May 1999. The HBI produced at Port Hedland through the FINMET™ production route is primarily aimed at supplying the Asian electric arc furnace steel-making sector with low residual feedstock but it is also well suited to use as a coolant in the Basic Oxygen Furnace. HBI is also produced by the FINMET™ production route in Venezuela by the ORINOCO Iron joint venture (a joint venture between BHP-Billiton and the Venezuelan companies Sivensa and Ferrominera Orinoco). The output from this plant will supply US and European steel making markets.[1]

The process of HBI iron ore reduction has the associated problem of the agglomeration of iron ore particles leading to defluidisation of the reactor, and has been an issue in this type of DRI production for many years. Inside fluidized bed reactors, agglomeration, leading to sticking of iron ore particles, has caused serious economic and technological set-backs, acting as a barrier to this technology reaching its full potential.

The research topic presented here is that of the tendency of iron ore particles in a fluidized bed reactor during the DRI process, to form agglomerates, giving rise to

sticking of iron ore particles resulting in the defluidisation of fluidised bed iron ore reactors. The particles are capable of sticking to one another, to reactor walls, and to adhere to the interior of standpipes, as they pass from one reactor bed to another [2-4].

The phenomenon of sticking has been observed in DRI plants in general, including the FINMET™ [1] plant in Port Hedland, Western Australia, and in the FIOR™ [2] plant in Puerto Ordaz, Venezuela.

Various authors have studied the sticking phenomenon and its characteristics and have proposed some solutions to preventing it [5-8]. The study by Gransden and Sheasby [6], showed some evidence to suggest that sticking of iron ore particles during reduction is related to sintering of pure iron surfaces, and will occur generally at temperatures above 600^0C.

It is observed by some authors that particle sticking will be favoured by smaller ore particle size [8], and it is argued that the smaller particles with a larger surface area per unit volume will produce a greater potential for contact[9]. Special attention might therefore be directed towards the surface properties of the particles in the future.

Smaller wustite (FeO) particles coupled with an optimal partial pressure of carbon monoxide when reduced, favour the growth of what are known as “whisker” growth. These are near nano-scale tendril like structures growing on the iron’s surface during reduction. Both whisker growth and sticking it is thought, are related to sintering.[7]

The problem of defluidisation of iron ore reactors is not new. Studies of this phenomenon extend back over forty years [5, 7, 8, 10-13]. The disparate variables

involved, make the issue complex. Some key questions posed in the past are (but not exclusively), “Under what thermodynamic, atmospheric and chemical conditions does the bed defluidise? “What is the mechanism of sticking itself?” “What are the associated surface properties of the ore particles in defluidisation?” These questions have inspired approaches to this problem from many points of view, from experts of a variety of backgrounds (not necessarily all in agreement).

The different angles of approach to this study have ranged from geological perspectives, [14, 15] being the study of the various ore types that display a high propensity to stick during reduction. There are those who have studied how thermodynamic parameters, [6] reaction kinetics [7, 16] and chemistries of the reducing gases, and additives, [5, 12, 17] affect the agglomeration of fine particles or “sticking”. There are studies that have been conducted on surface morphologies, [18] and surface formations [7, 19] during reduction in an attempt to identify the controlling mechanism of sticking. The experts involved in these studies have come from a range of backgrounds, including metallurgists, applied chemists, materials engineers and solid-state physicists.

The scientists involved also have come from different points of view as to what kind of research will provide clarification of the issues. concerned The two main "schisms", in this respect are those who see an engineering solution to the problem, (that is to say, selecting the correct reactor conditions and/or building a more efficient reactor in some way), and those who believe a solution lies in a fundamental understanding of iron ore reduction and sticking behaviour. The ultimate solution to the sticking problem is likely to come from a synthesis of these two points of view.

It must be understood that much of the disagreement amongst researchers and engineers comes in the face of a problem of overwhelming complexity. It is a common reaction of those studying such a complex topic to hold on to a particular school of thought, believing that thermodynamics, say, or understanding reaction chemistry, will ultimately point the way to a solution. This approach has not, and will not work. During the undertaking of this study, it has become clear that a solution to this problem requires more than just a novel approach. Its solution will be firmly rooted in an interdisciplinary endeavour.

This thesis has not been concerned so much with tying together techniques from various disciplines. The concern of this thesis has been to derive some fundamental concepts and properties of the sticking phenomena of iron particles. Fundamental measurements have been made in a simplified, well-defined system of iron and iron-carbon alloy surfaces with respect to matter transport, physical properties and inter-atomic and molecular forces that are significant when two surfaces are brought into close contact.

The general phenomena of sticking and related problems in HBI production via the DRI process is not well understood, even to this day. Above is an introduction to the basic principle of the issue, and the activity in this area. In the chapter that follows, a more developed overview of the problem, from first principles and experimental research to the mechanism of sticking itself, will be presented.

Chapter 2:

Literature Review

Chapter 2: Literature review

2. Introduction

This review aims to summarise and present the topic of iron ore reduction in relation to the agglomeration of iron ore particles in a fluidised bed reactor, leading to a defluidisation of the reactor. Presented in this review, is an introduction to the topic up to the point of commencing this thesis, as it is experienced in the fluidised bed reactor in Port Hedland in Western Australia. In order to gain perspective and put into context previous work on the subject, a brief history of the past fifty years in iron ore reduction and its evolution of relevance to the current study is presented.

Included is a discussion of defluidisation itself, the central phenomena resulting from agglomeration. The work done so far by previous authors has revealed that agglomeration is closely related to whisker growth and the sintering of fine micron and sub-micron iron ore particles. Despite much research in this area, the exact mechanism leading to sticking of iron ore particles is not well understood.

2.1. A Brief History of DRI

The acquisition of metallic iron through iron ores via solid-state reduction, is the most ancient method of direct reduction, dating back as early as 1300 BC [20]. Since the modern industrial age however, the use of blast furnace technologies has been the predominant method for producing high-grade metallic iron. Economic and technological considerations in the last fifty years, has led iron and steel production

back to directly Reduced Iron (DRI) processes as a viable option for the production of virgin iron units. [20]

The Mexican company Hysla (formerly Hojalota y Lamina S.A), began electric steel making in 1943. The production suffered from a lack of scrap supply and expensive imports from the U.S.A. High quality iron units were required, however because of the company's small scale of production, gas-based reduction of iron ore became a viable option. The Hysla company developed this first functional process in 1957 called HYL I. This hailed the modern era of DRI production. [20]

In 1946, the Midland-Ross corporation, in Toledo, Ohio, started working on new DRI technology using stoichiometric reformers, combined with the shaft furnace process. This research gave rise to the MIDREX® DR process in 1969. [21] The new technologies, (HYL I and MIDREX®) enjoyed great success in the 1970s, and new plants were erected in many parts of the world, especially in developing countries. [20]

DRI production grew from 0.7 mega tones (Mt) in 1970 to 7 Mt in 1980. This growth plateaus between 1980 and 1987 due to an economic recession in the U.S.A. Toward the end of this recession, the world steel production was again on the increase. Higher rates of scrap metal production from standard mills forced an increased need for DRI, that utilises the scrap. [20]

DRI, produced with inexpensive natural gases, can provide an economical solution to iron and steel manufacturers in developing countries. The developing world had an increased need for DRI since the beginning of the 1990s and DRI production was up to

33.3 Mt by 1996 throughout the world. Analysts suggest that DRI production will continue to increase into the future for at least the next five years. [20]

The impressive success of DRI production has had parallel to this success, production problems with production that has been the subject of lively scientific research since its inception.

2.2. Archetypal Iron Ore Reduction Processes

The last fifty fears have seen an evolution of direct reduction processes. An expanded technical dossier will not be given here on each process developed, rather a brief mention of the main types of processes will be indicated. A more complete description of the processes relevant to work in this thesis will be presented however.

Many DRI processes were developed and tested experimentally, but some were not successful, the successful prototypes have been developed into full-scale commercially viable concepts, and, due to a balance of technical and economic factors, a number of DRI production processes are in use today. [22]

In general, there are two main categories of DRI processing techniques, coal-based reduction and gas-based reduction. [22]

Coal based reduction processes represent a group of DRI techniques, the subset of which are the retort and rotary kiln reactors. [22, 23]. Gas-based processes also house a subset of process technologies, of which shaft reactors and fluidised bed reactors are probably the most important[23]. Whereas shaft reactors such as those used in the

MIREX process require pelletised feedstock, the fluidized-bed reactors are designed to produce DRI from iron ore fines.

2.2.1. Fluidised Bed Reactors

With respect to the current study it is the process of fluidised bed (that is gas-based) iron ore reduction technologies that is the focus of continuing study, due to particular problems encountered in these reactors. Thus a closer look at their operation is needed at least to give the reader a contextual overview of the topic.

2.2.2. FIOR™ and FINMET™

The two major fluidised bed DRI technologies developed in the last forty years are the FIOR™ and the FINMET™ processes. [1, 2] The FIOR™ process is no longer in production, but it is pertinent to describe it in some detail as the FINMET™ process is based partially on this design.

The FIOR™ process was first developed by EXXON™ (formerly ESSO) back in the 1960s. [24] The FIOR™ plant was operated by SIVENSA™ at Puerto Ordaz, commissioned in 1976, and was the first commercial fluidised bed DRI plant in the world.

FIOR™ reduces iron ores in the solid-state using high partial pressures of Hydrogen from steam-reformed natural gas to obtain metallic iron. This process is shown schematically in **figure 2.1**. The reduction takes place in four fluidised bed reactor vessels in series called a "fluidised bed cascade". [2, 25]

Reactor R404 is the preheat stage responsible for preheating the ore, in the presence of combustible natural gas. The preheated ore flows via stand pipes, utilising gravity as the driving force to flow the ore through reactors R403 to R401. The ore is reduced in the reactors by counter current flowing hydrogen gas in the temperature range 680^{o}C to 780^{o}C, at a pressure between 10 and 11 bar.

The FINMET™ process produces DRI by reacting fine iron ore with reformed natural gas in a series of fluid bed reactors, based on the flow sheet of the FIOR™ process. [5]

The FINMET™ process has been under development during the 1990s and was brought on line in Australia by the end of the decade. The BHP FINMET™ plant at Port Hedland in Western Australia, produced its first batch of HBI on February 18 1999. [1] BHPs interest in investing in the FINMET™ process was motivated in part by the processes capability to reduce directly fine ores (approximately 6.3mm or less). This is important for the type of ore targeted by BHP for production. [1]

The FINMET™ process is largely a modified version of the FIOR™ process as shown schematically in **figure 2.2**. [1]

Some gangue is removed in the beneficiation plant. The ore is then dried and the feed stock lifted to the top of FINMET® reactor (R1) via a lock hopper system. The ore is then reduced in step-wise fashion in reactor beds R2 to R4 at a pressure between 11 to

13 bar in the temperature range 550°C to 800°C. From there the ore is then made into Hot Iron Briquettes.[1]

The FINMET™ process uses a cascade series of four reactor beds, as does the FIOR™, with the reduction gas flowing counter current to the solids flow.

[1] Studies of the properties of HBI and its sintering has been studied by Wanda Melfo at the BHP Institute of Steel Processing and Products in the University of Wollongong.26. Melfo, W., *Early Sintering Phenomena Pertaining to Hot Briquetted Iron*, in *BHP Institute for Steel Processing and Products*. 2002, University of Wollongong: Wollongong. p. 100. (Masters Thesis).

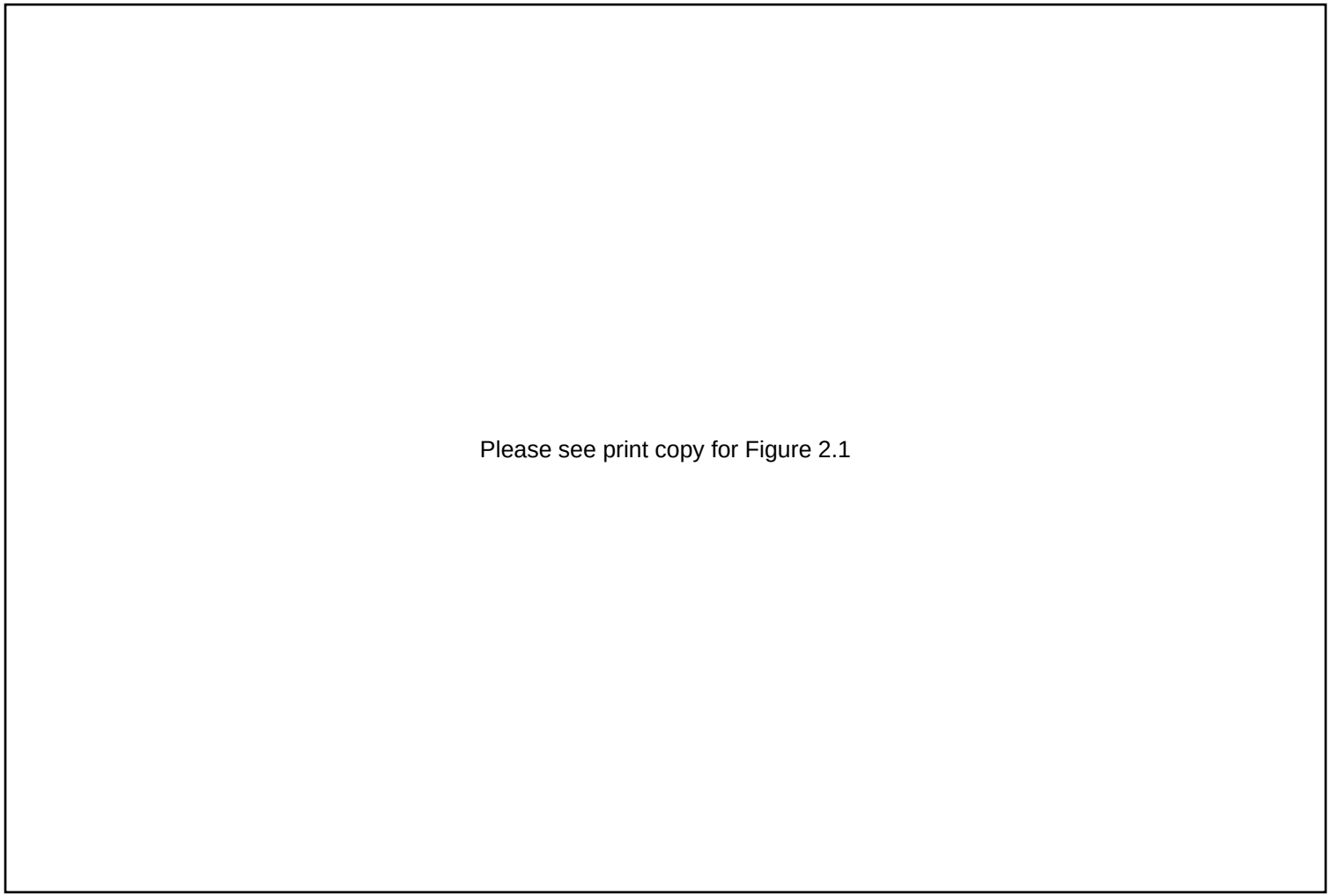

Figure 2.1: Schematic illustration of the FIOR™ process.

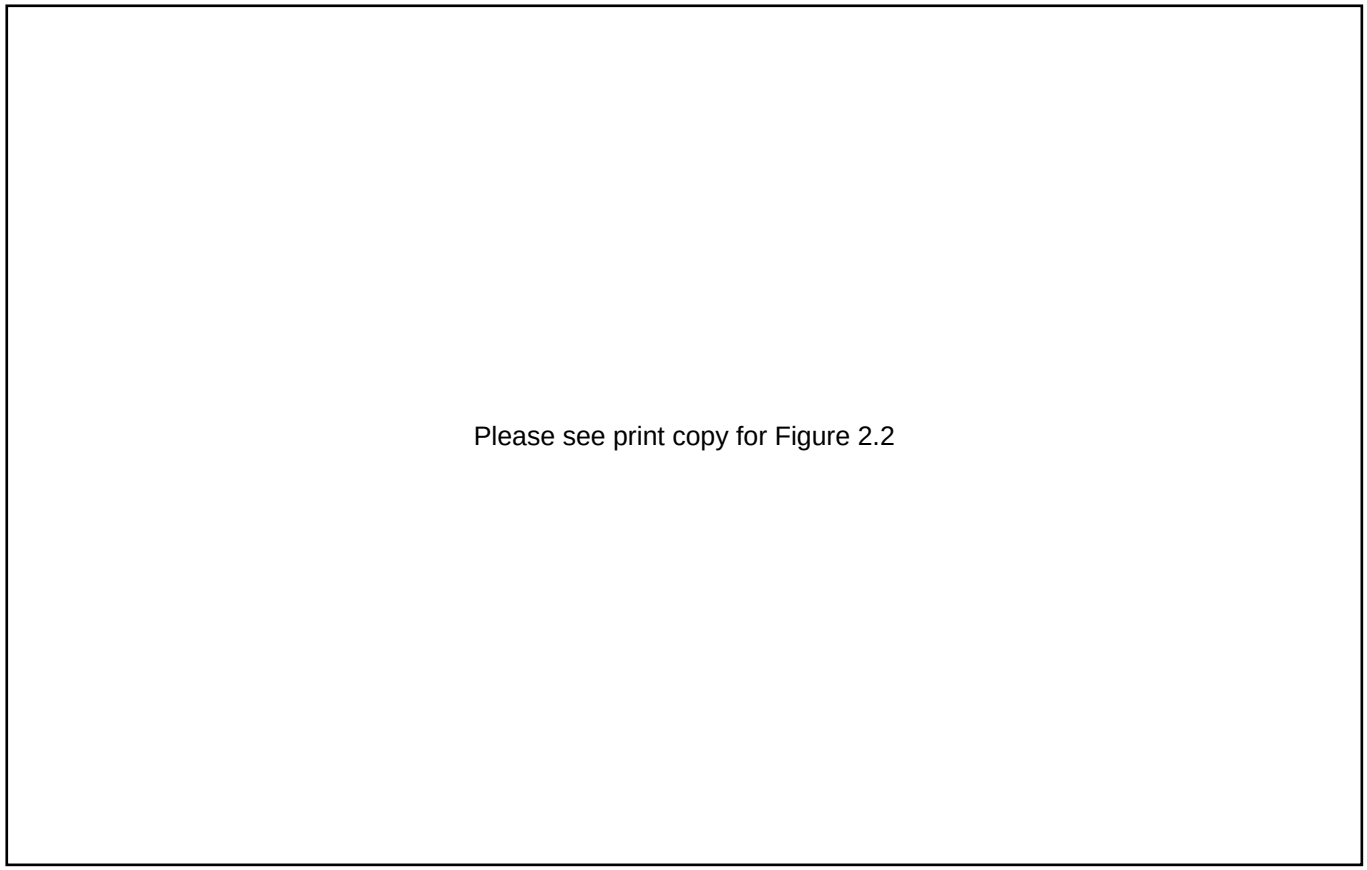

Figure 2.2: Schematic illustration of the FINMET™ process.

The feedstock enters reactor R4 where it is preheated to 550^{o}C-570^{o}C by reducing gases recycled from reactor R3. The ore is passed down from R4 through R3and R2 to R1 counter-current to the flow of reduction gas rich in hydrogen and carbon dioxide (steam reformed gases), reducing the ore to metallic iron from Hematite (Fe_2O_3). The ore is then briquetted at a temperature of approximately 650^{o}C to densities of not less than 5 g/cm^3.

The FINMET™ process is, as mentioned, based on the flow-sheet of the FIOR™ process. It will be of interest then to note the differences between these processes and improvements in the design of the FINMET™ process. The key differences between FIOR™ and FINMET™ have been compiled by Damien O' Dea at BHP laboratories[5], these are:

1. An increased capacity from 400 ktpa to 500 ktpa per reactor module.
2. An increase in the fluidized bed reactor diametre from 3.9 to 4.5 m.
3. Swaging of the freeboard zones of the final two reactors.
4. The use of Mt Newman concentrated hematitic ore as feedstock as opposed to San Isidro Hematitic/Goethitic ore.
5. The use of a reducing gas instead of combusted natural gas to preheat and pre-reduce the ore in reactor R4.
6. An increased CO content of the reducing gas and the inclusion of a CO_2 removal system in the gas recirculation loop.

The focus of the present study is on the final two reactors where the formation of agglomerates is predominant.

2.3. Thermodynamics and Chemistry

It is well established that the efficiency of iron ore reduction is critically dependent on the reducing gas composition and temperature [6, 11, 16, 27]. What is important then, is to present an overview of the thermodynamic factors relevant to this issue.

In direct reduced iron processes, the thermodynamic conditions relevant to the system can generally be "mapped" by phase equilibrium diagrams, depicting the material (or gas) composition as a function of temperature. [28]

In the production of DRI in the former process iron ore reduced to metallic iron but the freshly formed iron is carburised by the carbon-containing reduction gas. Thus, the most important phase diagrams to be considered in our analysis of the process are the Fe-O and the Fe-C, phase diagrams, relevant portions of which are shown in **figures 2.3** and **2.4**.

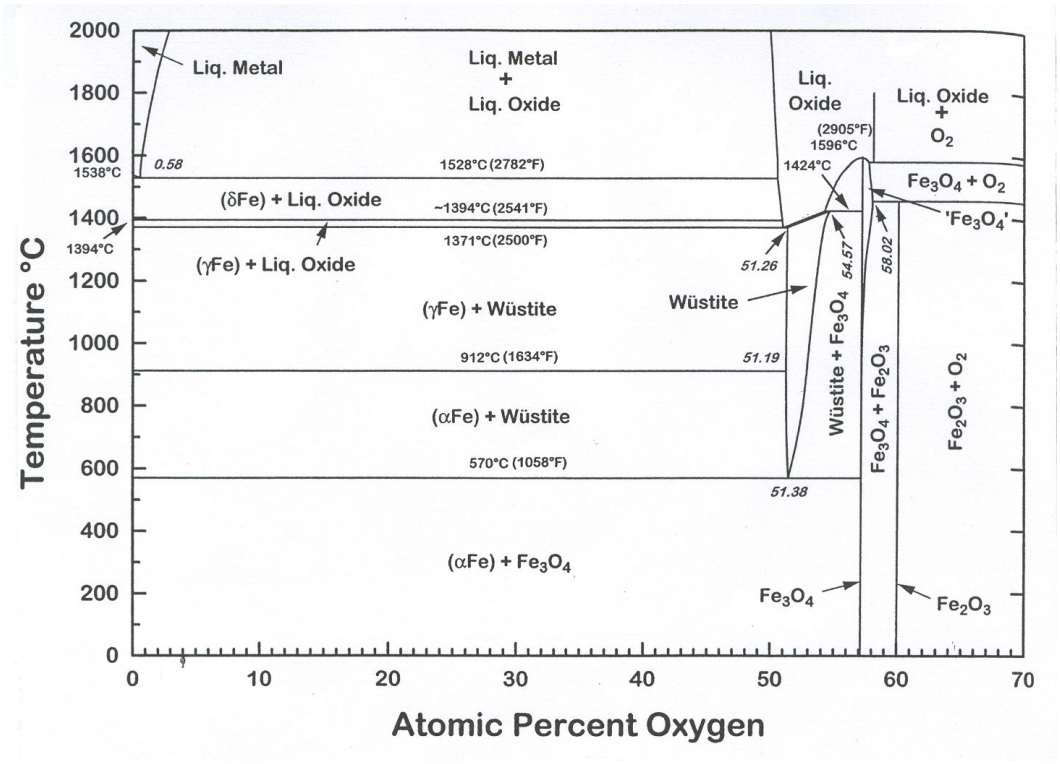

Figure 2.3: The Fe-O phase diagram.

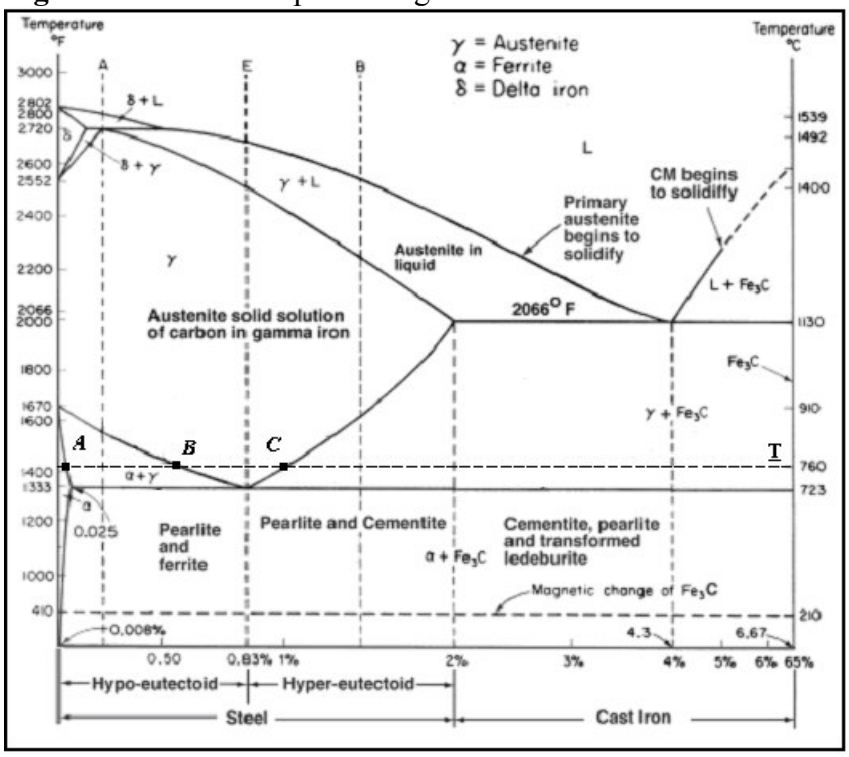

Figure 2.4: The Fe-C phase diagram.

At room temperature, the α-ferrite phase (bcc) of iron is stable. At temperatures of 912°C, pure iron transforms to the austenite phase (γ-ferrite fcc), and on further heating to δ-iron (bcc) at 1394°C [29, 30]. Counter intuitively, the iron oxide system is not actually stoichiometric[2], [31] stoichiometry seeming to be implied by the iron oxide formulas, Hematite (Fe_2O_3), Magnetite (Fe_3O_4) and Wustite (FeO). [29]

There are different oxides of iron that can exist, not all of which are stable at room temperature [29]. Mineral Hematite is stoichiometric and nearly all the Fe is trivalent (Fe^{3+}). Magnetite on the other hand can be composed of both trivalent and divalent (Fe^{2+}) iron ions. It is close to stoichiometric when T< 1000°C. Magnetite is normally not found as a single crystal, having trace elements and inclusions in a spinel structure[29]. However, it can be found in a dense state with few defects[32].

Wustite has an FCC structure with mostly divalent iron ions, but it can have trivalent iron ions also. Thus, Wustite can be written in the form $(Fe_{3x-2}^{2+})(Fe_{2-2x}^{3+})\ O^{2-}$. Wustite is only stable above 570°C. Below this temperature it will decompose to Magnetite and α-ferrite[29].

2.4. Reduction Chemistry

It is generally accepted that the reduction of iron ores proceeds in stages such that [16, 30, 33];

$Fe_2O_3 \rightarrow$	$Fe_3O_4 \rightarrow$	$FeO \rightarrow$	Fe	(2.1).
(Hematite)	(Magnetite)	(Wustite)	(Iron)	

[2] This is due mainly to the presence of cation vacancies and cations in a higher valence state.

The reduction chemistry in principle is straightforward. In the FINMET™ the iron ores are reduced by hydrogen and carbon monoxide gases, produced from reformed natural gas; CH_4 [34, 35].

The basic reactions in the DRI process proceed for T>570°C. The reactions are as follows with standard heats of enthalpy (for T = 1073K); [29] [3]

$$Fe_2O_3(s) + CO(g) \leftrightarrows Fe_3O_4(s) + CO_2(g); \quad \Delta H° = -37.19 \text{ KJ/mol} \qquad (2.2)$$
$$(H_2(g)) \qquad (H_2O(g)); \quad \Delta H° = 83.25 \text{ KJ/mol}$$

$$Fe_3O_4(s) + CO(g) \leftrightarrows FeO(s) + CO_2(g); \quad \Delta H° = 16.42 \text{ JK/mol} \qquad (2.3)$$
$$(H_2(g)) \qquad (H_2O(g)); \quad \Delta H° = 50.46 \text{ JK/mol}$$

$$FeO(s) + CO(g) \leftrightarrows Fe(s) + CO_2(g); \quad \Delta H° = -17.9 \text{ JK/mol} \qquad (2.4)$$
$$(H_2(g)) \qquad (H_2O(g)); \quad \Delta H° = 125.44 \text{ JK/mol}$$

2.5. The Fe-C System

The other system important in DRI is the iron carbide system. Described briefly here, [30]. Consider the Fe-C phase diagram given in **figure 2.4**. At equilibrium, in the presence of solid Carbon, the iron will form a solution of Carbon in Iron. For T> 738°C the Fe-C composition lies in saturation from 0.69% Carbon by mass to 2.4% Carbon by mass on the phase diagram. Iron, found above 723°C (076 %C by mass; the eutectoid temperature) is γ-austenite. For T< 738°C α-ferrite is formed in saturation of Carbon with 0.02% w.t. Carbon.

[3] The reader can note that the ore is reduced in the solid-state.

2.5.1. The Boudouard Reaction

An important reaction that evolves out of the DRI process is the Boudouard reaction. Whether or not reduction takes place is dependent on how this reaction proceeds. The Boudouard reaction is as follows (including standard heat of enthalpy at T=1073K);

$$C(s,v) + CO_2(g) \leftrightarrows 2CO; \qquad \Delta H^\circ = \pm 169.93 \text{ KJ/mol} \qquad (2.5).$$

If the balance of this equation is too far to the left (in excess of 90% say) then reduction will cease.[36]

The reason for this will be explained later. For now, consider the reaction equilibrium constants;[29]

$$\kappa_1 = (\text{Partial Pressure } CO_2)/(\text{Partial Pressure CO}) = (ppCO_2/ppCO) \qquad (2.6)$$

$$\kappa_2 = (\text{Partial Pressure } H_2O)/(\text{Partial Pressure } H_2) = (ppH_2O/pp\ H_2) \qquad (2.7).$$

These are the partial pressures for which reactions (2.2-2.4) are at equilibrium for a given temperature. The reaction for the partial pressure is;[29]

$$CO(g) + H_2O(v) = CO_2(g) + H_2(g) \qquad (2.8).$$

Using Gibbs free energy changes, and common tangent construction [28], the Fe-O phase stability diagram in terms of κ_1 and κ_2 can be constructed, as in **figure 2.5**.

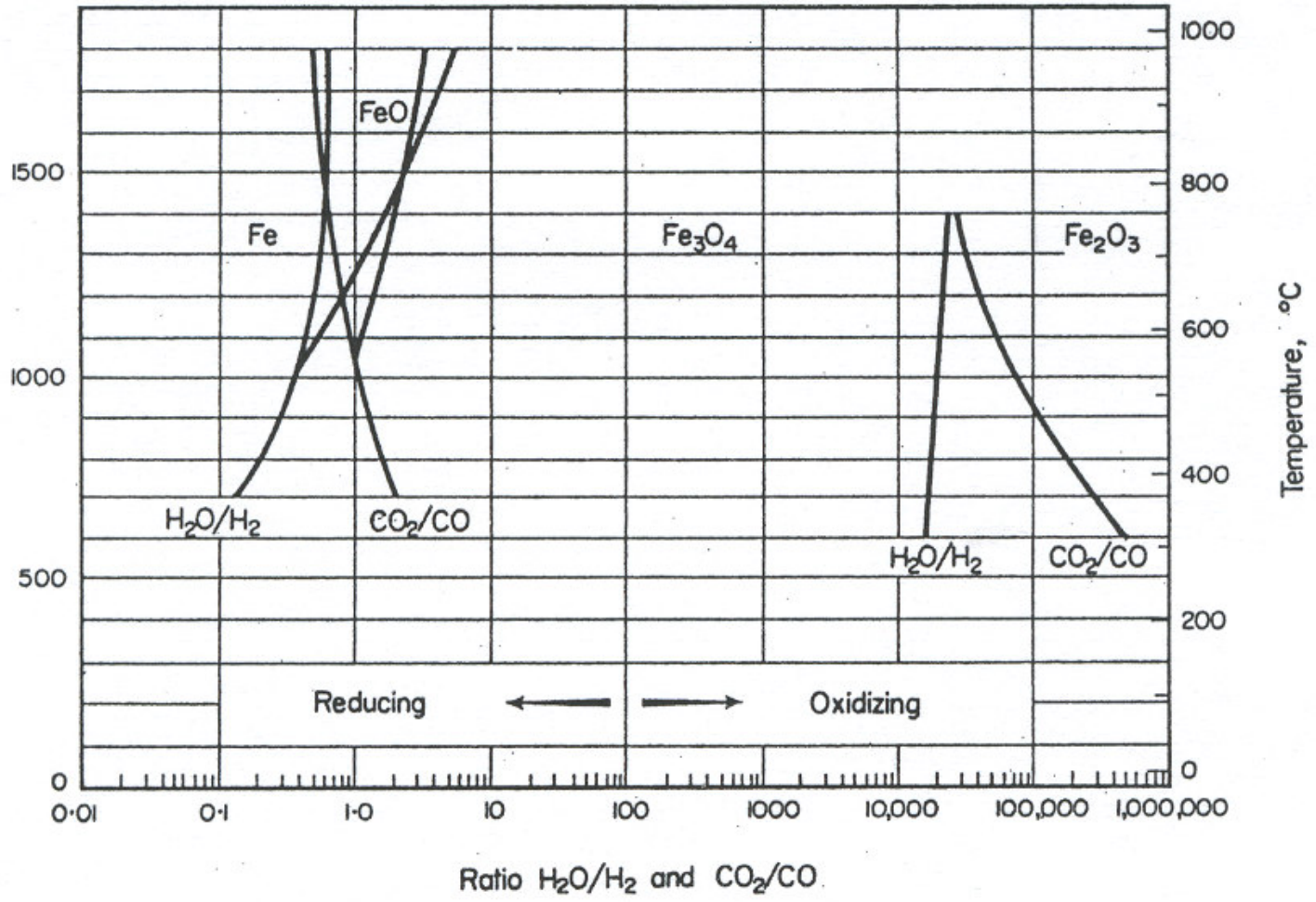

Figure 2.5: The Fe-O phase stability diagram in terms of κ_1 and κ_2.

The partial pressures appearing in equations (2.6 and (2.7) have an effect on whether or not the reaction will proceed, as the stability regions are determined by the CO_2/CO partial pressures. This is also true for the additions of any gases to the process, for instance the addition of N_2, and for the case of CH_4 gas evolving from reactions [29].

2.5.2. Carburisation During Reduction

One result of the Boudouard reaction, is that the free carbon indicated to the left of reaction (3.5), can diffuse into the iron in the solid-state. This is likely to occur during the γ phase as the carbon in much less soluble in the α-iron phase. [29]

Carbon will diffuse into the surface first and build up until saturation point. The carbon will then diffuse from the surface into the bulk towards the center of the particle. The carbon content at the surface will continue to build, establishing a chemical gradient which drives the diffusion of the carbon further into the bulk. [36]

The carbon content can be mapped by weight percent via the iron-carbon phase diagram as in **figure 2.4**.

As temperatures reach above 785°C carbon will readily diffuse from the surface layer into the bulk. When the carbon content exceeds 0.02 w.t % C on the surface, austenite, with a 0.5 w.t. % C content will nucleate and the γ-ferrite-interface advances away from the surface, as a function of time. [25, 28]

When a 0.96 w.t. % C content is reached, cementite (Fe_3C), with a 6.67% w.t. % C will nucleate. A continued diffusion of the carbon into the bulk will allow the Fe_3C phase to

grow in thickness and the Fe_3C/γ-ferrite interface will advance away from the surface with time [28] as can be represented by **figure 2.6**. [25]

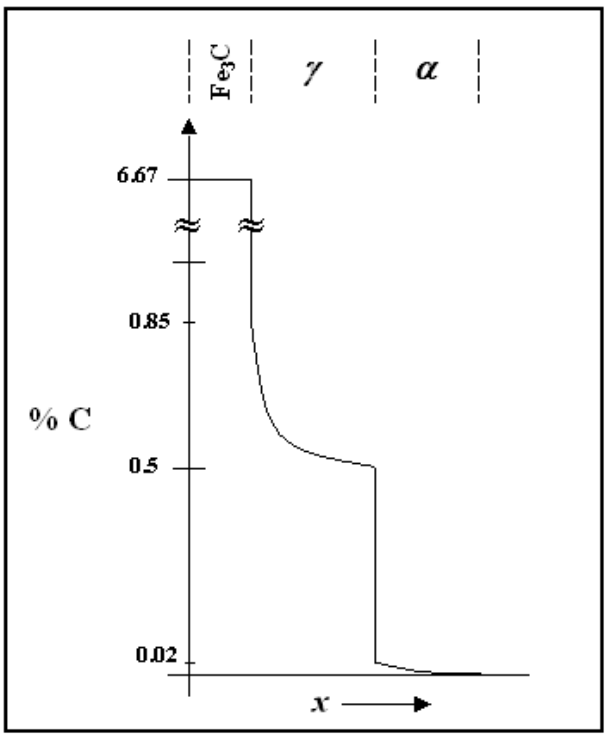

Figure 2.6: A schematic map showing the progression of the depth of the carburised layer with respect to %C by mass.

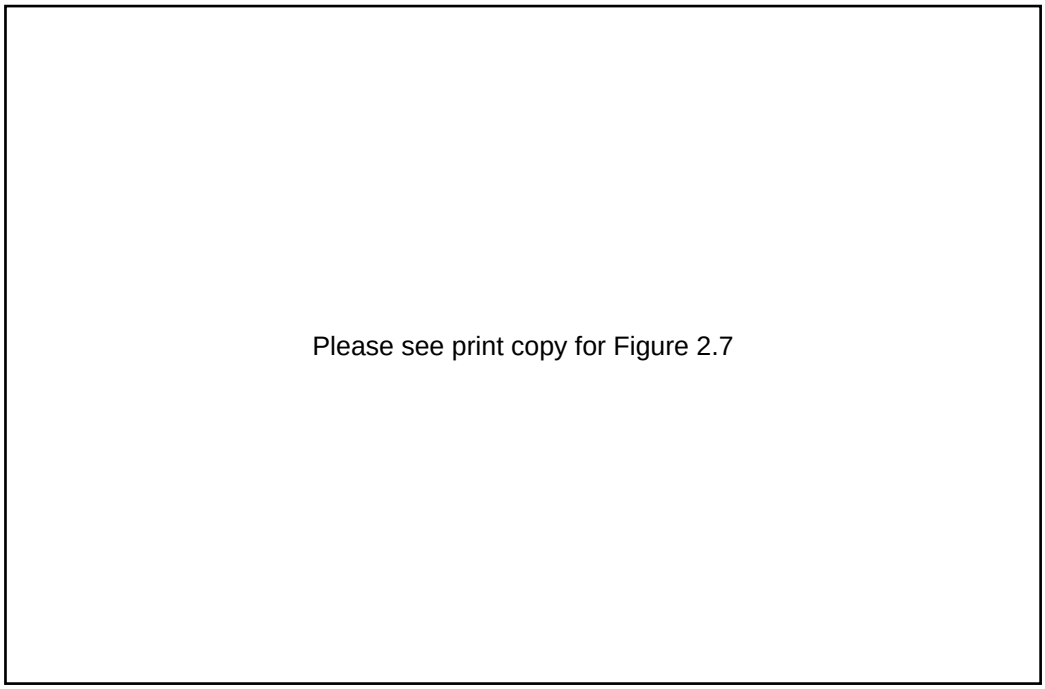

Figure 2.7: The Fe-O phase diagram, showing the partial pressure relationship to temperature[29].

2.5.3. Carburisation and Boudouard reaction Effects During Reduction

The Boudouard reaction as was mentioned, determines whether or not reduction will proceed. For a given temperature, the formation of free carbon is governed by the partial pressures of CO_2/CO. [29] Consider the Fe-O phase diagram in **figure 2.7**, showing the relationship of temperature to CO_2/CO partial pressure.[29, 37]

The three broken diagonal lines on the diagram indicate the Boudouard lines for different pressures (P=0.1 Bar, 1.0 Bar and 10 Bar). The field to the left of each respective lines shows that the Boudouard reaction is to the left and vice versa to the right.

To the left of the lines, the Boudouard reaction is proceeding to the left, (i.e. the CO_2/CO partial pressure is on the increase) in this field reduction does not occur. The reverse is true for the right of the lines.[29, 37] In simpler language, if there is too much CO_2, the reaction is starved of CO and cannot reduce.

The above is given as an overview of the thermodynamics and chemistry essential for the basic understanding of the DRI process.

The thermodynamics and chemistry is not enough however to explain other phenomena emerging during reduction such as whisker formation and topochemical reduction for example. This is where the kinetics of reduction becomes relevant.

2.6. Kinetics

The kinetics of iron ore reduction is an area where the reduction process takes on direct relevance to the sticking phenomena. The kinetics of reduction controls significant outcomes of the process such as, how quickly reduction proceeds in the particle [38], how reduction proceeds (i.e. topochemically say) [37] and the emergence of surface phenomena (such as whiskers). [7] It is important then, that the main points of the kinetics of DRI be explained.

2.6.1. General Kinetics of Reduction

Iron ores are reduced from Hematite to metallic iron via a step-wise process, as in equation 3.1. The reactants CO and H_2 react with the Fe oxides on the surface of a particle and the reaction products are transported from the reaction site [37, 39].

There is a general consensus that the reduction of wustite to iron proceeds via a mechanism proposed by Wagner[7, 40-42].

At the surface of the wustite particle, hydrogen or carbon dioxide reacts according to

$$\begin{matrix}(CO)\\(H_2)\end{matrix} + O^{2-} + 2Fe^{3+} + \square \rightarrow \begin{matrix}(CO_2)\\(H_2O)\end{matrix} + 2Fe^{2+} \qquad (2.4a)$$

after equation 2.4. Oxygen is transferred from the lattice to the gas and there is a production of two ferrous ions and the vacancy created (indicated by a square) migrates to the surface. When the Fe/O ratio is high enough and the iron cation activity is at a critical point the iron metal can start to nucleate on the surface.

The rate at which the reactants arrive at the site, react, get away and allow more reactants through is the essential kinetics of the issue. How quickly and efficiently this can be done is dependent on the ores reducibility, that is the rate at which the ore can be reduced. The reducibility of an ore is dependent on disparate factors such as density, gangue content and porosity. [39]. Measurements of the reducibility of different ores were carried out back in 1936[43], and later[44], and it turns out, that porosity is the dominant factor in deciding the ores reducibility. That is to say that the permeability of the gas into the particle is paramount.

Assume equi a priori access of the gas to every part of the surface, from all possible directions. The surface is reacted to metallic iron first, then, the gas is required to permeate below this layer to react further and then the products must permeate back out. This process is repeated further and further into the bulk. Following this process, a time differential is setup between reaction, permeation and exit gases and the result is that the ore particle is reduced "topochemically".[39] The result is a particle made up of different oxide layers, with iron on the surface, under that wustite (which oxidizes to magnetite on cooling) then magnetite and then hematite at the core as in **figure 2.8**.[30]

As reduction takes place, there is another phenomena that assists in gas permeability. If CO is involved as a reducing gas, it will react with the surface to form $C + CO_2$. The carbon, during carburisation (discussed earlier), will diffuse through the iron to the iron-wustite interface. Here it will react with wustite to form $CO + CO_2$. This being the case, a high pressure is built up under the layers by the CO and CO_2 to about 600 psi. This is enough to burst the iron layer and allow more gas to permeate. [37]

2.7. Rate Controlling Phenomena and Iron Whiskers

There is an important result that arises from the kinetic melee of the reacting gases and solid-state diffusional processes during reduction uncovered by Nicolle and Rist in 1979[7, 39].

As reduction proceeds, the removal of oxygen atoms from the solid at a gas-solid interface results in a chemical concentration within the solid gradients. The iron and oxygen concentrations at the surface change in relation to the bulk values. The diffusion of iron ions and electrons will increase in rate as vacancies facilitate cation diffusion. When wustite reduction begins, the gas-solid interface recedes as oxygen atoms are removed by the gas and iron ions and electrons diffuse into the bulk. This reduction process will lead to the nucleation of metallic iron. There are two possible outcomes of the reduction and nucleation process depending on whether chemical reactions are rate controlling or whether diffusional processes are rate controlling.

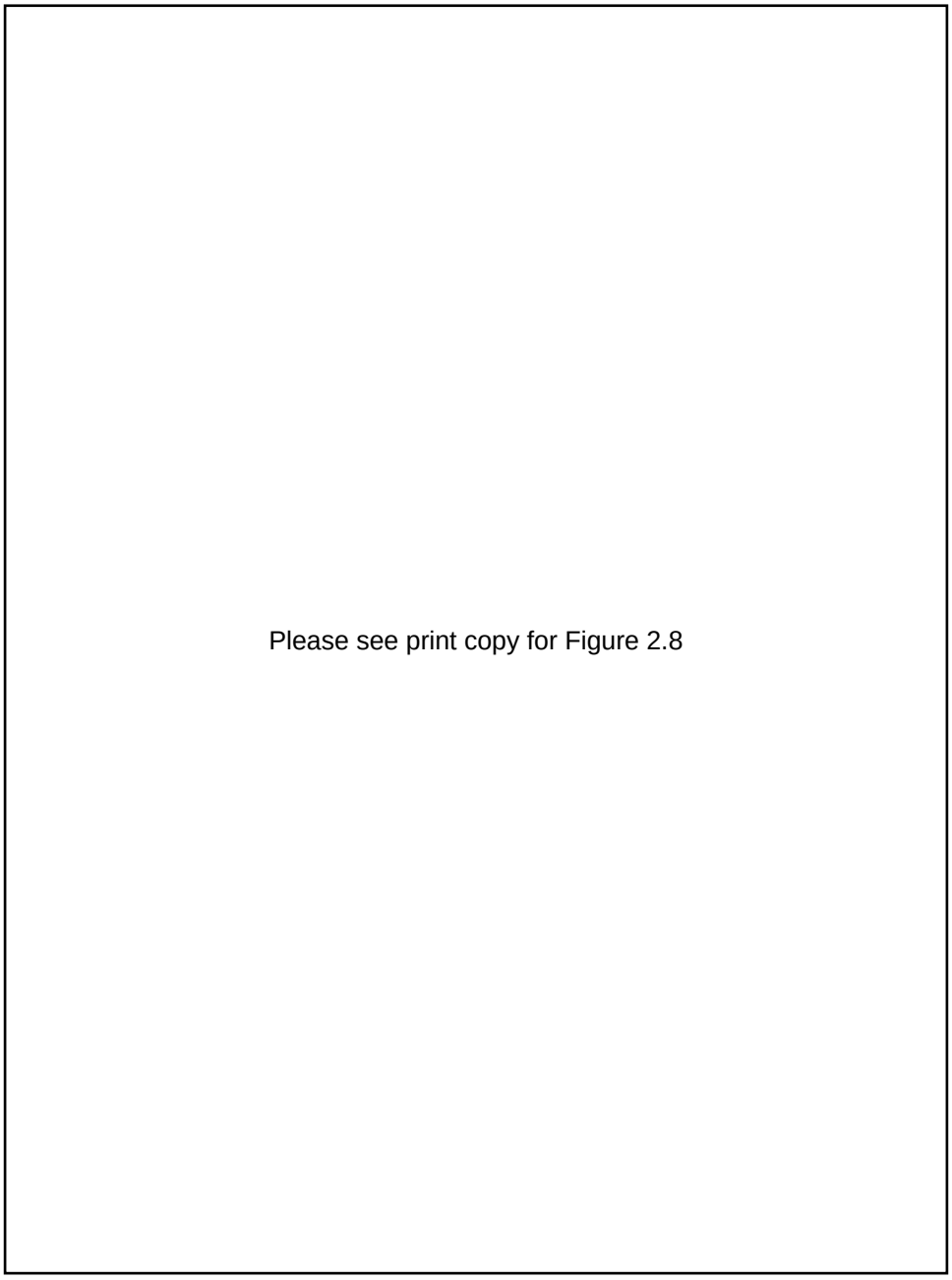

Figure 2.8: A topochemically reduced ore particle, showing the consecutive layers of reduction.

2.7.1. Diffusion as Rate Controlling

If during reduction there is a high rate of oxygen removal on the surface, the rate of iron nucleation is higher than the rate at which iron cations can diffuse through the wustite. Thus diffusion becomes the rate-controlling step in the reduction reaction. If the ratio Fe/O exceeds the equilibrium value between iron and wustite (i.e., the iron activity is higher than that of the oxygen), the reaction zone will become super-saturated with iron. The result is that iron will nucleate all over the surface and form "platelettes" of iron which merge together to establish a "sponge" iron layer[7]. This enables a topochemical pattern of reduction to be established (as in **figure 2.8**). [30]

2.7.2. Chemical Reaction and Diffusion as Rate Controlling

If the gas reaction has a low reducing potential and the wustite has a high iron diffusivity (i.e. due to cation vacancies, defects and surface cracks), a different situation arises. If iron nucleation at the surface is minimal, the whole wustite grain can be affected by the gas. The Fe/O ratio can become more or less uniform over the whole grain. The whole particle becomes supersaturated and nucleation can occur discretely, but homogeneously throughout the particle. As soon as the iron can nucleate at the surface, excess iron ions will diffuse to the nucleation site and feed the growth. [7] This process will give rise to iron whiskers as shown schematically in **figure 2.9**.

The whisker will grow until the diffusion process equilibrates (that is, when the activity curve attenuates) and the reaction is terminated. The surface morphology results in iron whiskers sprouting all over the surface (see **figure 2.10**).

Thus, during the reduction process there are two main outcomes. If diffusion is rate controlling, a topochemical pattern of reduction results. If chemical reduction is rate controlling, then whiskers will result.

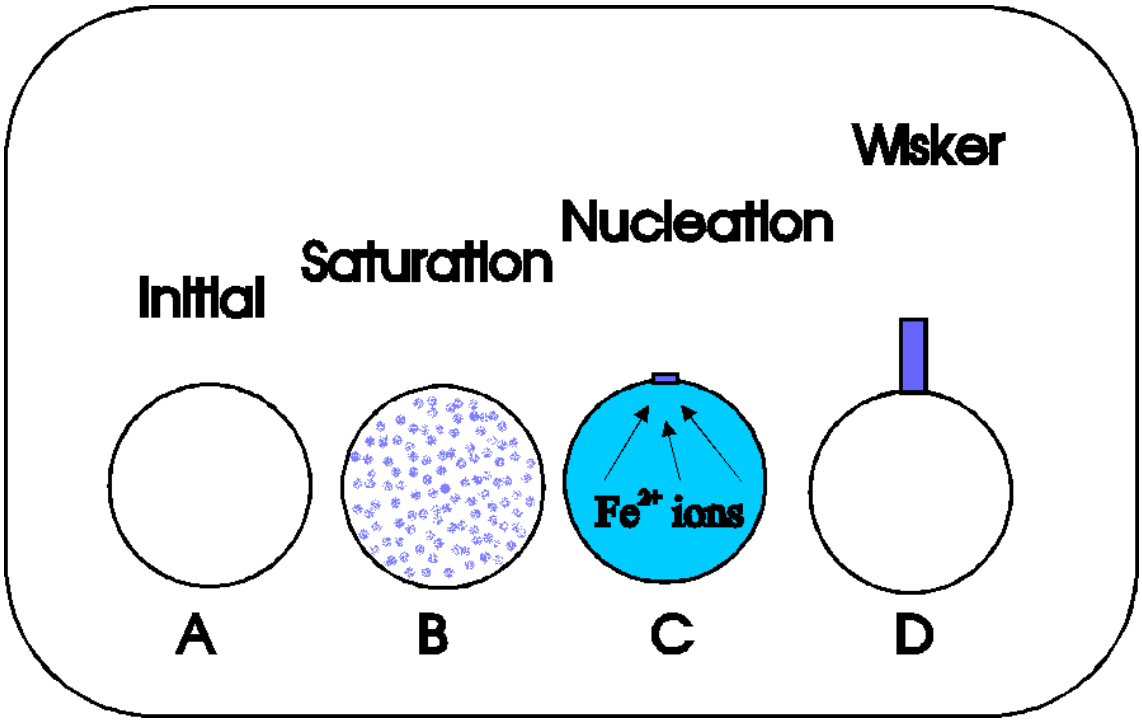

Figure 2.9: A schematic diagram of the result if reduction is rate controlling**.**

Please see print copy for Figure 2.10

Figure 2.10: Electron micrograph of multiple iron whiskers on the reduced surface[4].

[4] Courtesy of BHP.

2.8. Defluidisation, Sticking, Sintering and Whiskers

2.8.1. Defluidisation

The phenomena of defluidisation in DRI fluidised beds is the central issue addressed in this work. Defluidisation is a term referring to the event in which a fluidised bed reactor loses fluidisation velocity, halts its motion and is reduced to a semi packed state.[5]

This problem is most likely encountered when "clean" iron ore surfaces, with a high degree of metallisation make contact and adhere to one another. [6, 11]

In the literature, the concept of defluidisation and sticking seem to be used almost interchangeably [5, 6, 12, 13, 17, 45]. It is not difficult to see why the two events are strongly correlated. [6-8, 17, 45]

It is possible however, that correlation can be confused with causation. Sintering and sticking are observed when defluidisation occurs. However, it has not yet been shown definitively whether or not sticking is the cause of defluidisation, or one of the factors leading to it, or simply the result of particles being stationary after defluidisation has occurred. This is an important distinction, as the question can be asked, “Does sticking occur and a reactor will then defluidise?” or “Does a reactor defluidise and then particles stick?”

This distinction aside for the moment, it is at least a common factor in defluidisation and therefore should be discussed further.

2.8.2. Defluidisation and Sticking

It has been observed that the phenomenon of defluidisation and sticking is mainly associated with whisker growth, nodular precipitates of iron and roughness on the surfaces of reduced iron ore particles. [6, 7, 12, 17]

It has been surmised that whiskers may interlock in like a "Velcro", producing excess friction, entanglement, and increase overall contact time of the particles and heighten the propensity to stick and sinter. [5, 32]

Gransden and Sheasby have shown a temperature relationship to defluidisation. [6] They found that it is possible for a reactor to defluidise at temperatures above 600°C whenever acid cleaned surfaces make contact. They also observed that if particles were dirty (they surmise it effectively harbouring a barrier film on the surface), the reactor bed would not defluidise until a temperature of 740°C is reached. Further observations led them to postulate that iron nodules were capable of breaking the barrier film and clean surfaces can then impinge. These observations provided evidence that defluidisation is strongly related to sintering.

The mechanism of defluidisation by sintering of whiskers will be discussed later, for now, a dossier of the factors effecting sticking found via the last forty years of research will be given.

2.8.3. Factors affecting sticking

Sticking occurs for T > 600°C for clean surfaces and T > 740°C for dirty surfaces. If sticking is first observed at T > 600°C, and the bed defluidises, it is possible to cool the bed separate the particles and refluidise. If this is done the defluidisation temperature is reduced to 595°C. Annealing of the ores before reduction can reduce the chances of defluidisation. [7, 32]

Gas ratios of (CO_2/CO) = 0.19 is correlated with whisker growth which is associated with defluidisation. [7] The addition of a large partial pressure of nitrogen to the CO_2/CO mix tends to increase whisker formation. [46]

A smaller grain size over all tends to increase sticking tendency. [8, 9] It is thought that the smaller particle size will provide an overall larger surface contact area in the reactor bed, and it favours whisker growth.

The ore type selected for the process has an influence in the outcome of sticking. Magnetitic ores have a larger propensity to form whiskers than the Hematitic ores. [14] Hematitic ore are found to strongly promote whisker growth. [15, 47] Goethitic ores tend to reduce forming smooth iron layers and hence do not lend themselves as much to sticking. [32]

The term “gangue” refers to the rock and waste material found in iron ores. Ores with higher percentages of gangue has less of a tendency to stick[48]. On the other hand whiskers will increase with an increase in alumina (Al_2O_3)inclusion content[45].

Additions of CaO will promote whisker growth[49]. Sulphur content will also promote sticking for 700°C < T < 1000°C[12].

In terms of barrier films, silica has been found to be effective against sticking[6]. MgO additions have been thought to have a negligible effect in suppressing sticking, [39] however recent findings at BHP suggest that MgO is an effective anti-sticking agent. [5]

Whisker growth and agglomeration are a strongly correlated sub-set of defluidisation. The study of whiskers and their effects on sticking has been pursued by many authors[6, 7, 11, 17, 45, 50, 51].

In view of this, to what ever degree agglomeration, assisted by whisker growth can be considered responsible for defluidisation, it certainly is a major possibility in deducing a mechanism. It is important then, that a dossier be given as to the conditions that either encourage or discourage whisker growth.

2.8.4. Factors Which Promote Whisker Growth

Nicolle and Rist, back in 1979, provided a comprehensive list of factors which will either encourage whisker growth, or suppress it[7]. Their list was derived from their own work and the work of many other authors. The list of conditions has not really changed by much since then, and so a synopsis of the major factors involved identified by them will be presented.

According to the work of Nicolle and Rist, a strong relationship between pre-existing surface morphology and whisker growth was found. It was shown, that a jagged, defected, cracked or rough surface morphology encouraged the growth of whiskers. They quantified this relationship with their 'Z_N' map topography. Their results are shown in **figure 2.11**.

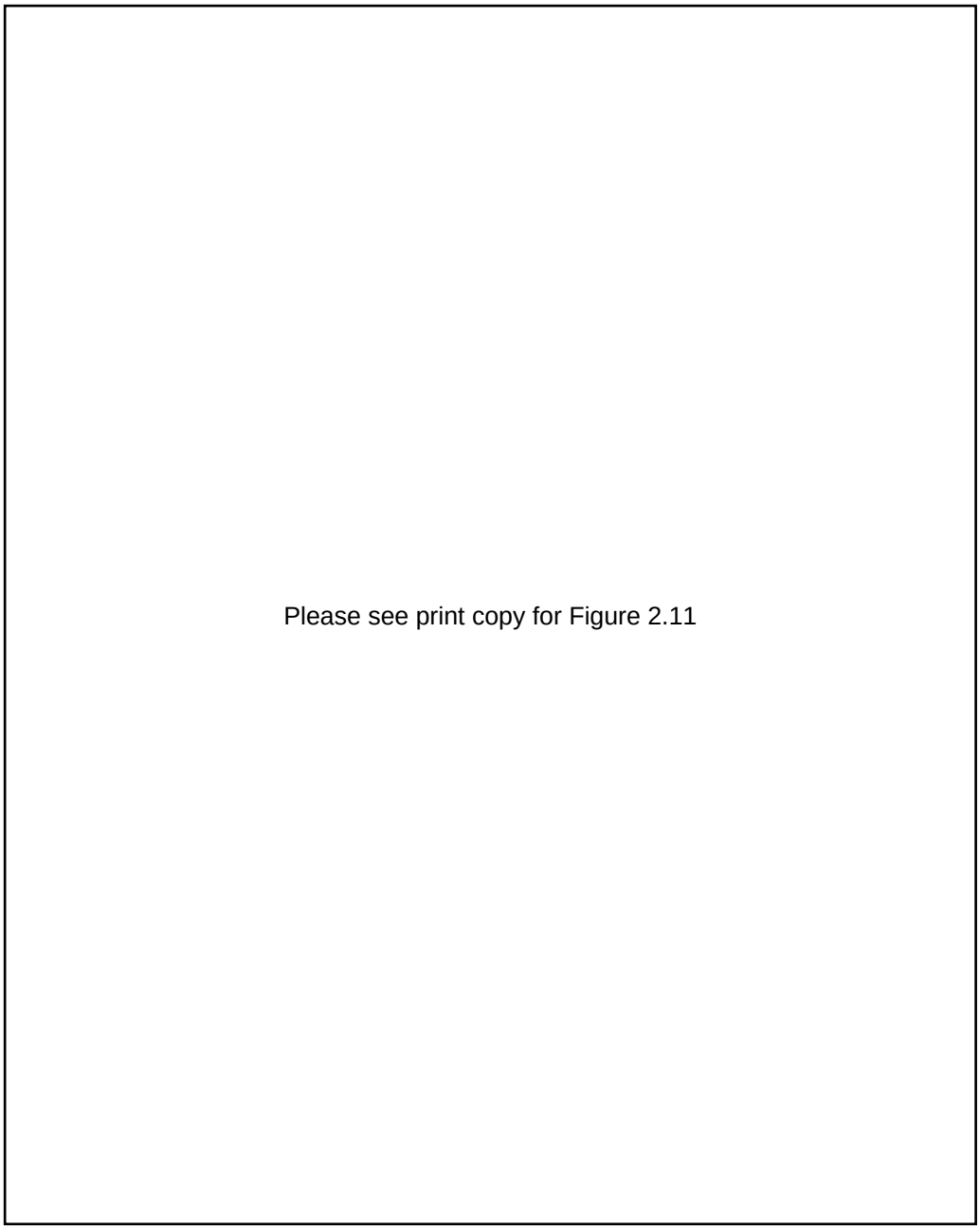

Figure 2.11: Relationship between the pre-existing topography of ore particles, and whisker growth (after Nicolle and Rist).

Here the relationship between pre-existing morphology and resulting surface morphology can be seen. Included in this picture are the results of conical outgrowths, which occur when the diffusion rate and the reduction rate are comparable. The diagram in **figure 2.11** shows in schematic representation the three major surface conditions leading to different types of whisker growth. The surface may have, (a) isolated large asperities on the surface, (b) multiple small asperities and (c) a relatively smooth surface, free of asperities.

Down the left of the diagrams the particular rate controlling reduction mechanism is indicated. If the reduction is chemically controlled (that is, having a high rate of Fe^{2+} ions to the surface and into the asperities) it can be seen that the result is, (a) large isolated whiskers, (b) small multiple whiskers and (b) a sponge iron layer respectively.

Under mixed control partially formed conical whiskers take the place of the long cylindrical whiskers again with an iron layer in the case of a smooth surface. In the final case if diffusion is rate controlling a sponge and smooth iron layers predominate. In all cases, if whisker growth is to be discouraged, the surface needs to be as smooth as possible and the reduction should preferably be diffusion controlled.

There is also a size relationship to whisker growth. The smaller the grain size is (particularly in the case of powders), the higher the propensity will be for whisker growth. It is believed that the smaller size will favour chemical control.

Temperature also has a major affect. The swelling index of the particle is related to the degree of whisker growth on a wustite particle. It has been shown for T = 750°C and T

= 950°C the swelling index of whisker growth will be at a maximum. It is also found that for a gas partial pressure of (CO_2/(CO + CO_2)) = 0.16 measured at T = 940°C, whisker growth is maximised. [52]

If CaO is distributed heterogeneously across the surface, whiskers tend to increase. Sulphur in the reducing gas will reduce the chemical rate constant of the reducing gas and chemical control is favoured.

Finally, cation additions, particularly Ca^{2+}, Na^{+} and K^{+} are observed to promote whiskers. The explanation proffered, is that cations will expand the lattice and facilitate vacancy diffusion, increasing the diffusion rate, and increase whisker tendency. No evidence has yet been found for this view.

If the pre-existing surface morphology is smoother, then it is harder for whiskers to evolve. This also has the dual effect of removing defects that are also suspected to promote whiskers.

The minimum swelling index of wustite particles is achieved around T = 850°C. For T < 850°C and T > 950°C the slope is negative and it indicates a tendency towards a smooth Z_N map. In general, when T > 1000°C a topochemical layer is favoured.

2.9. Defluidisation Mechanisms

There are at least one half dozen or more mechanisms that have been proposed in the past in an attempt to explain the mechanism of sticking. These mechanisms may all be

present in the process or they may exist in varying combinations. It is also possible that one single mechanism may be either responsible or at least the dominant mechanism. Which ever of the mechanisms are truly at work here still awaits experimental verification.

2.9.1. Theories of Mechanisms

A general list of possible contributing mechanisms of defluidisation has been compiled by Damien O' Dea in 1998 [5].

In that list are such mechanisms as; 1) Chemical bonding reactions and/or sintering of particles. 2) The formation of cohesive liquid films such as water which binds particles together. However studies at BHP suggest water vapour additions has anti-sticking properties[53]. 3) Surface roughness may increase interparticle friction, resulting in a loss of kinetic energy of the particles and increasing contact time. 4) Surface whiskers acting as Velcro like structures and interlocking together. 5) Surface plasticity of particles at high temperature leading to deformation and molding of the surfaces together. 6) Electrostatic charging of dielectric material due to triboelectrification causing the particles to stick to internal walls and standpipes. [54]

One such mechanism could be the magnetisation of particles. It is found in topochemically reduced particles, that a core of unreacted hematite is left behind. [30] It is well known in geological and physics circles that hematites are capable of forming Thermo-Magnetic-Remnants (TRM). [55-57]

Lewis Neel showed that when hematite is heated to above 600°C, it becomes paramagnetic, and the magnetic dipoles will align to the earth's magnetic field and the magnetic field induced will remain even when cooled. It is just possible that magnetised hematites, especially if they are single domain, will produce a force strong enough to cause particle attraction and attraction to the interior walls.

A less acknowledged mechanism of adhesion is that of intermolecular or van der Waal's forces. These forces can produce high pressures particularly when particles or points of contact are at micron or submicron scales[58]. The van der Waal's stress for metals when in contact can typically be between 100-200 MPa[58-60]. In nature, the tokay gecko uses van der Waal's forces on its feet to climb up walls and hang from ceilings[61].

Attempts have been made to model the general defluidisation of a reactor bed, incorporating stochastic equations of motion, which account for the various forces as perturbations in the formula. These models are of interest in constructing a predictive theory of defluidisation, however they offer little in the way of fundamental understanding. [62, 63]

The earliest evidence emerging suggesting that sintering may be an important mechanism involved in defluidisation, was given by Gransden and Sheasby in 1974. They uncovered that there is a strong correlation between sticking and the sintering of iron ore particles [6].

It was not until much later however that a working quantitative model was developed to describe iron bridging and neck growth in terms of defluidisation. Basing their work on Kuczynski theory of solid-state sintering [64], Mikami and co-workers modelled neck growth via surface diffusion when two particles are in contact. [13]

The relationship between neck diameter and time was essentially logarithmic and was worked out for various temperatures. They state in their work that fluidised bed conditions will provide enough contact time to form sintered necks and become cohesive enough to initiate defluidisation.

Their models however require time scales on the order of hundreds hours to form substantial necks and it is difficult to see its application in the case of fast collisions. In addition, the sintering mechanism relies on surfaces in contact, to initiate diffusion, at least in principle. Observations under real time SEM show that contact between particles is not always necessary, and in some cases particles can "sinter", across gaps. **Figure 2.12** shows an example of sintering at a distance.

The image in **figure 2.12** shows one the greatest mysteries in this field to date. During the reduction process, it is possible for whiskers growing from two physically separated particles to preferentially grow toward one another. The gaps of separation have been known to be as much as 20 microns.

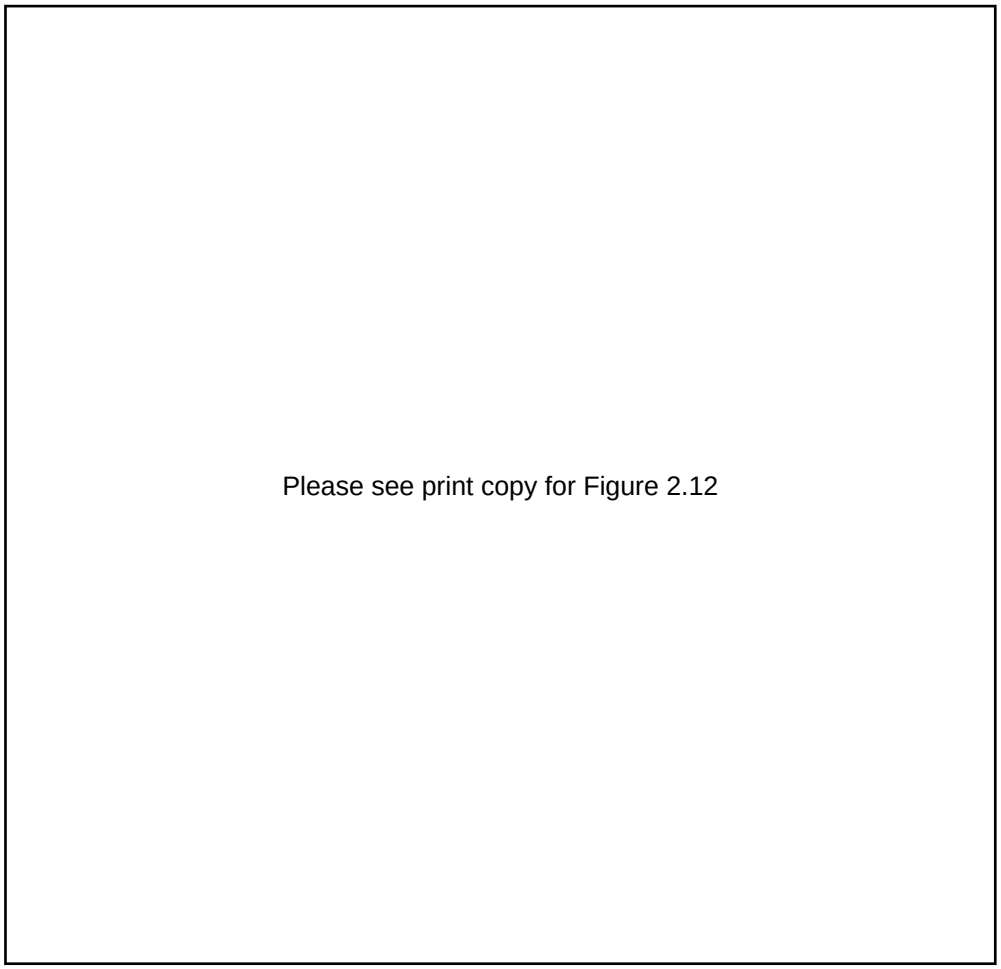

Figure 2.12: Sintering at a distance.[5]

[5] Courtesy of BHP.

The essential driving force for sintering has been established as being the need to reduce surface area, and in the case of small particles, the initial mechanism is predominantly via van der Waal's forces and surface diffusion. The surface diffusion aspect of sintering depends on the difference in curvature of the connecting particles. Other diffusion mechanisms come into play in order to densify interparticle necks. The theory built up to date is modeled after two ideal spheres in contact. [65, 66]

When a powder aggregate is sintered, the compact may increase in density, due to neck formation. There are six different pathways for matter transport during sintering, contributing at different stages. The six identifiable pathways are indicated in **table 2.1**.

Table 2.1: The six distinguishable pathway to sintering.

Mechanism No.	*Transport path*	*Source*	*Sink*
1	Surface diffusion	Surface	Neck
2	Lattice diffusion	Surface	Neck
3	Vapour transport	Surface	Neck
4	Boundary diffusion	Grain boundary	Neck
5	Lattice diffusion	Grain boundary	Neck
6	Lattice diffusion	Dislocations	Neck

These sintering mechanisms are modeled after two ideal spheres particles in contact, and assume no compressional forces acting on the particles, and no phase changes occur during sintering. The situation is illustrated in **figure 2.13**. The diagram shows two connecting spheres and the arrangement of matter transport pathways, where sources and sinks are indicated.

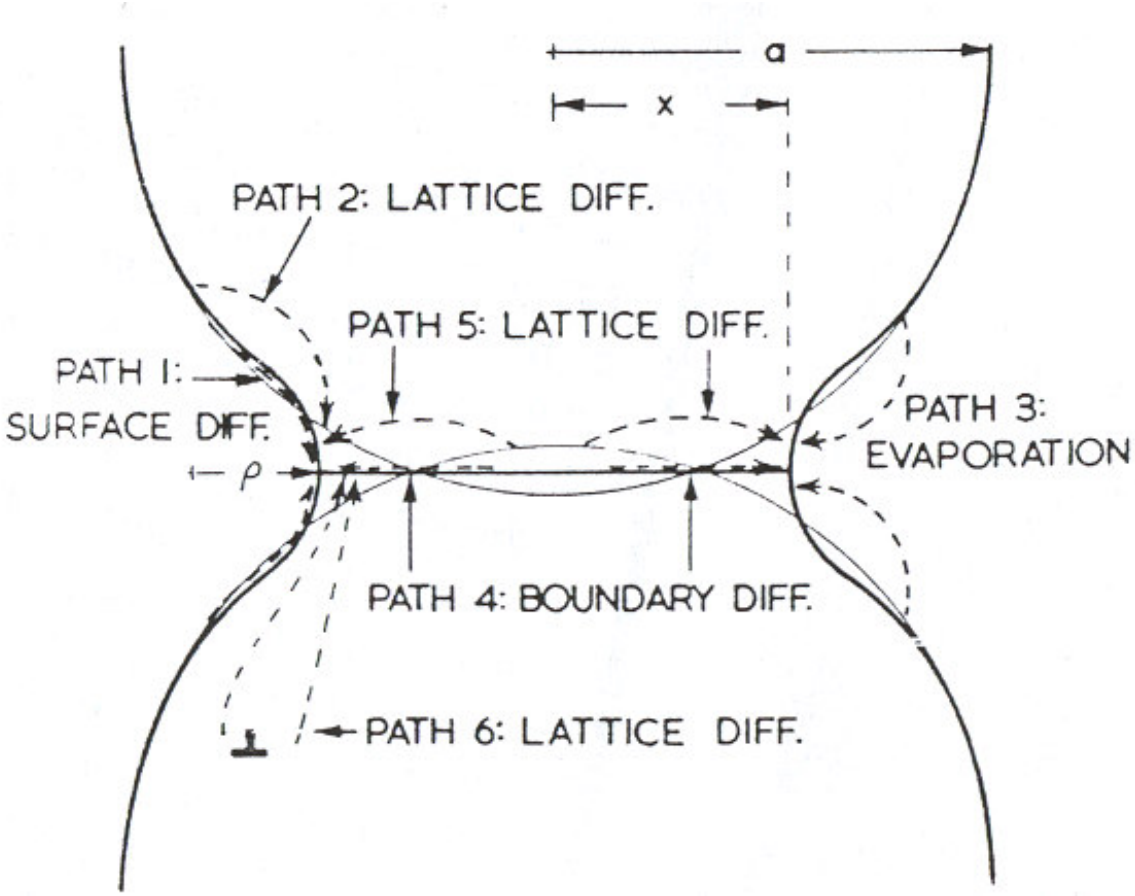

Figure 2.13: The simple arrangement of the sintering of two ideal spheres, and the matter transport pathways.

The ideal model of sintering has been developed and provides a relationship between neck radius, contact area and time. Comparing then, the ideal case to the case of a rough surface displaying iron whiskers, the situation may be considerably altered. Take for instance, the model of sintering developed by Kuczynski in 1949 [64]. In the case of surface diffusion of two ideal spheres in contact, the neck radius with respect to time is given by;

$$a = \sqrt[7]{\frac{56\gamma_s z_0^4 R^3 D_s t}{k_B T}} \tag{2.9}$$

where γ_s is the surface tension, z_0 is the lattice parameter, R is the radius of a spherical particle, D_s is the rate of surface diffusion, t is the time, k_B is Boltzmann's constant and T is the temperature. If whiskers are present, the surface becomes effectively an array of spheres in contact, instead of one sphere in contact. This is illustrated in **figure 2.14**.

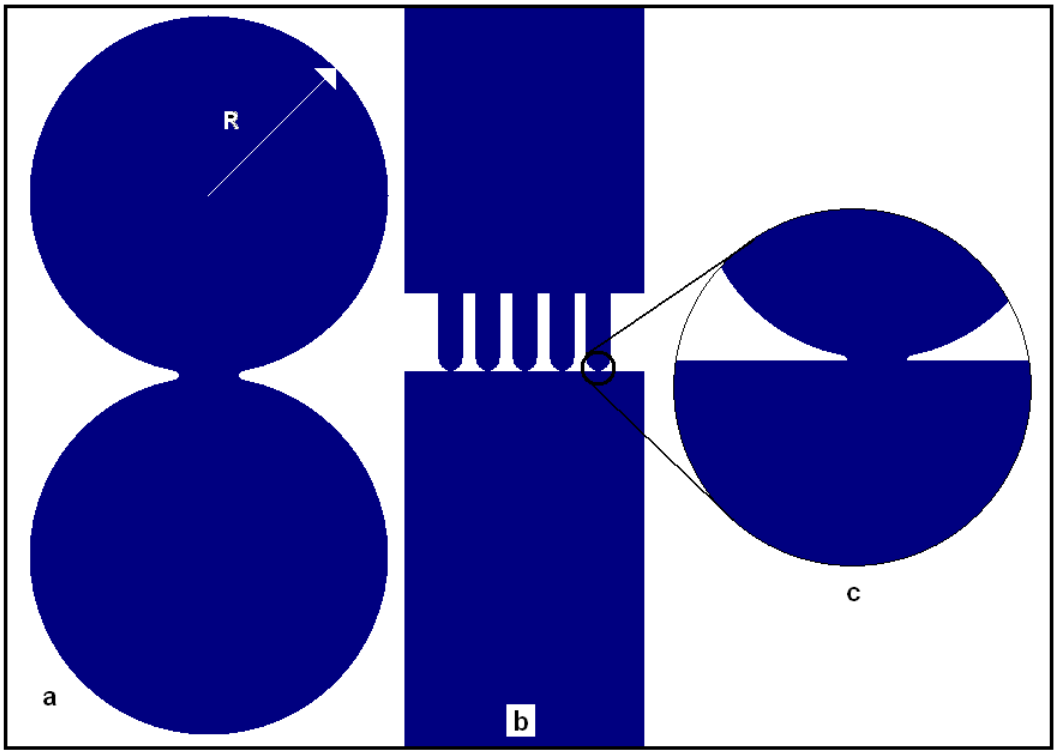

Figure 2.14: An array of spherical surface contacts resulting from whiskers. The small tips have a large contact area relative to their size.

The relationship in equation 2.9 implies that the smaller tip radius will bind to the surface more efficiently due to the larger contact radius relative to the radius of the spherical tip. This is so as $\frac{a}{R} \propto \frac{1}{R^{4/7}}$.

Work by Matsumura (1971), shows that for iron wires of radius 200μm held at 1050°C, it took 390 hrs to form necks of appreciable width [67]. Translating this back to the sintering of particles of around 100-200μm at T = 735°C, since this temperature is considerably lower than 1050°C it is difficult to see how this kind of mechanism can propagate a cascade of sticking quickly enough. Laboratory studies suggest that defluidisation can occur within an hour if no anti-sticking additives are present[5]. Computer modelling and some experimental data places the time for sintering at approximately one hour for an appreciable neck to form, that is to say a neck radius of 0.2-0.3 of the particle radius[13, 63]. Sintering, as mentioned, relies on contact of surfaces, however observations of real time SEM images made at BHP in Newcastle show surfaces merging and "sintering" at a distance.

It has been suggested that if the correct conditions are present for whiskers to form on an ore particles surface and the surfaces impinge, that the whiskers will grow toward one another and become entangled, forcing the particles to bind together.

The behaviour of preferential growth and entanglement has been observed, [17, 18] however no mechanism for this growth has been found. If the whiskers do grow and entangle, then there is of course sufficient time within the process to initiate sticking, provided that the whiskers are still long enough, and close enough, to entangle.

It is just possible that whisker growth and sintering are not mutually exclusive, and that they will work in conjunction to defluidise the reactor bed. Whiskers have a micron to submicron sized tip radii that makes them ideal for rapid sintering

2.10. Initial stages of sintering, a focus for study

Identified by Ashby,[68] and Swinkels[69] are the sequential stages of the sintering phenomena. They point out that the so-called stage 0 of sintering where two particles are in a vacuum and not affected by electrostatic, magnetic or other transient forces, involves adhesion by van der Waal's forces. Stage 1 sintering involves the other diffusion mechanisms of sintering as time progresses. At this stage, inter-particles necks are formed with a low density. Stages 2 and 3 sintering occur after the order of hundreds of hours in the case of iron, and it is these stages that densify the necks.

In the case of iron or other metallic system, Swinkles and co-workers indicate that stage 0 sintering will form a neck radius of 1% of the particle radius, given the understanding of van der Waal's forces and contact mechanics at that time. In gamma-iron, sintering via surface diffusion can take place for at least the first 100 hours before other mechanisms begin to operate.

Laboratory scale studies of defluidisation, conducted at BHP indicate that defluidisation, in the absence of any anti-sticking additives, will occur approximately ninety minutes into the reduction process[5]. This would suggest that stage 0 sintering, and surface diffusion rates are crucial to the defluidisation phenomena.

2.10.1. The sticking problem at Port Hedland

The typical operating temperatures in Reactors 2 and 1 are 735°C and 785°C respectively, therefore closely resembling temperature T in **figure 2.4**. In the FINMET process there is a high content of Methane (CH_4) of approximately 20 – 25%. Under the operating temperature indicated above for Reactor 2 the following reaction can occur:

$$CH_4 \leftrightarrow C + 2H_2 \quad (2.10a)$$

$$C + H_2O \leftrightarrow CO + H_2 \quad (2.10b)$$

$$C + 3Fe \leftrightarrow Fe_3C \quad (2.10c)$$

$$2CO + 3Fe \leftrightarrow Fe_3C + CO_2 \quad (2.10d)$$

$$CO + H_2O \leftrightarrow CO_2 + H_2 \quad (2.10e)$$

This effects the surface of the iron by the decomposition of soot and hence the formation of cementite layers. Considering this and by an analysis of the reactor products, the reduction gas is clearly carburising. Products from reactor 2 contain approximately 0.5%C and that of reactor 1, 1.5%C. The major problems with sticking seem to be encountered in the transfer of solids from Reactor 2 to Reactor 1, therefore with the product of Reactor 2. The constricted space of the pipe will only add to the problem.

The 'sticking test' developed at the Newcastle Laboratories of BHP discriminates well between material which have a tendency to stick from those that do not. An example of the output of such a test is shown in **figure 2.15** (Courtesy of A Shook). Whereas the product of Reactor 1 does not show a tendency towards sticking, the product of Reactor

2 displays a very different sticking behaviour below and above a temperature of approximately 720°C.

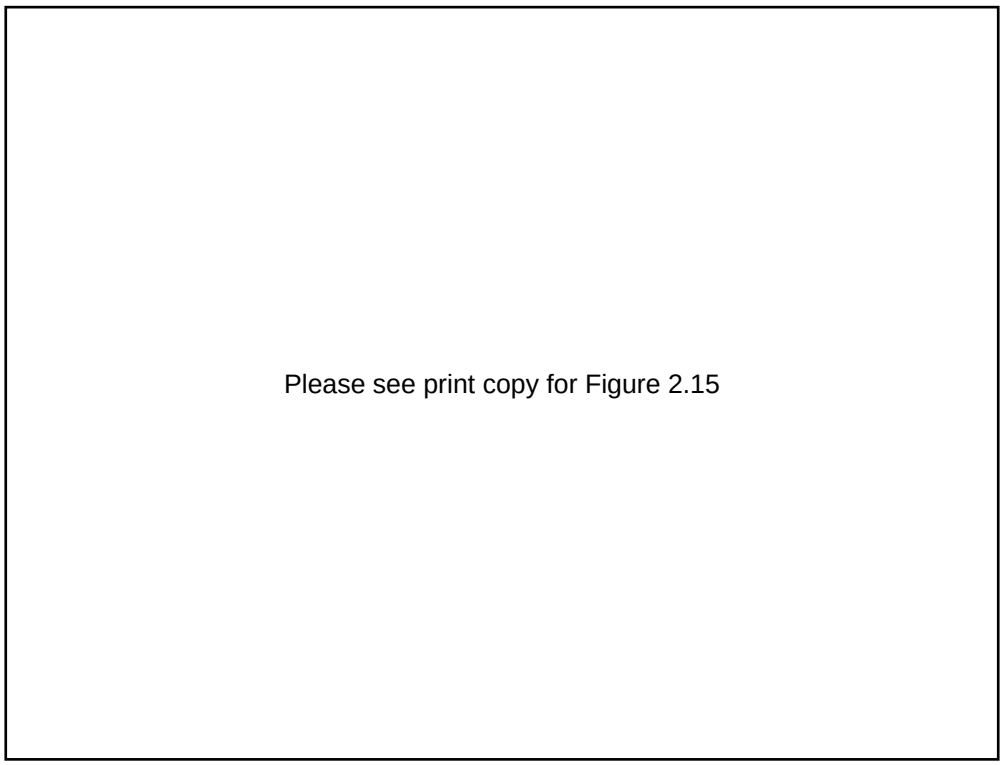

Figure 2.15: The correlation between the angle at which iron powders will spill from a spoon in relation to temperature. Reactor 2 products being iron containing about 0.5%C, shows a sharp change in sticking behaviour at the eutectoid temperature. The reactor 1 product of approximately Fe-1.5C does not display this abrupt change in sticking tendency in the vacancy of the eutectoid temperature.

In fact it is not strictly correct that "sticking" or adhesion of iron powders will not be observed at temperatures between 24-723°C. Take for instance a typical iron powder where the mean particle size is approximately 50μm. When a spoon full of the powder is gently tipped at room temperature the powder will tip out yet it will do so in clumps that appear to separate at rough fault lines as in **figure 2.16**. When the powder is all out there remains a coating of iron powders and some random clumps left behind. The

forces at work here are possibly electrostatic and capillary but most likely van der Waal's forces.

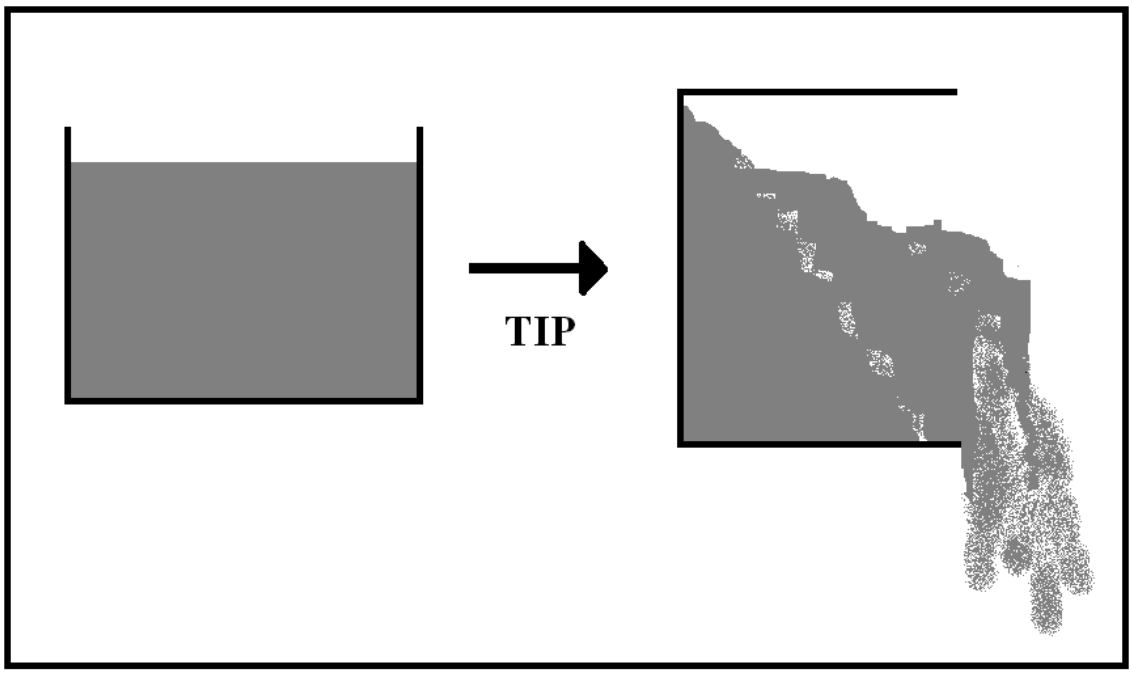

Figure 2.16: As the iron powder is tipped from the spoon the powder will fall in characteristic clump-plates disengaging along apparent fault lines.

If particle contact is ideal, van der Waal's forces should be enough in principle to overcome gravity and in the case of isolated particles this is certainly the case in practice. At room temperature the contacts are less than ideal and the bulk mass of the powder is able to overcome contacts and the powder can cascade out of the spoon.

It is believed there is great significance in the sticking trends described and the following is proposed:

The transition temperature shown in **figure 2.15** for reactor 2 products is actually 723°C. The product of Reactor 2 contains approximately 0.5%C and this Fe-C alloy consisting primarily of primary ferrite and pearlite below a temperature of 723 °C

figure 2.17d. At 723 °C the pearlite transforms to austenite and at temperatures between 723°C and 850°C the structure consists of ferrite and austenite as in **figure 2.17b**. The product of Reactor 1 contains approximately 1.5%C. At temperatures below 723°C the structure consists of primary cementite (Fe_3C) and Pearlite **figure 2.17e**. At 723°C on heating the pearlite to austenite and at temperatures between 723°C and 850°C, the structure consists of austenite and primarily cementite **figure 2.17c**. At higher temperatures this Fe-C alloy will transform to a fully austenitic structure **figure 2.17a**. It is important to note that a rim of cementite is expected to form on the outer surface of a particle, as it is the outer rim that is in contact with the carburising gas.

Neither product displays complete adhesion below 723°C because the surface composition is such that the inter-particle contact between Reactor 2 product is mostly pearlite/pearlite and that of Reactor 1 mostly cementite/cementite. Both the pearlitic and cementite structures will deform les than either pure ferrite or pure austenite.

The product of Reactor 2 has a greater sticking tendency above 723 °C than below because the inter-particle contact above 723°C is austenite/austenite. The Reactor 1 product displays a lower sticking tendency because the inter-particle contact is mostly cementite/cementite. Cementite has a much higher melting point than austenite and is mechanically much stronger. Particles are therefore less likely to bind together and the sticking tendency is reduced.

It is believed that surface roughness and hardness at lower temperatures will inhibit ideal contact between particles preventing sites for atomic binding from being realised.

Rapid rates of surface diffusion and a soft malleable surface may enable the van der Waal's force to create close to ideal surface contacts.

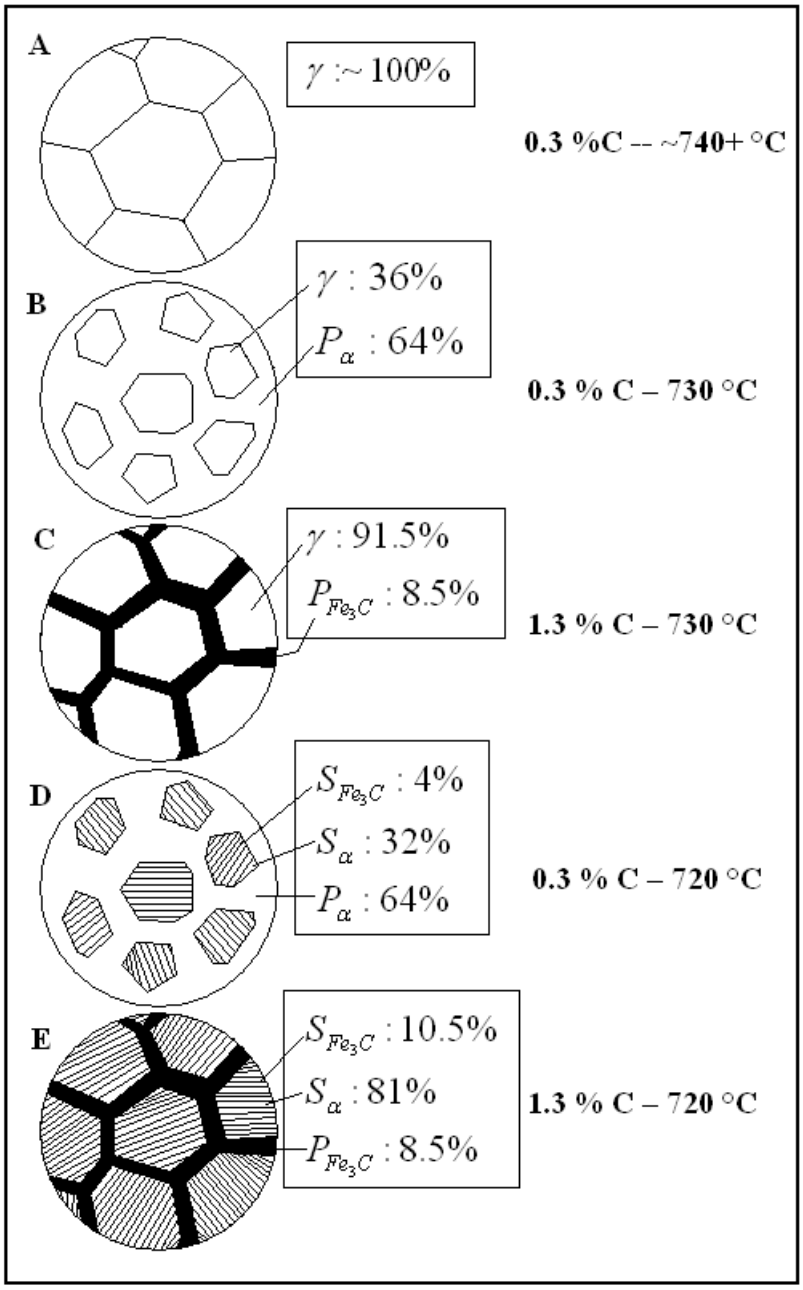

Figure 2.17a-e: Schematic representations of iron surfaces for various iron-carbon alloys for various temperatures.

2.11. Conclusion

The process of DRI, and its associated issues of agglomeration, is not only complex, but it has a long history as well. The study of agglomeration in DRI is a field that has drawn on research from different backgrounds, both theoretical and experimental. It was the aim of this review, to summarize the topic for the reader and provide a sufficient background so as to be able to follow future work in the field.

The beginning of DRI as a way of making iron is found as early as the middle ages. It is in the modern age of steel processing however that DRI it has gained economic and technological significance. The relatively low cost of producing directly reduced iron has been important in smaller economies of scale, establishing itself in developing countries.

In order to understand the issue of defluidisation, it has been important first to understand the thermodynamics and kinetics behind reduction. In understanding the thermodynamics, it helps to gain knowledge in the various process conditions that affect sticking. Distinct temperature conditions indicate when whisker growth and sticking has the highest probability of occurring. It is explained that the swelling of iron ore particles (a symptom of whisker growth) reaches a peak between 750-950°C. In addition, the sticking behaviour is seen to rapidly increase above 723°C. This indicates a strong temperature dependence and provides a suitable temperature range for study. The kinetics of iron ore reduction we have seen, is important in controlling the rate and pattern of reduction.

A discussion of the mechanisms behind defluidisation was given. It is seen in the literature at least one half dozen possible mechanisms might lead to defluidisation. It is not known for sure which of these mechanisms, if any, are at work in sticking. There is consensus however, that sintering is likely to be responsible.

It is surmised here that if the reduction of iron ore is taking place under particular conditions of temperature and surface conditions, (such as freshly nucleated iron and perhaps whisker growth) where sticking has been mostly observed, that it is most appropriate to consider closely, the sintering properties under these conditions.

It has been pointed out in the literature that surface diffusion may be the most predominant factor in sintering of iron in the early stages of sintering. Much data has been gathered about pure iron and rates of surface diffusion, however nothing quantitative about the effects of carbon in iron on surface diffusion has been gathered. Differences have been noted in sticking behaviour between 0.5 percent carbon steel and 1.5 percent carbon steel in the FINMET™ process.

In the past, the effects of basic initial adhesion properties have been dismissed as having very little to do with the sintering process. The adhesion forces are due to van der Waal's forces, and to a less consistent extent, electrostatic and magnetic forces. Up until the beginning of this study, no experimental knowledge existed on the adhesion effects of van der Waal's forces between iron surfaces. There had been no inquiry into the effects of temperature on adhesion up until the beginning of this study, and so authors tended to suggest that the effects of van der Waal's adhesion did not change with temperature.

Specific to the FINMET™ process, a correlation between going above the eutectoid temperature and a sharp rise in sticking is observed in iron products in reactor two. It is important that this finding be tested with a controlled quantitative study of sticking behaviour.

The gaps in the knowledge indicated in the above three paragraphs, have provided a direction for study in this thesis. In this study, an analysis of surface diffusion for various carbon steel alloys has been conducted. A new technique of studying surface diffusion using high temperature confocal microscopy has been developed in the process. New knowledge of van der Waal's forces between iron surfaces has been obtained using atomic force microscopy. Finally, a new technique for measuring sticking at high temperature has been developed.

Chapter 3:

Measurement of van der Waal's forces and surface stresses between iron/iron surfaces in water by Atomic Force Microscopy and contact mechanics theory

Chapter 3: Measurement of van der Waal's forces and surface stresses between iron/iron surfaces in water by Atomic Force Microscopy and the application of contact mechanics theory

3. Introduction

The last decade or so has seen a new application of Atomic Force Microscopy measuring surface and interfacial forces in metals and other materials [70-77]. Disparate authors have shown that the Atomic Force Microscope (AFM) has increased the limits to which surfaces can be studied [78, 79].

In the present study, van der Waal's (vdW) or non-retarded, dispersion forces and the work of adhesion resulting from van der Waal's forces has been measured in metallic iron. Atomic Force Microscopy opened up the possibility of measuring van der Waal's forces in metallic systems, and the technique have been used to study forces in gold [71, 77]. The accuracy of using an AFM to measure such forces in metals has been reasonably well established by these studies.

The theoretical work by Lifshitz in this area is primarily developed for dielectric materials, [59, 79] and no specific theory (considering electron motion) had been developed for metals until recently. This held the comparison of the theoretical calculations to experimental data in some doubt. A recent van der Waal's theory for metals called the Coupled Plasmon Approach (CPA) [80, 81] takes into account the moving electrons in a metal.

In this study, we measured the vdW forces and work of adhesion in iron for the case where a spheroid particle or tip is in contact with a flat surface. The simulation of an iron particle in contact with an iron surface using an atomic force microscope cantilever was considered for its importance to the powder metallurgical industry in relation to the adhesive qualities of iron surfaces[1, 6]. A comparison of the experimental results is made with the Lifshitz vdW theory and the Coupled Plasmon Approach. An analysis of the adhesion properties is made using contact mechanics theory and force adhesion curves measured in the atomic force microscope.

3.1. Theory of van der Waal's forces

The fundamentals underpinning the origin of van der Waal's forces are well established [59, 79, 80], and in the context of this study it is only pertinent to refer to the basic understanding of dispersion forces.

3.1.1. The Origin of Dispersion Forces

Dispersion forces arise when two or more condensed matter systems are brought together, in such close proximity that the transient dipole moments of the zero-point quantal electron motions can polarise their respective electron clouds[82]. This interaction may be demonstrated by reducing the system to two interacting atoms separated by a distance D as pictured in **figure 3.1**, where the interaction potential is of the form

$$V(D) = -CD^{-6} \quad \text{(J)}. \tag{3.1}$$

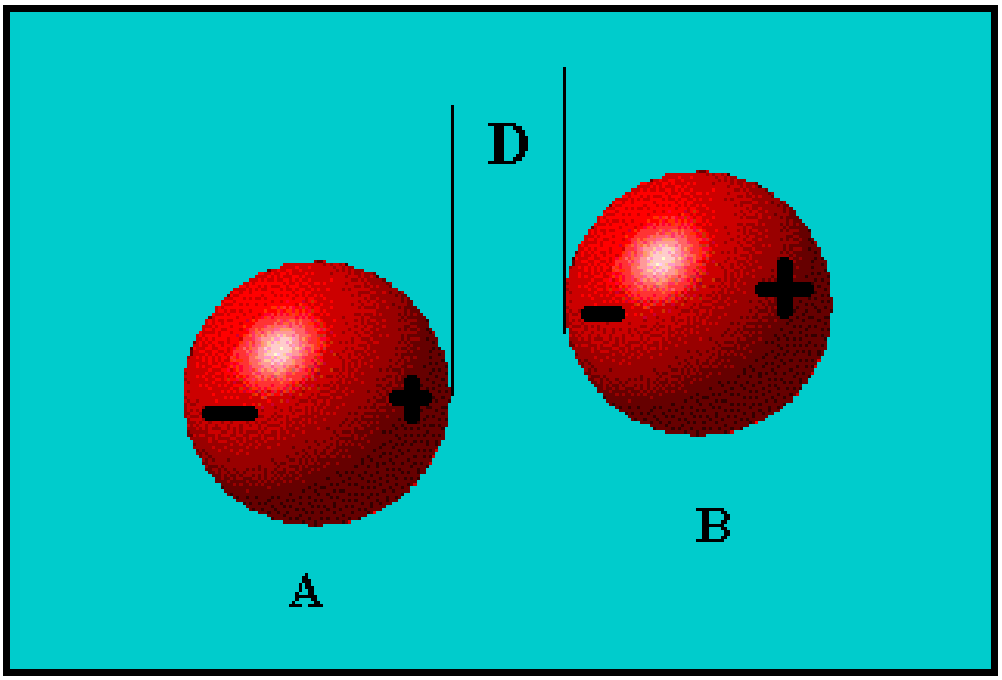

Figure 3.1: A system of two mutually polarised atoms.

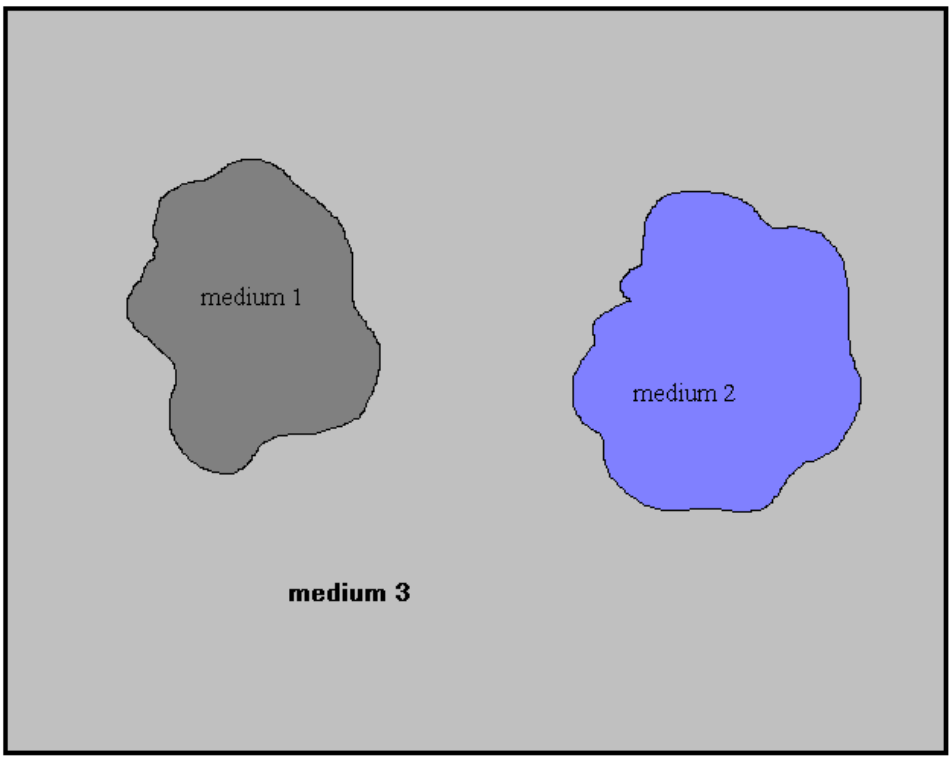

Figure 3.2: Two arbitrarily shaped dielectric condensed materials in some medium. The Hamaker constant relative to medium 1 or 2 can be calculated for the closed system of medium 1, 2 and 3 using Lifshitz theory.

The coefficient *C*, is the atomic Hamaker constant referring to a system of two isolated atoms in close proximity. The dipole moments generated as the electron cycles about the nuclei will not average to zero as higher order terms arise due to the coupling of atoms. Electron fluctuations between the atoms may initially induce a transient dipole moment in atom A. This dipole gives rise to an electric field with an inverse power relationship of D^{-3} at atom B, thereby producing a dipole by induction. The coupling of these fields results in the interaction potential relationship shown in equation one. This principle can be extended to condensed many-atom systems such as polymers, ceramics and metals.

3.1.2. Dispersion forces in condensed matter

The dispersion force encountered between two multi-atomic condensed-matter systems is dependent on the value of the Hamaker constant denoted *A*[59, 80]. The value of the Hamaker constant is a physical property calculated with respect to the system of interfaced materials in the medium and is independent of the geometry of the system.

According to the Lifshitz, the Hamaker constant for a given system is dependent upon the dielectric properties and refractive indices of the materials in the system. As an example, referring to **figure 3.2** if a system is made up of two arbitrarily shaped materials 1 and 2 brought close together and immersed in some medium (material 3), the Hamaker constant of the system is:

$$A = \frac{3}{4}kT\left(\frac{\varepsilon_1-\varepsilon_3}{\varepsilon_1+\varepsilon_3}\right)\left(\frac{\varepsilon_2-\varepsilon_3}{\varepsilon_2+\varepsilon_3}\right)+\frac{3}{8}\frac{\hbar\omega_p}{\sqrt{2}}\frac{\left(n_1^2-n_3^2\right)\left(n_2^2-n_3^2\right)}{\left(n_1^2+n_3^2\right)^{1/2}\left(n_2^2+n_3^2\right)^{1/2}\left\{\left(n_1^2+n_3^2\right)^{1/2}+\left(n_2^2+n_3^2\right)^{1/2}\right\}} \quad \text{(J)} \qquad (3.2).$$

Here ε_1 and ε_2 are the dielectric constants of the two materials interfaced, and ε_3 is the dielectric constant of the medium in which they are immersed. The values, n_1, n_2 and n_3 are the refractive indices of the two materials, and the medium respectively. The symbol $\hbar$ is Plank's constant and ω_p is the characteristic UV adsorption frequency (for dielectrics) or the plasma frequency (for metals) [83].

If the two materials being interfaced are identical, then the expression for the Hamaker constant reduces to:

$$A = \frac{3}{4}kT\left(\frac{\varepsilon-\varepsilon_3}{\varepsilon+\varepsilon_3}\right)^2 + \frac{3}{16}\frac{\hbar\omega_p}{\sqrt{2}}\frac{\left(n^2-n_3^2\right)^2}{\left(n^2+n_3^2\right)^{3/2}} \qquad \text{(J)} \qquad (3.3).$$

In the case of metals, the dielectric constants are treated as if they approach infinity and thus the term in parenthesis on the left equals one. The refractive index in the term on the right is a complex quantity for metals, and this term will factor out when evaluated from first principles [59]. The term on the left in the case of metals is out-weighed by the term on the right by two orders of magnitude, and so the expression for the Hamaker constant for a system of two metals in a vacuum or a medium of low refractive index reduces to:

$$A \sim \frac{3}{8}\frac{\hbar}{\sqrt{2}}\frac{\omega_{p1}\omega_{p2}}{\omega_{p1}+\omega_{p2}} \qquad \text{(J)} \qquad (3.4).$$

Where ω_{p1} and ω_{p2} are the plasma frequencies of the two metals.

3.1.3. Dispersion forces in metals (The Coupled Plasmon Approach)

The Coupled Plasmon Approach (CPA) is derived for metals as it models for free electrons [81, 82]. The limitation in applying this theory at this stage is that no general equation for a particular Hamaker constant has been evaluated.

Consider a condensed body comprised of a system of plasmons[6]. The finite separation dependent zero-point energy of plasmons is:

$$\Delta E = \frac{\hbar}{2}\sum_{j}\delta\omega_{p}^{j} \qquad \text{(J)} \qquad (3.5).$$

Where $\{\omega_p^j\}$ is the set of electron plasmon frequencies of the combined coulomb-coupled system. ΔE is the change in the ground state energy. In the case of metallic interfacial systems that are separated enough to prevent electron cloud overlap, it is possible to obtain ΔE analytically for particular geometries using the hydrodynamic approximation as described by Dobson [82].

According to Dobson, the particular equation of the interaction energy between two flat infinite metallic slabs is[80, 81]:

$$W_{CPA} = -5.522\times10^{-3}\frac{\hbar\omega_{p}}{\sqrt{2}D^{2}} \qquad (\text{Jm}^{-2}) \qquad (3.6)$$

Where D is the separation distance between the slabs.

[6] A plasmon is a collective excitation for quantised oscillations of electrons in a metal obeying Bose-Einstein statistics.

3.1.4. Comparison of Lifshitz Theory with CPA

It is pertinent to establish the quantitative difference between the Lifshitz theory and the Coupled Plasmon Approach. The interaction potential for two opposing planar surfaces according to the Lifshitz theory is[59]:

$$W_L = -\frac{A}{12\pi D^2} = \frac{3}{192\pi}\frac{\hbar\omega_p}{\sqrt{2}D^2} \qquad (\mathrm{Jm}^{-2}) \qquad (3.7).$$

Hence, the Coupled Plasmon Approach predicts a value for the interaction potential 10% higher than the Lifshitz theory for a given geometry.

If equation 3.6 and 3.7 are compared a general equation for the Hamaker constant for the coupled plasmon approach can be derived as follows:

Consider that $\frac{A}{12\pi D^2} = 5.522\times10^{-3}\frac{\hbar\omega_p}{\sqrt{2}D^2}$

$\therefore A \approx \frac{5}{24}\frac{\hbar\omega_p}{\sqrt{2}}$ or for two different metals interfaced together:

$$A \approx \frac{5}{12}\frac{\hbar}{\sqrt{2}}\frac{\omega_{p1}\omega_{p2}}{\omega_{p1}+\omega_{p2}} \qquad (\mathrm{J}) \qquad (3.4a).$$

One of the aims of this study was to compare both theoretical predictions with experimental data.

3.2. Experimental arrangement and analysis technique

The van der Waal's forces were measured on a Nanoscope Dimension Series atomic force microscope inside a fluid cell. The experimental arrangement is shown

schematically in **figure 3.3.** Three types of cantilever tips were prepared with a thin coating of iron inside a vacuum evaporation chamber. The cantilevers are coated with iron having a thickness of approximately 50 nm. Two of the cantilevers have an iron coated tungsten ball, and the other cantilever has only an iron-coated tip with an effective radius of 0.1 μm. The radii of the tips were measured visually in a Scanning Electron Microscope (SEM) for the 0.1 μm tip and under a high-resolution confocal optical microscope for the 3 and 7 μm tips shown in **figure 3.4**.

The spheroid tip is driven up and down towards an iron surface by a piezo-electric crystal at a rate between 1 - 10 Hz. The arrangement was submersed in Milli-Q water (6 times distilled) with a pH of 6.5 ± 0.5 at approximately 26°C. The iron surface and the AFM are both earthed, although electrostatic charging is not expected to be an issue under the water.

An iron spheroid tip is being brought into contact with a large flat iron plane, and the interaction force is measured. The surface of the iron plate was polished to an average roughness of < 0.1 μm since too much roughness will produce lateral twisting of the cantilever arms which will introduce errors[71]. In order to minimise oxidation, measurements on the AFM were taken within 30 minutes of the iron coatings being applied to the cantilevers and polishing of the iron substrate.

The type of cantilever used is a silicon nitride "V" shaped contact mode cantilever tip. The tips were calibrated with a spring constant of $k \approx 0.3 \pm 0.02$ by a mass-resonance frequency method [84]. In this method, a mass (M_l) is loaded on a cantilever and its natural resonant frequency (ν_l) is obtained inside the AFM holder. The cantilever

without a mass is then placed inside the AFM and its resonant frequency (ν_0) is determined. The cantilever constant is calculated from the equation:

$$k = (2\pi)^2 M_l \left(\frac{\nu_l^2 \nu_0^2}{\nu_0^2 - \nu_l^2} \right) \ (\mathrm{Nm^{-1}}) \qquad (3.8).$$

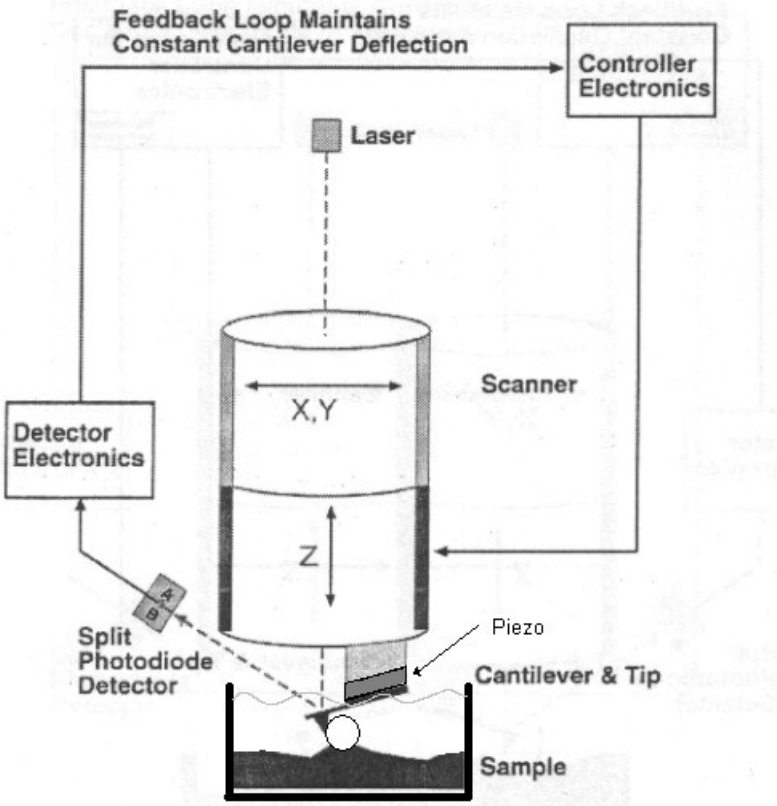

Figure 3.3: An iron coated cantilever tip and ball are driven alternately towards the surface by a Piezo-electric crystal between 1 – 10 Hz. The entire cantilever is immersed in water, the fluid cell being an attached component making an extension away from the piezo crystal, and is shielded by a rubber cap.

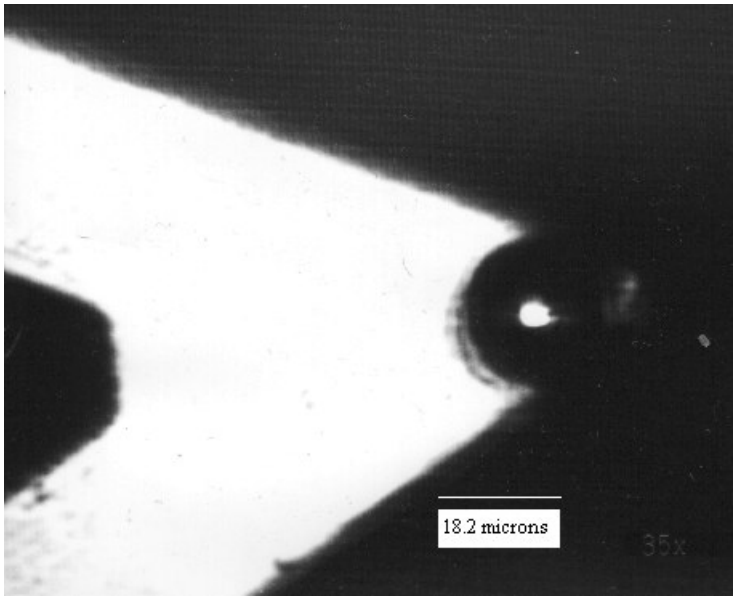

Figure 3.4 (a)

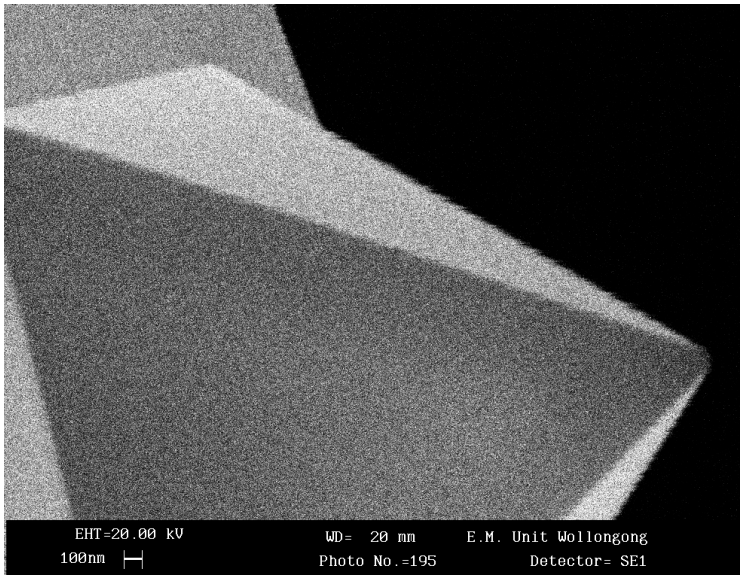

Figure 3.4 (b)

Figure 3.4 a-b: The images of the AFM cantilever tips, taken using high resolution confocal microscopy and Scanning Electron Microscopy. a) R = 7microns b) R = 0.1 microns.

3.2.1. Data analysis technique

Once an understanding of the regions or parts of the force curves is obtained, force-distance relationships can be made. In this work, the interpretation of various components of the force curve is made after Ducker and co-workers [72] and Biggs and co-workers [71]. This is shown schematically in **figure 3.5**.

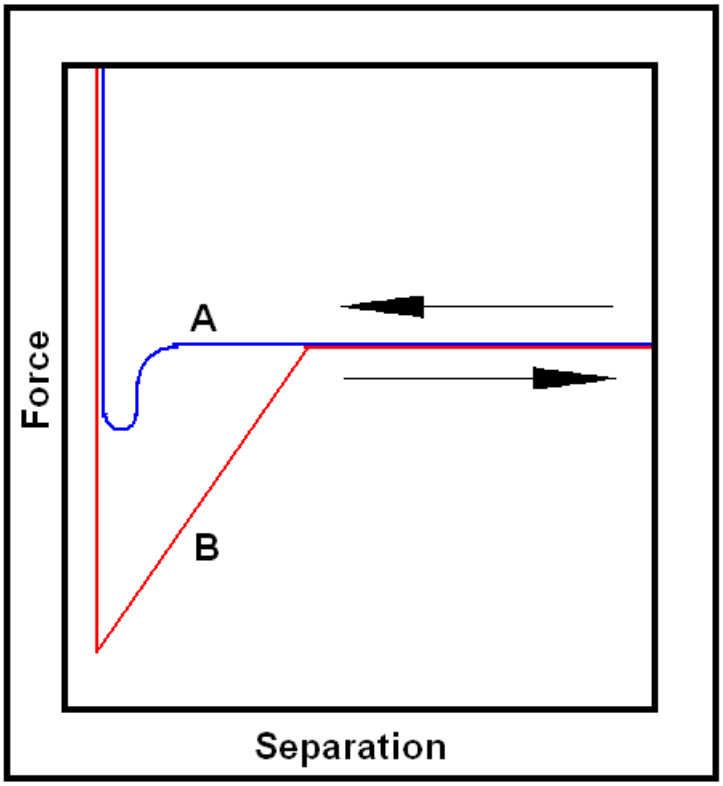

Figure 3.5: The various regions of the force curve as measured by the atomic force microscope shown in schematic.

The curve "A" marked with the arrow indicating to the left is the approaching (jump in contact) curve and the curve "B" marked with the arrow indicating to the right is the retracting (adhesion) curve. The vertical line to the far left is the called compliance region where full contact with the surface is made. This is considered to be the point of zero separation. The horizontal lines to the right are the approaching and retracting regions where no force is encountered by the tip. Curve "A" shows the jump to contact region immediately after the curve bends down sharply. The x-axis depicts the

separation of the cantilever from the surface. The y-axis depicts the force experienced by the cantilever as the cantilever stiffness resists the force. If measured by the method previously mentioned, the cantilever tip will have a known spring constant. The deflection is measured initially and then the force with respect to distance experienced between the tip and surface can be measured by applying the force equation $F = -kx$, where x is the cantilever deflection.

It is possible to acquire an approximate value of the Hamaker constant using the experimental data via a semi empirical technique. Taking the interaction potential for two planar surfaces the force equation can be obtained using the Derjaguin approximation [59]. The Derjaguin approximation for a plane surface and a sphere is:

$$F(D) \approx 2\pi R W_L(D) \qquad \text{(N)} \qquad (3.9).$$

Where $W_L(D)$ is the interaction potential from equation 3.7 between two planar surfaces. Placing equation 3.7 into equation 3.9 gives:

$$F(D) = -\frac{AR}{6D^2} \quad \text{(N)} \qquad (3.10)$$

Upon approaching the surface, as the cantilever tip begins to experience the interaction force between itself and the surface, the cantilever will begin to deflect. As the gradient of the interaction force exceeds the limit of the spring constant the tip will jump in contact to the surface. Mathematically, this is represented as:

$$\nabla F(D) = \frac{AR}{3D^3} \geq k \qquad (\text{Nm}^{-1}) \qquad (3.11)$$

then jump in contact will occur. The distance $D = D_j$ where D_j is the jump in contact distance when k (the cantilever force constant) is equal to the force gradient. If the spring constant is known and the tip radius is known the Hamaker constant A can be found by rearranging equation 3.11, thus:

$$A \approx \frac{3kD_j^3}{R} \qquad \text{(J)} \qquad (3.12).$$

3.3. Results and Discussion of van der Waal's forces

The atomic force microscope produces a deflection verses separation curve for each sample and records the points into a data file. The data points can then be converted into a force versus separation plot, provided the cantilever constant and radius of curvature are known. In the case of the van der Waal's experiments, measurements were performed in pure iron with two tip sizes, one with a tip radius of 0.1 μm and the outer a tip radius of 3 μm. The results are plotted in **figure 3.6 a-b**.

The graphs are plotted as the Force divided by the tip radius (F/R) with respect to the separation. Indicated on the graph is the point where the jump in contact occurs. The magnitude of F/R at the jump in contact point is smaller with a large tip radius (3 μm) than it is with a smaller tip radius (0.1 μm). This finding is in agreement with earlier work on gold/gold contacts [71]. It was pointed out in the study on gold, that the smaller value of the absolute force for the smaller tip radii is more sensitive to vibrational noise. This was also true in this work, as the data obtained when using the smaller tip radius had more scattering in the plot, and the transition where the cantilever jumps into contact with the surface is less defined.

The determination of the distance where the cantilever makes a "jump into contact" (JIC) to the surface takes a measure of interpretation. As shown in equation 3.12, the Hamaker constant can be estimated by knowing the cantilever spring constant, the radius of curvature of the tip and the jump to contact distance.

The radius of curvature and the spring constant were obtained as earlier described. The jump in contact distance can be estimated from the approaching curve of the force data by treating the graph analogous to a BODE plot. A BODE plot is typically applied to circuit theory. A BODE plot in circuit theory is used to measure the frequency of a sinusoidal voltage input at the limit of a circuits voltage gain (decibels dB) as it responds to that input [85]. Analogous to this, we can that the van der Waal's force is the "input" into the cantilever. The cantilever produces a response according to the cantilever stiffness. The limit of the cantilevers response to the force input is where the gradient of the force field exceeds the cantilever spring constant and jumps into contact with the surface. Tangents should be inscribed along the horizontal data and on the data where it starts to rapidly slope away along the asymptote, as shown in **figure 3.6**. The point where the two tangents meet is known as the 3dB point in circuit theory. This is analogous to the "Jump in Contact" (JIC) point here.

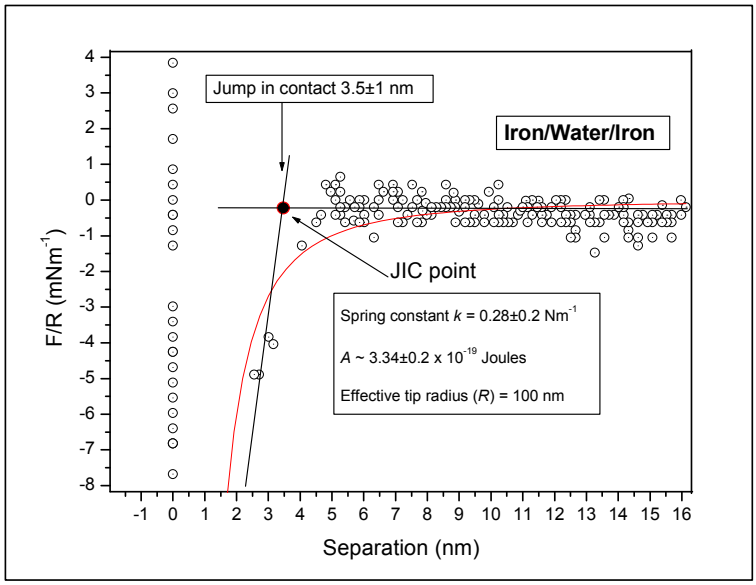

Figure 3.6 (a):

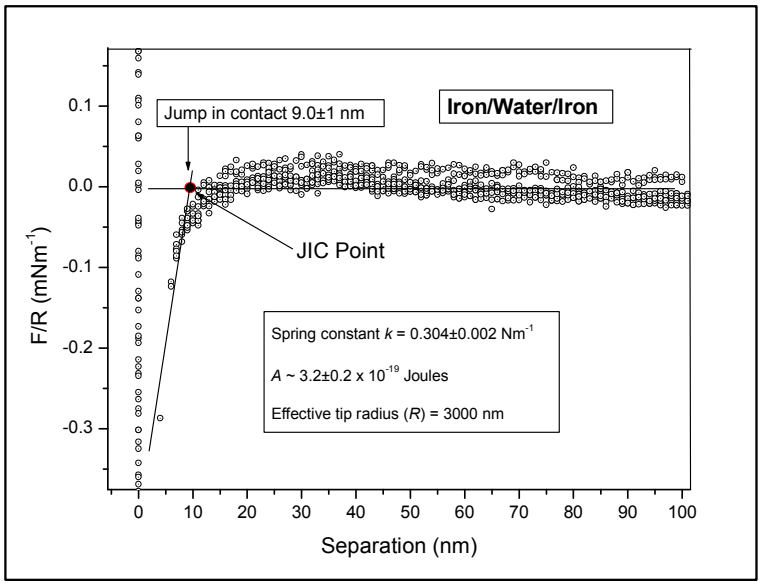

Figure 3.6 (b):

Figure 3.6: The force distance curves for the van der Waal's attraction between two iron surfaces obtained by atomic force microscopy.

3.3.1. Comparison with theoretical values

When determining the Hamaker constant from experimental data, variables in the system such as the cleanliness of the surfaces, the purity of the materials, vibrations and electrostatic noise can give rise to errors. Consider the value of the Hamaker constant in iron with the 0.1 μm tip. The experimentally determined result for the Hamaker constant here could fall between 3.2 - 3.34 $\times$ 10^{-19} J. This value is close to the theoretical prediction of the Lifshitz theory and the CPA (see **table 3.1**). The Hamaker constant predicted, and experimentally measured for gold are also shown in **table 3.1**. In both cases, there is good agreement between the theoretical predictions and the experimentally determined values.

Table 3.1: Calculated and semi-empirical values of the Hamaker constant for iron and gold.

Please see print copy for Table 3.1

The 0.1 μm tip system measures a Hamaker constant that is closer to the theoretical value, and closer to an expected value for a metal in general. Using the separation distance at the jump to contact, substitute equation 3.11 into equation 3.10, then it is possible to show that the value of the largest force measurement obtainable before jump in contact is:

$$\left|\frac{F}{R}\right|_{\max} = \frac{1}{6}\left(\frac{3A^{1/2}k}{R}\right)^{2/3} \quad (\mathrm{Nm}^{-1}) \qquad (3.13).$$

Assuming the Hamaker constant to be close to the theoretical value, then the maximum F/R at jump in contact should be $F/R \sim 0.5\text{mNm}^{-1}$ for a 3 μm tip. If you apply this value for F/R back into equation 3.10 this implies a jump in contact distance close to 8-10nm. Following the same calculation for the case of the 0.1 μm tip the value is approximately $F \sim 0.4\text{nN}$, implying a jump to contact distance of 3-5 nm.

3.3.2. Magnetic effects

When working with ferromagnetic material it is important to determine if magnetic forces influence the magnitude of the force distance relation. The only magnetic field available to induce a magnetic field in the tips is the Earth's magnetic field ($\sim 0.5 \times 10^{-4}$ T)[86]. Order of magnitude calculations can be made for each sphere to find the force induced by the Earth's magnetic field[87, 88].

The simplest way to arrive at some approximate value of a magnetic force in this case is to consider the force between two spherical magnetic particles with some value for the magnetic flux density $\boldsymbol{B}$. Tholen and Yao offer an equation for the case of two magnetised spherical iron particles with their magnetic poles axially aligned, coming into contact from a distance[89]:

$$F_m = \frac{8\pi}{3}\frac{B^2}{\mu_0}\frac{r^6}{d^4} \qquad \text{(N)} \qquad (3.14).$$

$\boldsymbol{B}$ is the magnetic flux density, (μ_0) the permeability of free space, r sphere radius and d is the centre-to-centre separation between the particles. A derivation of equation 3.14 is offered in **appendix 1**.

The equation for the force between two magnetised spherical particles in equation 3.14 is limited by the assumption that the particles are at a separation $d >> r$. In the case where the particles are in contact ($d = 2r$) equation 3.14 reduces to:

$$F_m(r = 2r) = \frac{\pi}{6}\frac{B^2}{\mu_0} r^2 \qquad \text{(N)} \qquad (3.15).$$

Values for the magnetic force derived from this equation are only order of magnitude approximations. The value of ***B*** in this experiment can be considered to have an effective strength no greater than the earths magnetic field sine no other magnetic field is present to induce a higher value in the iron. It is also important that the particles not be too small that they constitute a single domain particle. It can be shown that for a sperical ferromagnetic particle of radius r, the critical radius R_c for it to become a single domain magnetic particle is[88]:

$$R_c \leq \frac{9\gamma_{DW}}{\mu_0 M_s^2} \quad \text{(m)} \qquad (3.16)$$

where the domain wall energy is γ_{DW} = 3.8x10^{-3}(Jm^{-2}) and the saturation magnetisation is M_s =1.74x10^6 (Am^{-1}). This gives a value for R_c = 10nm. The radii on the cantilever tips used in this experiment are much larger than 10nm and so they are not expected to be a single domain magnetic particle. If the magnetisation was at saturation the magnetic flux density will have the value B = 2.15 Tesla[86]. If it were the case that the 0.1 and 3 μm particles are at saturation, the force between the particles near contact would be 19 nN and 17 μN respectively. These values for the force are orders of magnitude larger than those detected experimentally in the AFM and in fact are much greater than the force detected at contact (see **table 3.2**), implying that magnetic forces are not present.

If it is assumed that the particles are magnetised by the magnetic flux density of the earths magnetic field, then the maximum magnetic force that the 0.1 and 3 μm particles could experience even in contact with the substrate is ~10^{-17}N and ~10^{-14}N respectively. Forces of this magnitude could not possibly be detected by the AFM and so it is likely that the potential magnetic force from the iron tip was not a factor in this case. An even more conservative estimate to make is to consider that the iron tip was taken to saturation magnetisation and a magnetic remnant is left behind. The magnetic remanence for iron is B_r~0.1T[88]. If this value is used the values for the magnetic force are still of the order 10^{-11}N for the 100nm tip which is still too small to affect the value obtained. In the case of the 3 μm particle the value is higher at ~10^{-8}N. A field of this magnitude would certainly be detected if present however no such force was evident in the curve.

3.3.3. The Casimir force and the Casimir limit

There are two types of interatomic force, which arise between metal surfaces. Which attractive force is operating at the time, depends on the distance by which the surfaces are separated. In close range, the surface attraction is governed by the electrostatically polarising van der Waal's force. This force can go by the name of dispersion or van der Waal's force as mentioned earlier.[80, 82] The other attractive force is called the Casimir force. This force governs the attractive interaction of the surfaces at long range and is analogous to the retarded van der Waal's force for dielectric materials. The Casimir force is established by the electromagnetic standing wave pressure between the two metal surfaces resulting from the zero-point quantum electron fluctuations described earlier.[90] The Casimir force is governed by a weaker force-distance power

law to the van der Waal's force (compare references[80, 90, 91]). To determine at what distance the Casimir force governs the surface interaction, one is required to calculate the so-called Casimir limit. The Casimir limit is the distance where dispersion forces give way to Casimir forces.

If the sphere is too large, the jump to contact, as implied by equation 3.12, will occur at a distance greater than the Casimir limit. Since the Casimir force arises from the standing wave of the quantum electron fluctuations (or the plasma frequency ω_p), then the distance where Casimir force will begin to operate will be $D_{cross} = c / \omega_p$ where c is the speed of light and ω_p is the plasma frequency of the metal. If this occurs, then it is uncertain as to whether the force of attraction is van der Waal's forces and hence the Hamaker constant cannot be measured. In the case of iron the Casimir limit is $D_{cross} \approx$ 13nm. The largest jump to contact distance measured was for the 3μm tip of ~9nm. This suggests that the forces acting were still van der Waal's forces.

3.3.4. Oxidation monolayers

Although great care was taken to keep the surfaces free of contaminants and oxidation, there is little doubt that an oxide layer had formed on the surface of the iron during the experiment. Data on the formation of oxide layers in the iron system indicates that in air, under atmospheric conditions, a layer of oxide will form on an iron surface of approximately 1-1.5nm within 30 minutes. The relationship of oxide thickness to time is logarithmic and so the thickness of the oxide will be double this (3nm) after 20 hours[92]

This being the case, we are essentially left with a two-part system of a thick iron specimen with a thin slab of oxide on top. The dispersion field produced by a particular material is dependent on its geometry[59]. In the case of two thin slabs of insulating material separated by a distance D, the van der Waal's energy reduces as C/D^4 (where C is constant) providing that the thickness of the insulator $L < D$[93]. In the case of two thick slabs of metal or insulating material where $L > D$, the van der Waal's energy reduces as K/D^2 (where K is constant). The cofactor C for a thin slab is less than cofactor K[82]. Since C<K and if $D << 1$ then $1/D^2 >> 1/D^4$ the energy of the thin slab will diminish much faster than the thick slab.

Consider then, the system of a large iron sphere coated in a thin layer of iron oxide. The van der Waal's field due to the thin oxide (given its power law) will be negligible in comparison to the thick iron sphere. This will be the case until the sphere is at a distance that is comparable to the thickness of the oxide. In the case of the present experiment, that distance is 1-1.5nm. The force distance relations shown in **figure 3.6** indicate jump to contact distances of 3 – 9nm. In effect, the van der Waal's force of the iron oxide thin slab is negligible compared to the iron sphere up until a separation of ~1.5nm where it operates on a $1/D^4$ relationship. It can be assumed then, that the van der Waal's force of the iron sphere is that force which is governing the region of the curve where jump to contact occurs is strongly dominated by the vdW field arising from the bulk metal in accordance with equation 3.10 and 3.12.

3.4. Adhesion

An understanding of the adhesion properties induced by van der Waal's forces is important in understanding the adhesion between iron particles in powder metallurgy. The van der Waal's forces being thought to play a role in the early stages of sintering[68], makes it relevant to obtain a general quantity of the work of adhesion between iron particles.

3.4.1. Theory of Adhesion

To evaluate the adhesive stress and the size of the contact areas between particles, there are two main theories that deal with contact mechanics in elastically deforming systems. Each theory describes a limiting cases. The Johnson-Kendall-Roberts (JKR) theory describes systems of relatively low Young's modulus and large particle radius[94]. The other is the Derjaguin-Muller-Toporov (DMT) theory, dealing with small particles with a high Young's modulus[95].

The Tabor parameter μ can give an index to evaluate what theory is most applicable for what system[96]. The Tabor parameter is given by:

$$\mu = 0.86\left(\frac{64R\gamma_s^2}{9K^2z_0^3}\right)^{1/3} \qquad (3.17).$$

Here z_0 is the lattice parameter or atomic spacing, γ_s is the surface tension, R is the particle or cantilever tip radius and K is the reduced Young's modulus

$K = 4/3\left(\frac{(1-\nu_1^2)}{E_1} + \frac{(1-\nu_2^2)}{E_2}\right)^{-1}$. Here, E_1 and E_2 are the Young's moduli of the two particles and ν_1 and ν_2 are their respective Poisson ratios. This parameter measures a particles size in relation to its elastic hardness and will ultimately determine the particle contact area and adhesion stress applied by a given force.

In general, when $\mu < 0.1$ the DMT theory is used. If $\mu > 5$ then JKR theory is used. At room temperature of 25 °C the values derived for iron/iron contacts for the sphere sizes of 0.1 μm and 3 μm, $\mu \sim 1.7$ and 4.9 respectively. These values fall between the ranges of the DMT and JKR theories.

Schwarz derived a general theory of contact mechanics [97] that accounts for particle systems in contact with a planar surface where the Tabor value can lie in the DMT limit, the JKR limit or in between these two limits as is the case for the systems studies here. A brief outline and rational of the theory will be given.

Consider a sphere in contact with a flat surface as in **figure 3.7**. In the absence of an externally applied load, surface area contact is maintained by the van der Waal's force F_c. The van der Waal's force gives rise to a work of adhesion. The work of adhesion is given by:

$$\gamma_w = \gamma_1 + \gamma_2 - \gamma_{1-2} \qquad (\mathrm{Jm}^{-2}) \qquad (3.18).$$

In the case where the two materials are the same and when in contact they form an ideal van der Waal's solid the interaction term $\gamma_{1\text{-}2} = 0$. The work of adhesion is then equal to twice the surface energy of the material. A van der Waal's solid is one where the interaction at the interface is governed by van der Waal's forces alone and no medium or other interaction forces lie between the interface. The particles in a van der Waal's

solid are bound together by van der Waal's forces alone as in the case of dipole-dipole forces in ice.

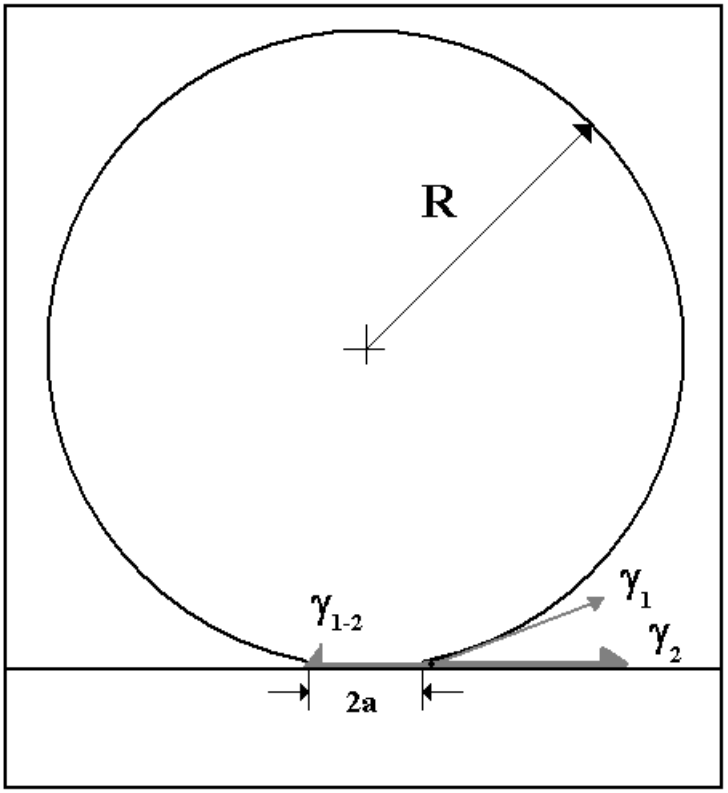

Figure 3.7: An ideal contact between an elastically deforming sphere and a flat surface. The γ_1, γ_2 and γ_{1-2} indicate the surface tension of the spherical surface, the flat surface and the boundary tension between the sphere and the surface respectively. The diameter of the contact area is 2a and the radius of the sphere is R.

The interface between two metals does not behave as a van der Waal's solid, rather it is more like an interfacial grain boundary. In theory, a metallic interface is governed by the interplay between van der Waal's forces and the short ranged forces responsible for atomic binding.

The van der Waal's force when the particle is in contact with the solid surface is given by;

$$F_c = -\tfrac{3}{2}\pi R\gamma_{w1} - 2\pi R\gamma_{w2} = \tfrac{1}{2}\pi R\gamma_w\left(\tau^2 - 4\right) \qquad \text{(N)} \qquad (3.19).$$

The first term is the contact force experienced in the case where the system is completely in the JKR limit, and the second term describes a system completely in the DMT limit. The terms γ_{w1} and γ_{w2} are the fractions of the work of adhesion, depending on whether the system is described by JKR or DMT. If the system is fully described by JKR for instance, $F_c = -\frac{3}{2}\pi R\gamma_{w1}$ and $\gamma_{w1} = \gamma_w$ and $\gamma_{w2} = 0$. The converse is true if the system can be described by the DMT model. If the Tabor parameter indicates that the system lies between these two limits, then the work of adhesion is portioned out accordingly between γ_{w1} and γ_{w2}.

Schwarz has shown that, given an elastic interaction between the particle and the surface in the absence of an external loading force, the radius of contact is given by[97]:

$$a = \left(\frac{R}{K}\right)^{1/3}\left(\tau\sqrt{\frac{3}{2}\pi R\gamma_w} \pm \sqrt{\left(2-\frac{\tau^2}{2}\right)\pi R\gamma_w}\right)^{2/3} \quad \text{(m)} \quad (3.20).$$

And the adhesion pressure distribution across that contact is given by;

$$\sigma(r) = \frac{3Ka}{2\pi R}\sqrt{1-\left(\frac{r}{a}\right)^2} - \tau\frac{\sqrt{\frac{3K\gamma_w}{2\pi a}}}{\sqrt{1-\left(\frac{r}{a}\right)^2}} \quad (\text{Nm}^{-2}) \quad (3.21).$$

The parameter τ indicates the degree to which μ is between 0.1 and 5, and has a value between 0 and 1. In other words τ indicates how close a system conforms to the JKR

limit or how closely it conforms to the DMT limit. If $\tau = 1$ the JKR limit dominates and if $\tau = 0$ the DMT limit dominates. It can be shown that:

$$\tau(\mu) = \begin{cases} \dfrac{\mu - 0.1}{4.9} & (0.1 \le \mu \le 5) \\ 0 & (\mu \le 0.1) \\ 1 & (\mu \ge 5) \end{cases}$$

An approximation mentioned by Hao[73] and later clarified by Schwarz[97] is that the work of adhesion is given by:

$$W_{L0} \sim \frac{F_{ad}}{1/2\,\pi R(\tau^2 - 4)} \sim \frac{A}{3\pi(\tau^2 - 4)D_0^2} \quad (\mathrm{Jm}^{-2}) \qquad (3.22)$$

where D_0 is called the equilibrium distance between the surfaces. This approximation can be further refined taking into consideration short ranged repulsive energy due to electron wave-function overlap. This potential energy is also accountable for atomic binding. An empirical expression used to model the close range interaction potential of two similar metal surfaces[59, 98, 99] is:

$$W_{BE} = -2\gamma_s\left(1 - \frac{(D - z_0)}{\lambda_M}\right)\exp\left(-\frac{(D - z_0)}{\lambda_M}\right) \quad (\mathrm{Jm}^{-2}) \qquad (3.23)$$

where λ_M is the Thomas-Fermi screening length[83, 99] and z_0 is effectively the atomic lattice parameter. The balance between the van der Waal's energy and the atomic binding energy that becomes repulsive at short range (approximately $D < 2z_0$ for iron) is ultimately the work of adhesion between the two contacting surfaces. The theoretical expression for the work of adhesion is:

$$\gamma_w(D_0) = W_{BE} + W_{CPAorL} \quad (\mathrm{Jm}^{-2}) \qquad (3.24).$$

This equation is a more generalised equation of the work of adhesion. Here W_{CPAorL} is the van der Waal's energy using the CPA or Lifshitz theory. Extending this principle to the van der Waal's force distance relation and applying the Derjaguin approximation once again from equation 3.9, the more general force distance relation describing a spherical particle and a flat surface can be obtained:

$$F(D) = 2\pi R\left[-2\gamma_s\left(1-\frac{(D-z_0)}{\lambda_M}\right)\exp\left(-\frac{(D-z_0)}{\lambda_M}\right)+\frac{A}{3\pi(\tau^2-4)D^2}\right](\mathrm{N}) \qquad (3.25).$$

This expression gives an approximate value of the equilibrium separation D_0 between the surface and the sphere. This value can be found graphically as in **figure 3.8** where the equilibrium separation is at the minimum of the curve. The theoretical work of adhesion is then given by the energy at the equilibrium separation.

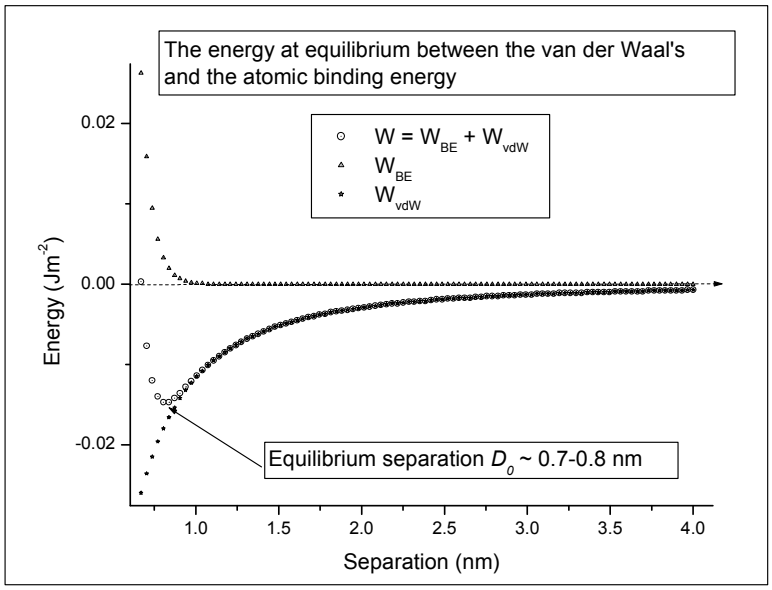

Figure 3.8: The van der Waal's adhesion energy graph including the repulsive energy curve. The minimum of the curve shows the equilibrium separation.

The above theory shows a single energy distance relation in equation 3.24, where only the Hamaker constant A, the Fermi screening length λ_M, the lattice constant and basic

material properties are required such as the Young's modulus and the surface tension. The work of adhesion for the particle in contact with a surface is constant in the JKR or DMT limit, and varies slightly when passing between these two limits. The results for the work of adhesion using the above theory are shown in **table 3.2**.

3.4.2. Experimental measurements of the work of adhesion

The crucial value in determining the radius of contact and the adhesion stress between a sphere and a flat surface is the work of adhesion arising from the van der Waal's force. In practice, the measurement of the adhesion at the interface is also potentially affected by surface roughness, impurities and barrier-layers.

There can be much confusion as to the interpretation of the various regions of adhesion curves as measured by the atomic force microscope. The author here will give an interpretation of the force-adhesion curve using the adhesion curve obtained for the 100nm AFM tip.

Consider the curve shown in **figure 3.9**, comparing it to the schematic curve in **figure 3.5**. In **figure 3.9a**, the part of the curve labelled "A" shows the point where the cantilever is first measured by the AFM to be in contact with the surface. The schematic in **figure 3.5** shows this line to be perfectly vertical. This would be the case if the tip did not penetrate the surface, or if there were no deformation of the tip or surface that is to say if the tip and surface were infinitely hard. The experimental curve in **figure 3.9** indicates that there is some deformation. In the case of the adhesion curves (pulling off the surface) measured experimentally, the following interpretation is

suggested: the tip and surface are undergoing mutual deformation according to the principles of contact mechanics, as they are principally composed of the same material and thus one surface is not significantly harder than the other. At the point "A", there is a net positive loading force measured by the AFM as the piezo scanner overextends after contact is made with the surface. In **figure 3.9b**, on the point of the curve labelled "B", the net force experienced by the cantilever is zero. At this point, the degree deformation of the tip is shown on the right hand diagram before it is lifted off the surface and the adhesion force measured. In **figure 3.9c**, at the point on the curve labelled "C", the maximum adhesion force is measured. This is the exact point where the tip is released by the adhesive pull of the surface and returns to a net zero force as the piezo scanner retracts at point "D".

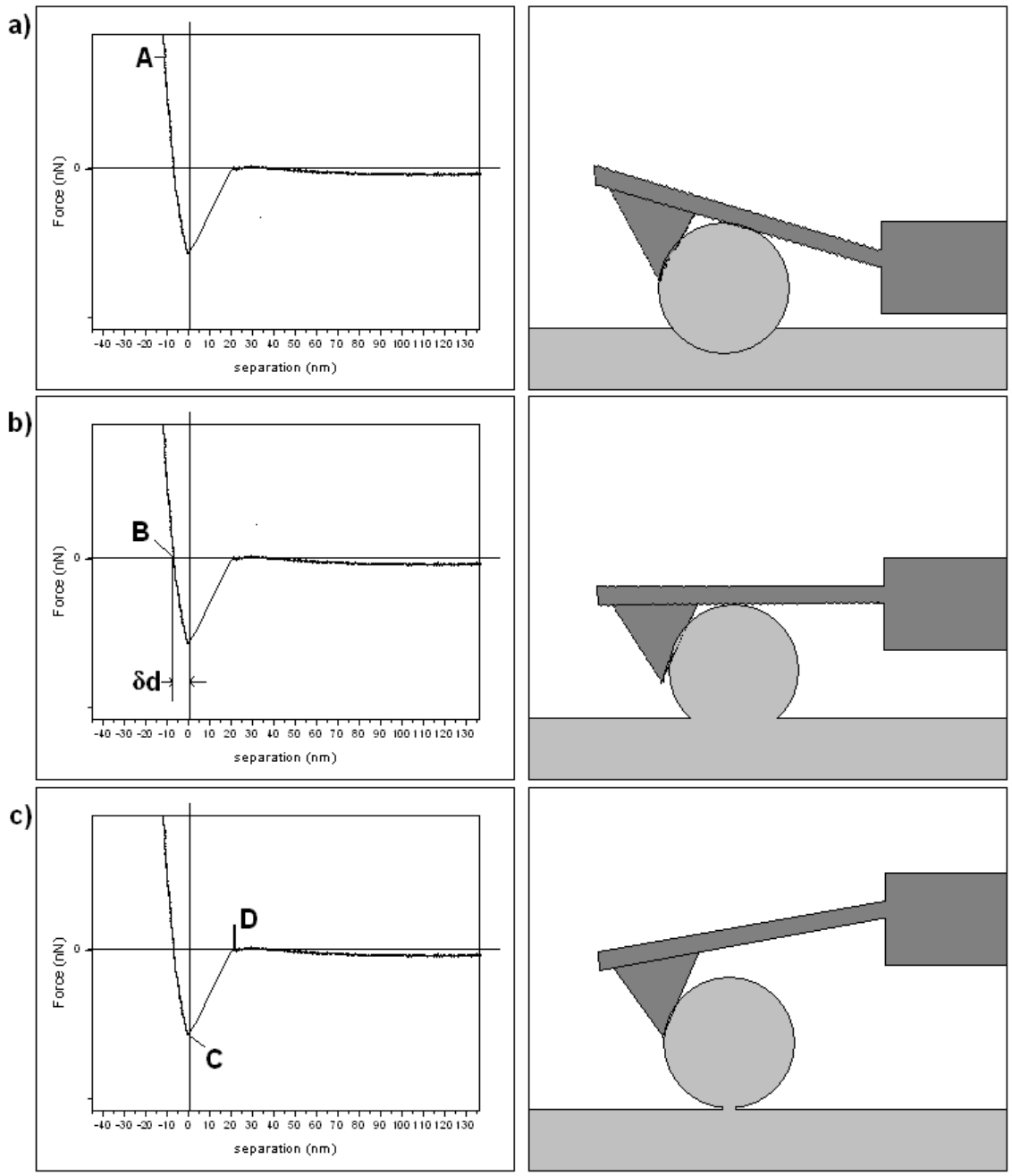

Figure 3.9: The various regions of and experimental force adhesion curve measured by atomic force microscopy.

The depth of deformation δd of the sphere can be approximated by measuring the negative separation at the point "B" on the curve in **figure 3.9b**. Applying geometry, the radius of contact and hence the surface area of contact can be calculated (see **figure 3.10**).

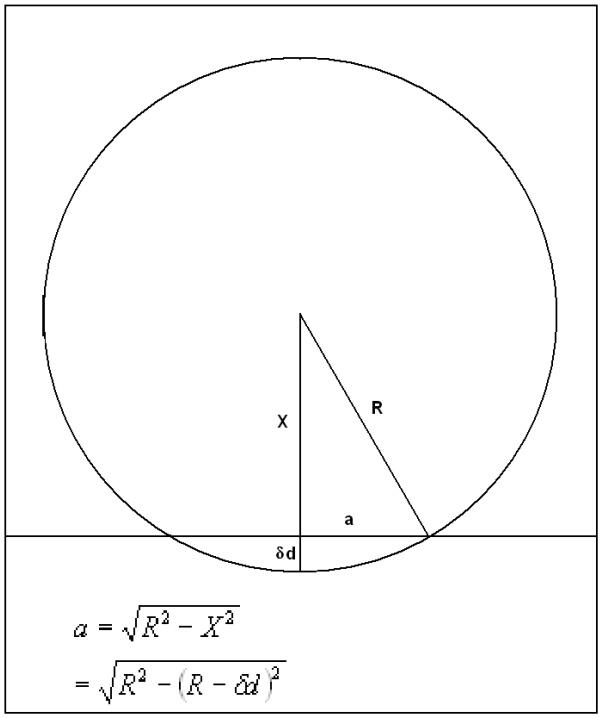

Figure 3.10: The geometry of the effective deformation when a tip is in contact with a surface in the AFM.

The theoretical values for the work of adhesion can be calculated as mentioned above by equation 3.24. Adhesion curves were measured experimentally for particle radii of 0.1, 3 and 7 μm respectively. There are at least two ways of deriving the work of adhesion using the adhesion force curve. The maximum value of the force of adhesion F_{ad} (point "B" on the graph in **figure 3.9**) can be used to derive the effective work of adhesion in conjunction with equation 3.22. This is a semi-empirical method using experimental data and contact mechanics theory. Results using this method are shown in **table 3.2**.

The other method is to evaluate the area of the curve in the interval where adhesion force is measured by the cantilever. The area of the curve to be measured is illustrated

in **figure 3.11**. This is the work done by the cantilever in resisting adhesion in this interval of separation.

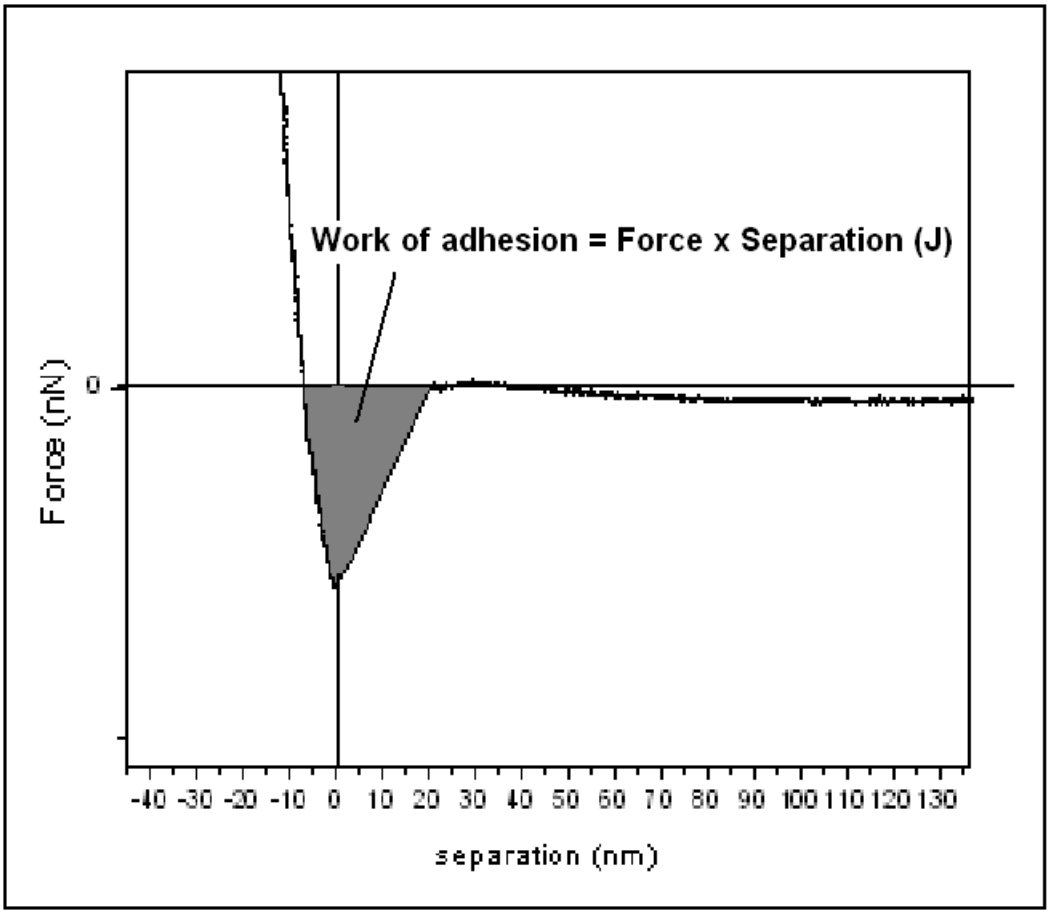

Figure 3.11: The measurement of the work of adhesion (Joules), from the force-adhesion curve using atomic force microscopy.

Since the deformation depth of the tip is measured from the graph, by geometrical arguments in **figure 3.10**, the radius of contact and hence the contact area can be approximated. This will yield an experimental measure of the work of adhesion in units of Joules per square meter. The results of these are shown in **table 3.2**.

Table 3.2: Force adhesion and work of adhesion values for three particle radii. [a] Theoretical values using equation 3.24. [b] The maximum force of adhesion experimentally derived. [c] The work of adhesion using the maximum forces of adhesion and equation 3.22. [d] The experimental values for the work of adhesion taking the area under the curve.

Please see print copy for Table 3.2

3.4.3. Discussion of adhesion

Measurements were taken across multiple curves for all three particle sizes and averaged and are given in **table 3.2**. The results in the table suggest that, given a system consisting of a sphere of any radius and a flat plane, in theory, the work of adhesion is similar. In principle, the only variance in this value is whether or not the system obeys the DMT or the JKR limit. In the case of the 100nm tip radius, the theoretical work of adhesion is a little different to the values calculated for the 3 and 7μm tip radius. This difference is due to the fact that the 100nm tip falls between the JKR and DMT limits. The 3 and 7μm tips are in the JKR limit and they display identical works of adhesion. It is understood here that the theory describes and ideal sphere and a flat surface in contact and that the sphere and surface undergo prefect elastic deformation.

In the case of the values using the maximum pull off force and equation 3.22, the system is modelled also as an elastically deforming sphere, however it is using an experimental value of the adhesion force. This method will be called method A in determining the work of adhesion. The experimentally derived results for the work of adhesion by the reasoning illustrated in **figure 3.9** and **figure 3.11** employ one

assumption that the sphere may be elastically or plastically deformed, however the deformation shape follows the geometry shown in **figure 3.10**. This will be referred to as method B.

The results for both methods are compared to the theory in **table 3.3**. The comparison shows the factor by which the measurements deviate from the applicable theory normalised to 1.

Method A shows a small variation for the 0.1μm from the theory of a factor of 1.35. In the cases of 3 and 7μm tips the deviation is larger. It varies by almost an order of magnitude for the 3μm tip and by a factor of 3.27 for the 7μm tip.

Table 3.3: The variation from theory of the values of the work of adhesion derived using two methods of measuring.

	Theory	Method A	Method B
0.1μm	1	1.52	1.66
3μm	1	11.02	3.06
7μm	1	3.71	2.36

Method B shows a slightly higher deviation from the theory in the case of the 0.1μm tip than method A. However, for all three tip sizes, the variation from the theory is consistent, varying by only a factor of 2-3 across the three tip sizes. It is not so much the smaller deviation from the theory that method B shows, but the greater consistency of measurement across the different tip sizes that implies its greater reliability over method A.

In the case of method A and B, the deviation from the theory is expected. The surfaces in real systems will display some roughness and will not necessarily deform elastically.

Analysis of the surface suggests that a complete theoretically ideal contact with the surface is unlikely. Conventional polishing techniques are capable of producing a surface from 10 – 100 nm in average roughness. A typical analysis of the root-mean-square (RMS) roughness in our samples was approximately 12.5nm RMS. This could mean that the probe could have been effectively varying in distance from the surface as it sampled the adhesion force by up to 12.5 nm.

In practise, the probe-surface contact will appear as in **figure 3.12**. In one study of an *in situ* observation of adhesion between gold surfaces in a TEM-AFM set up, surface gold atoms were seen to gather towards the point of contact producing an accentuated catenary neck[77]. However, an effective value of the work of adhesion is possible and its value seems to remain reasonably consistent whatever the particle radius size. In the study conducted here, the system parameters such as the probe-surface material, surface roughness and the medium they were immersed in were replicated in each test. The interpretation we give to the small variance in the work of adhesion is due the variations in the surface roughness and contact quality of each system.

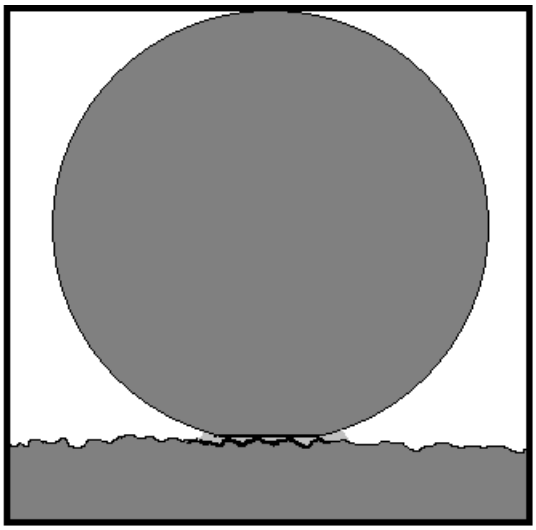

Figure 3.12: A probable contact between surface and probe.

Using the experimental values of the work of adhesion, equations 3.20 and 3.21 were used to find the approximate value of the initial stresses when the probe comes into contact with the surface. At room temperature, and assuming the probe distance to be approximately $D \sim 1$nm, the maximum value of the adhesion stress is ~ 1.4 GPa, 480 MPa and 360 MPa, for the 0.1, 3 and 7 μm probes respectively. The stresses given here are all above the tensile stress of ordinary iron at room temperature. It is likely therefore that some plastic deformation is taking place upon contact. This plastic deformation was certainly evident in the case of gold contacts at room temperature[60].

In the case of a particle in contact with a surface there has been a degree of uncertainty in relation to its overall distance of separation. If the atoms are in close enough contact they can bond. If the atoms are not bonding they remain in cohesion with the lattice and if only elastic contact takes place the particle will rest at some equilibrium distance as a balance between repulsive and attractive forces. An equation for the atomic binding energy was used to model the repulsive forces. This set the theoretical equilibrium separation at $D_0 = 7.77$ Å. Given ideal contact this sets the work of adhesion between the surfaces at $\gamma_w = 12.6\text{-}17$ mNm^{-1}. Experimental results tended to differ from this by a factor of no more than 3.

3.5. Conclusions

The measurement of van der Waal's forces between iron surfaces has received preliminary exploration in this chapter. Two distinct tip scales differing by an order of magnitude of 0.1 μm and 3 μm were studied having a, "ball and wall" geometry.

The relationship *F/R* with respect to separation showed that at the jump to contact distance *F/R* was smaller for the 3 μm tip than for the 0.1 μm tip which is consistent with previous work in gold.

The smaller tip radii measurements do suffer from more noise in the system, however these results produced a jump to contact distance more within expected values than the larger tip.

In comparison to experimental results for the Hamaker constant the Lifshitz theory and Coupled Plasmon Approach are shown to have a similar degree of accuracy. The two theories calculate results for this system that differ by only 10 %. The error margin for these results could potentially fall between 10 – 20 %. With this degree of precision, it can only be said at this stage that both theories compare equally well to the results. The departure from the theory in the most extreme case is only a factor of 0.3 – 0.4.

In the case of the 3 μm tip for example, yielded a measurement of the Hamaker constant at the lower end of the values expected for iron. Since the system was electrically grounded, the only other potential forces considered were magnetic. Iron is a ferromagnetic material and as such a magnetic remnant has potential to affect the result considerably. A theoretical calculation showed that in the case of a very weak ambient field, the magnetic force experienced by the system would be too negligible to perturb the results. Only in the extreme case that the tip became a single domain particle would there be a serious deviation from the force curve predicted by van der Waal's forces.

The atomic force microscope tips were shown to be too large to be single domain. It is concluded that magnetism did not significantly interfere with the result.

The oxidation of the surface is not likely to have a significant contribution to the force within the precision of this experiment. Oxidation layers would be too thin and their van der Waal's force field too weak to interfere with the van der Waal's forces emanating from the iron surface.

The Hamaker constant measured for the present study is $3.3\pm0.2 \times 10^{-19}$ J and $3\pm0.2 \times 10^{-19}$ J (for the 0.1 and 3 μm tip respectively). The 3μm tip shows the greatest stability of measurement and a clearer jump to contact distance with relatively small error bars compared to the 0.1μm tip. It is concluded from this study that the result for the 3 μm tip is the most reliable.

Experimental results for the work of adhesion were obtained with a 0.1, 3 and 7 μm tip, applying Schwarz theory of contact mechanics and observing the deformation length of the tip. The work of adhesion is shown here to be reasonably consistent despite the change in tip size when the adhesion energy is applied to the contact area derived from the deformation length. This is consistent with the theory. It is concluded that small corrugations in the surface can widen the effective distance between tip and surface. As surfaces are normally less than ideal, the work of adhesion values can be used as a reasonable guide when considering particle adhesion in real systems.

In a final word it can be said that the investigation of the interaction forces between ferrous materials is far from complete. The general study of van der Waal's forces in

metallic systems has not been explored extensively from an experimental point of view. Although in this case, the magnetisation of the iron tip samples was not a factor, it cannot be concluded that it is not an issue in iron powder reduction processes. Whist it is true that the average particle radii in a fluidised bed reactor is of the order 10-100 microns, there is likely to be nano-scale iron dust that each can potentially form single domain particles that have enough force to forge together on contact.

Chapter 4:

Measurements of the surface diffusion coefficient in iron and iron-carbon alloys using Focused Ion Beam milling and High Temperature Laser Scanning Confocal Microscopy

Chapter 4: Measurements of the surface diffusion coefficient in iron and iron-carbon alloys using Focused Ion Beam milling and High Temperature Laser Scanning Confocal Microscopy

4. Introduction

The field of research into surface self diffusion via mass-transfer techniques has been opened up as a live area of research, especially quantitatively, since the late 1950s and early 1960s[100-103]. Writers such as Mullins, King and Herring, paved the way theoretically and provided mathematical formalism that allowed surface changes to be quantified, in terms of surface diffusion coefficients.

In metallic systems, it is possible to derive numbers, such as surface diffusion coefficients, by way of observing the changes of micron-scale geometry on the surface, using these mass transfer techniques[104-107]. These techniques principally study the changes in some surface feature such as grain boundary groove development, or the attenuation decay of a surface scratch, grain boundary groove or multiple scratch wave pattern on the surface, taking time lapse pictures using some form of interference microscopy.

The experimental techniques in the past relied upon heating of the material to temperature, holding for a certain time, then cooling and removing the sample in order to view it under an interference-microscope. This process is then repeated for as many time stages as necessary[104]. These techniques are, in principal, particularly prone to oxidation and annealing effects that may influence the result.

In this chapter, a new experimental technique using high-temperature confocal microscopy (HLSCM) and focused ion beam (FIB) milling is presented. Some measurements are made with the assistance of and atomic force microscope. This new technique minimises handling of the material, and is capable of making a continuous, in-situ observation of a particular surface profile development. The technique here is applied to various carbon steels.

4.1. Theoretical considerations

4.1.1. Driving force for diffusion

The rate of material transport is dependent upon temperature. When the raising of temperature activates material transport, there is an associated change in surface topography. The driving force of this transport is the thermodynamic condition of a local gradient in chemical potential, driving it to equilibrium.[108, 109] The chemical potential gradient is proportional to the difference in surface curvature for a surface cavity or undulation. The surface curvature is $K = 1/r$ where r is the radius of curvature of the cavity or undulation. This is related by the Gibson-Thompson formula[109], given by

$$\Delta\mu = \mu - \mu_0 = K\gamma_s\Omega \qquad \text{(J)} \qquad (4.1)$$

where, μ and μ_0 are the chemical potentials of a surface of curvature K and a flat surface respectively. Ω is the atomic volume in the solid state, and γ_s is the surface energy of the crystal.

The effect of this curvature can be expressed as a diffusion current density relation, called the Einstein-Nernst relation[110], given by

$$J = -\frac{D_s \nu}{kT}\frac{\partial \mu}{\partial s} = -\frac{D_s \gamma \Omega \nu}{kT}\frac{\partial K}{\partial s} \qquad (\mathrm{m^{-1}s^{-1}}) \qquad (4.2)$$

where ν is the atomic surface density, D_s is the surface diffusion coefficient, k is Boltzmann's constant, T is the absolute temperature and s is the arc length along the curvature. The negative sign here indicates that the surface is concave into the surface.

Regions on a surface with positive curvature (convex bulges on a surface for instance) will have a higher chemical potential than flat or concave regions. Matter is then, driven by this gradient, transported from surface peaks to surface troughs.

4.1.2. Mechanisms of matter transport and associated geometrical scale factors

The present study relies on the application of the theory of mass transfer, originally introduced by Mullins[100-102], and later reinterpreted and extended by Tritscher and Broadbridge[111].

In any solid-state material, the amplitude of a surface undulation will decay exponentially with respect to time, according to one or more mechanisms of material transport. This can be represented by Mullins' [102] formula

$$a(t) = a_0 \exp\left\{-\left(F\omega + A\omega^2 + C\omega^3 + B\omega^4\right)t\right\} \qquad (\mathrm{m}) \qquad (4.3)$$

where $a(t)$ is the amplitude of the surface undulation, a_0 is the amplitude at time $t = 0$, $\omega = 2\pi/\lambda$ is the wave number and λ is the wavelength. The coefficients of the wave number (*F, A, C, B*) correspond to different mechanisms of transport. *F, A, C, B* indicate mechanisms of viscous flow, evaporation-condensation, volume diffusion and surface diffusion respectively. As stated, these mechanisms can occur on their own or in conjunction with two or more others. The question then is how to isolate any particular mechanism.

In order to isolate a particular mechanism, some criterion is needed to deduce it for a system with well-defined parameters. In crystalline systems, viscous flow is generally considered to be either non-existent or negligible in its contribution to matter transport[102]. In the case of iron, the vapour pressure is so low (~37 Pa, $298 < T < T_m$) that evaporation is unlikely to proceed [102, 104]. In addition, if evaporation-condensation was a predominant mechanism, the groove formed on the surface at the grain boundaries during thermal grooving would be flat on the edges as in **figure 4.1a**. If volume or surface diffusion is the dominant mechanism, a pronounced ridge will form on either side of the groove, as in **figure 4.1** [101]. In our experiments, these ridges were observed during thermal grooving and decay, shown in **figure 4.1b and c** compared to **figure 4.1a**.

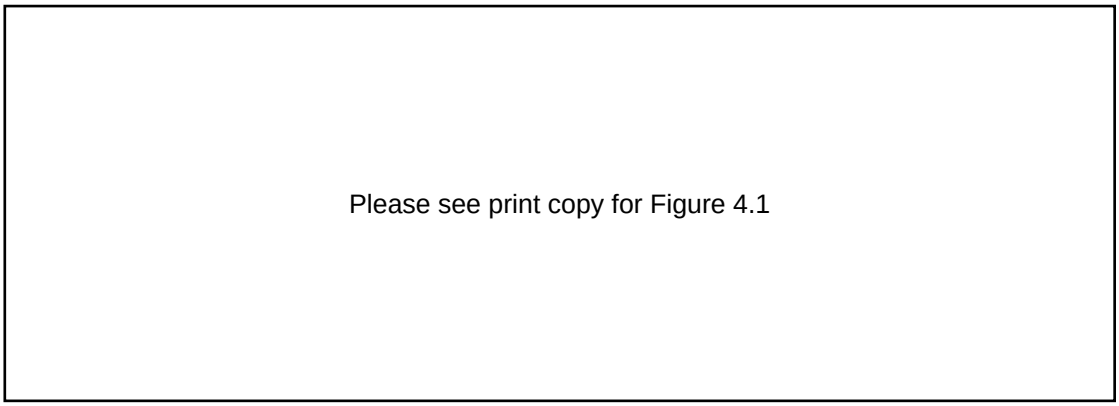

Figure 4.1: (a) An example of an expected groove profile, where evaporation-condensation is dominant. **(b)** An example of an expected groove profile, where volume or surface diffusion is dominant. **(c)** A sample of the profiles obtained in the present study.

The above consideration eliminates the likelihood that viscous flow and evaporation condensation play a role in surface annealing, leaving only volume and surface diffusion as possible mechanisms. Comparing the two exponential coefficients for volume and surface diffusion it needs to be established at what surface wavelength does surface diffusion begin to dominate, viz:

$$C\omega^3 \le B\omega^4 \Rightarrow C \le B\omega = B\,2\pi/\lambda \Rightarrow \lambda \le 2\pi\frac{B}{C} \le 2\pi\left(\frac{D_s\gamma\Omega^2\nu}{kT} \div \frac{D_v\gamma\Omega}{kT}\right)$$
$$\Rightarrow \lambda \le 2\pi\Omega\nu\frac{D_s}{D_v} \qquad (4.4)$$

where ν is the surface atomic density, Ω is the atomic volume density and $\nu = \Omega^{-2/3}$,

$$\therefore \lambda \le 2\pi\Omega^{1/3}\frac{D_s}{D_v} \quad \text{(m)} \qquad (4.5).$$

Surface diffusion will be dominant where $\frac{D_v}{D_s} << 1$, and since the atomic volume is a known value, the wave length of the surface groove must be created such that

$\frac{2\pi\Omega^{1/3}}{\lambda} << 1$. Blakely, Mykura and others, [103, 104, 112] through past experimentation, assert that a wavelength $\lambda < 20\mu m$ is necessary to ensure that surface diffusion is dominant. In the case of iron and carbon steel, where $10 < \lambda \leq 20\,\mu m$, $\frac{2\pi\Omega^{1/3}}{\lambda} \approx 10^{-5}$. The theory outlined here also assumes that the groove is shallow, where the ratio of the depth of the groove to its width is approximately ~0.1-0.16[101].

4.2. Experimental techniques designed to measure the surface diffusion coefficient

Two approaches were used in this study, both coming under the heading of mass-transfer techniques. These are, single groove or scratch decay (SSD) and multiple-groove/scratch decay (MSD) [110]. The mass-transfer method measures surface diffusion by observing changes in surface topography and is based on a general theory by Mullins [101, 102].

4.2.1. Multiple scratch decay (MSD)

The approach of multiple scratch decay, is based on observing the attenuation in amplitude of an induced, approximately wavy surface topography toward a flat surface over time. The attenuation in amplitude and width broadening over time can be described by the equation:

$$y(x,0) = a_0 \sin(\omega x) \quad \text{(m)} \qquad (4.6).$$

This is the general form of the surface profile at $t = 0$, and an initial amplitude a and ω as the wave-number. Blakely and Mykura showed [112] that the profile need not exactly conform to the profile of equation 4.6. It can however be resolved into its Fourier components. If volume diffusion can be eliminated, the differential equation describing the changes in the surface with time is:

$$\frac{\partial y(x,t)}{\partial t} = -B\omega^4 y(x,t) \qquad (\mathrm{ms}^{-1}) \qquad (4.7).$$

This equation has the solution:

$$y(x,t) = y(x,0)\exp(-B\omega^4 t) \Rightarrow y(x,t) = a_0 \sin(\omega x)\exp(-B\omega^4 t) \qquad (\mathrm{m}) \qquad (4.8).$$

It can be shown that the amplitude a will vary with time according to:

$$a = a_0 \exp(-B\omega^4 t) \Rightarrow \ln\left(\frac{a_0}{a}\right) = B\left(\frac{2\pi}{\lambda}\right)^4 t \quad (\mathrm{m}) \qquad (4.9).$$

Since the initial and changing amplitudes are expressed as a log-ratio, their height units are arbitrary and thus the observations of the progress of decay do not require an absolute measurement of the height.

4.2.2. Single scratch (groove) decay (SSD)

The equation for the single groove profile *y(x,t)* with initial profile *y(x,0)* as mentioned can be obtained by resolving it into its Fourier components, which has been done by King and Mullins [103].

The initial profile under Fourier transformation is:

$$g(\omega,0) = \frac{1}{2\pi}\int_{-\infty}^{\infty} y(\varepsilon,0)\exp(-i\omega\varepsilon)d\varepsilon \qquad (4.10).$$

In time, the initial profile will decay according to:

$$g(\omega,t) = g(\omega,0)\exp(-B\omega^4 t) \qquad (4.11)$$

where t is called the "fictitious" time[103], understood to mean the time from the initial creation of the profile which cannot be realistically measured in terms of real experimental running time. Thus, a new time variable is introduced, $t' = t + t_0$, where t_0 is the time elapsed since the creation of the initial profile, and t is the experimental running time starting at $t = 0$ for some arbitrary point in the experiment. The value t_0 can be determined from experimental data by a technique outlined below.

Since the real profile is given by:

$$y(x,t') = \frac{1}{2\pi}\int_{-\infty}^{\infty} \exp(i\omega x)\exp(-B\omega^4 t')g(\omega,0)d\omega \qquad (4.12).$$

The initial profile can be evaluated as a Taylor series in ω, and the overall profile can be shown to be[103]:

$$y(x,t') = -\frac{\alpha}{2\pi(Bt')^{3/4}}\frac{1}{8\pi}\sum_{n=0}^{\infty}\frac{(-1)^n}{(2n)!}\Gamma\left(\frac{2n+3}{4}\right)\left[\left(\frac{x}{(Bt')^{1/4}}\right)\right]^{2n} \text{ (m)} \qquad (4.13)$$

where $\alpha = \langle x^2 \rangle$ is the invariant second moment of the profile[7].

The second moment here is given by, $\alpha = \int x^2 y(x,0)dx$. This term contains the initial arbitrary profile. Thus the variation in width of any groove profile (see **figure 4.2b**) with respect to time, driven by surface diffusion, can be shown to be:

$$w = 6.9(Bt')^{1/4} \qquad \text{(m)} \qquad (4.14)$$

where, as earlier assigned :

$$B = \frac{D_s \gamma \Omega^2 \nu}{kT} = \frac{D_s \gamma \Omega^{4/3}}{kT} \qquad (\text{m}^2\text{s}^{-1}) \qquad (4.15).$$

The time taken to create the initial profile t_0 can be evaluated for any set of experimental data. This can be done by evaluating the ratio of a data point n, to the data point $n + 1$, as follows:

$$\frac{w_n}{w_{n+1}} = \frac{6.9(Bt_n')^{1/4}}{6.9(Bt_{n+1}')^{1/4}} = \frac{t_n'^{1/4}}{t_{n+1}'^{1/4}} = \frac{(t_n + t_0)^{1/4}}{(t_{n+1} + t_0)^{1/4}}$$

solving for t_0:

$$t_0 = \frac{\left[\left(\frac{w_n}{w_{n+1}}\right)^4 t_{n+1} - t_n\right]}{\left[1 - \left(\frac{w_n}{w_{n+1}}\right)^4\right]} \qquad \text{(s)} \qquad (4.16).$$

Obeying the criteria above and equations (4.9), (4.14), (4.15) and (4.16), it is possible to evaluate the surface diffusion coefficients of any metallic material.

[7] It is the author's interpretation, that this term defines the degree of curve attenuation from the initial profile.

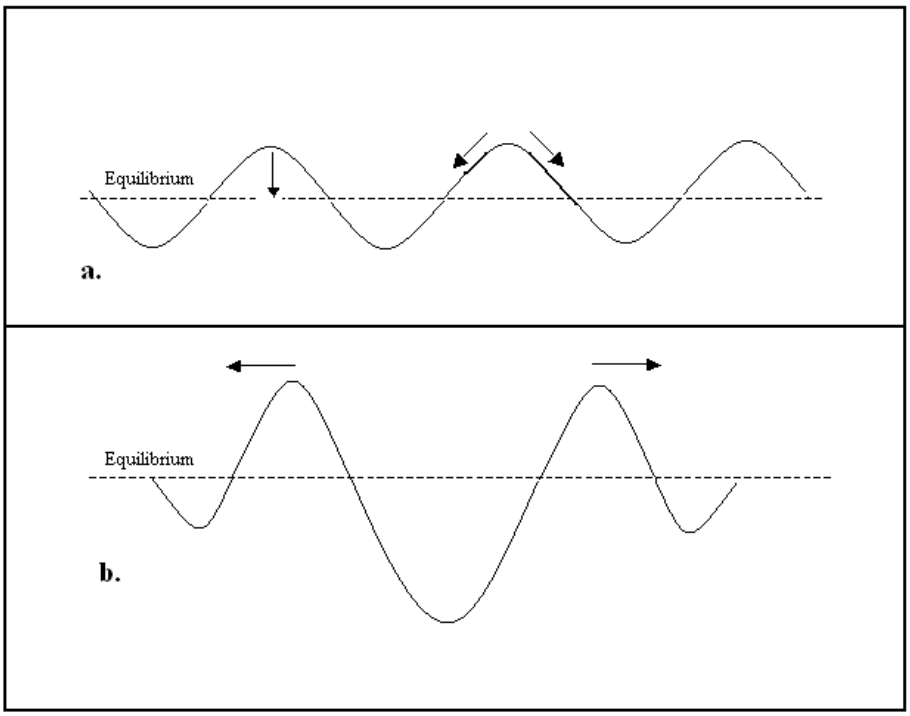

Figure 4.2a-b: A schematic representation of the cross-section of the decay of a groove or sin-wave pattern on a surface. a) A sine wave pattern. b) A single groove pattern.

4.3. Apparatus and experimental procedure

4.3.1. High Temperature Laser Scanning Con focal Microscope

In our experiment changes of the surface topography were made *in-situ* and in real time by a (Lasertech™) high temperature laser scanning confocal microscope (HLSCM) (shown in **figure 4.3a**). High resolution and quantitative topographical surface measurements, can be made in the confocal microscope, at the temperature of interest[113, 114].

A 1.5 mW He-Ne laser with a 632.8nm wavelength beam is the principal device to scan the samples. The 0.5μm diameter beam is reflected and scanned by an acoustic optic detector in the horizontal direction at a rate of 15.73 kHz and by a galvano mirror in the

vertical direction at 60 Hz. The scanning beam is confocally focused (i.e. using a confocal pinhole) on the surface of a specimen via a polarising plate and an objective lens, passing through a quartz covered view port. The reflected beam returns via the same path, passing through a beam splitter to a lens, which is then focused onto a CCD image sensor through a pinhole with an optical resolution of 0.25 μm with magnifications of up to 1350x being possible. This is an improvement over ordinary light microscopy which is usually at a resolution of 1μm [115]. The laser beam is reflected from the specimen through the objective lens and the beam splitter, so that only beams from the focal plane of the objective lens are focused on the CCD image sensor. Other beams reach the detector unfocused.[116]

As a surface feature is focused upon, the image intensity grows to a maximum, and this is used to measure the surface profile along a specified scan line, as was seen in **figure 4.1c** (the scan line is enhanced for presentation). The specimen is also scanned in the vertical direction, and the intensity maximum of the reflected beam is directly proportional to the height, and, if correctly calibrated can give a reliable reading of the height.

Specimens, held on a platinum pan inside an alumina crucible 4.5-10mm in diameter, are placed at one focal point of a gold plated elliptical cavity. A 1.5kW halogen lamp is placed at the other focal point in the cavity causing the radiation to converge on the specimen and thus heating it. The temperature of the specimen is monitored by thermocouples and is displayed on a monitor screen alongside the image. The laser beam scans at different focal depths, storing the corresponding data to reproduce the

image of the surface resolving surface features of 0.1 – 327 μm in diameter. A schematic diagram of the furnace and specimen holder is shown in **figure 4.3**.

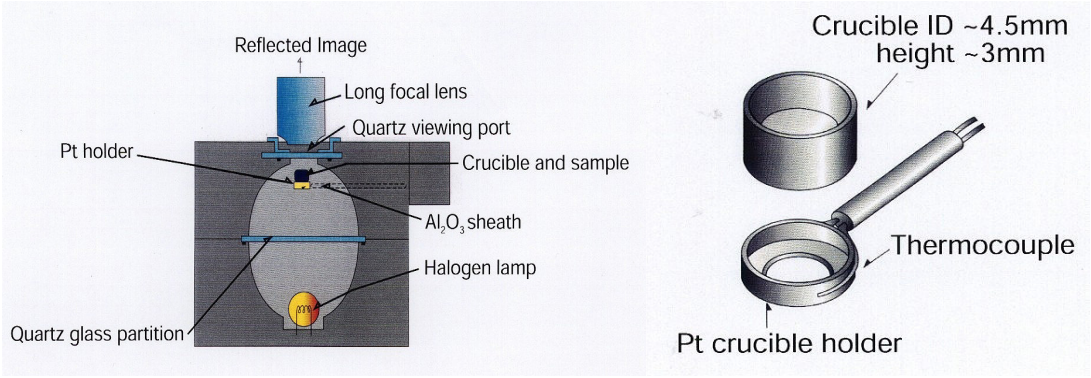

Figure 4.3: Schematic diagram of the HLSCM furnace and sample holder.

The gold cavity is isolated from the outside and evacuated down to ~10^{-5} Pa and then flushed with argon gas containing less than 1 ppb O_2, CO and CO_2 at a flow rate of 1.7 × 10^{-6} m^3 s^{-1} to prevent oxidation. This process is repeated four or more times to be sure that as much oxygen as possible is removed.

When the chamber is sufficiently pumped down and flooded with argon, the samples were first heated to 150 °C and held for 20 minutes in order to remove as much oxide and surface impurities as possible. The samples were then heated to the desired temperature for measurements.

The images are read by a computer and are recorded on a DVD disk in real time. The images can then be played back, frame by frame, for careful analysis of the images.

4.3.2. Sample preparation and treatment

The surface diffusion coefficient of iron and four iron-based alloys were determined. The compositions of the specimens used are in **table 4.1a-b**. Specimens were cut into discs 1 mm thick and 10 mm in diameter, mechanically polished to a mirror finish, thereby reducing the surface roughness to <0.1μm. The specimens used to measure the surface diffusion coefficient in pure iron were not milled in the focused ion beam mill. The surface wave patterns were etched using a 1200 grit sandpaper and then electrochemically polished. The single grooves were obtained through thermal grooving. As this was the technique used in past experiments it enabled a fairer comparison of the confocal technique to older techniques. Zapuskalov[117, 118] was the first to use confocal microscopy to determine the surface diffusion coefficient in pure iron. He measured the decay of thermal grooves on the surface to determine the rate of surface diffusion. Measurements in pure iron performed in the present study were done using thermal groove decay and mechanically etched surface. This enabled us to benchmark the validity of the confocal technique against Zapuskalov's measurements and those on pure iron in earlier studies[110]. More advanced techniques have been developed in the present study which can induce grooves on the surface in a controlled fashion. The focused ion beam mill was used to prepare two types of surface. In one type of sample a single groove pattern was made, in the other a sinusoidal wave pattern, as shown in **figure 4.3a** and **b**). These images were obtained using atomic force microscopy imaging to show the precision with which the ion beam mill can mould the surface patterns to fit the equations as close as possible. When the ion beam mill etches a surface it uses positive gallium ions to impress marks into the surface without removing surface material at least in principle. This satisfies the theoretical criteria that no surface material should be removed to make the grooves.

The theory developed to measure surface diffusion assumes that the surface undulations are molded into the surface and that the displaced material can flow back from a position of high energy to a position of minimum energy[101, 103, 112]. If material is removed, the surface needs to rely on volume diffusion in order to transport enough material to fill the groove, rather than redistributing locally displaced matter.

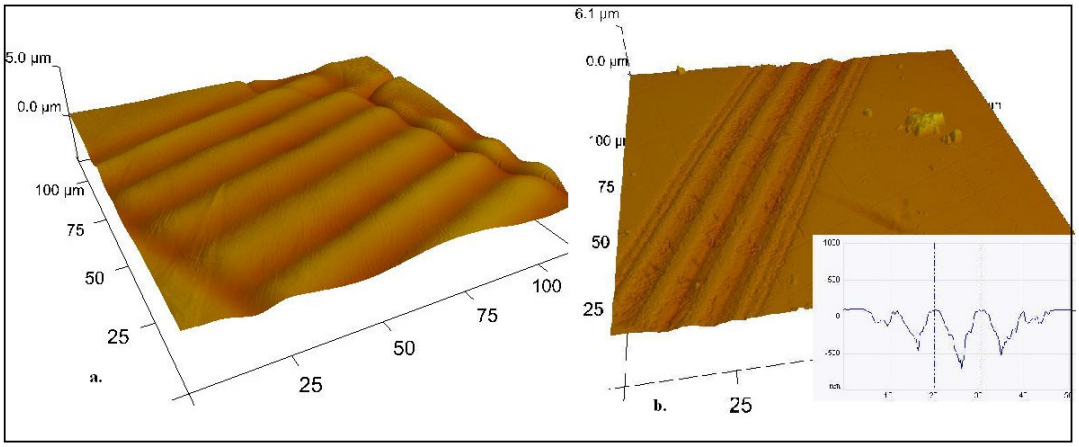

Figure 4.4a-b: An AFM image of the patterns created in the ion beam mill. **a)** A sine-wave pattern. **b)** A groove pattern modelled off a grain boundary groove. The insert on the right here shows a traced section of the groove.

In this study different measurement techniques were used to determine the surface diffusion coefficients. The groove decay technique was used in an Fe-1.5%C alloy, while the sinusoidal pattern was used in the determination of the surface diffusion coefficient of the Fe0.9%C steel. The advantage of using a sinusoidal-wave pattern is that the equation it uses is linear and thus requires fewer data points to record a diffusion measurement. In this case, an AFM image can be taken at the beginning and end of an experiment for a quick and easy result. The disadvantage is that the sample takes more time to prepare.

The advantage of using the single groove pattern is that the pattern takes less time and the AFM is not necessary to take reliable height measurements. The disadvantage is that errors can creep into the data when determining the initial time by equation 4.16.

Table 4.1a: The composition of pure iron used.

C (wt%)	Mn ppm	P ppm	Al ppm	Ni ppm	Si ppm	Na ppm	Ta ppm	Cu ppm	Co ppm	Cr ppm	Ga ppm	Ge ppm
<0.0036	1.1	1.4	3.9	6.1	14	0.5	10	1.6	10	4.7	0.7	1.7

Table 4.1b: The composition of alloys used.

C wt%	Mn wt%	Cr wt%	W wt%	V wt%
0.9	1.2	0.5	0.5	0.1
0.17				
0.43				
1.49				

4.3.3. The evolution of this technique and a critique of different technical approaches

Researchers in the Wollongong Steel research labs developed the original conception and technique for using the confocal microscope to gather surface diffusion coefficients[117, 118].

The difficulty in making surface diffusion measurements has always been in creating a well-defined surface geometry to observe. Naturally occurring thermal grooves such as the one depicted in **figure 4.1c** are ideal geometries to observe decay. However, finding an example such as this one occurring naturally by thermal grooving is not always reliable. The problem in using multiple scratches is that the scratches appear rough and irregular and it is possible that errors will be produced in the diffusion rates measured as the geometries take time to settle and smooth at high temperature.

In the first stage of developing this technique of measuring surface diffusion, thermal grooves were used which, when a suitable groove is identified, will make a clear transition to decay as resolved by the confocal optics. The confocal optics is reliable and accurate in measuring widths in the horizontal plane. However absolute depth measurements are not shown to be reliable. It is possible to work around this limitation, as the decay in depth signal by the scope trace is proportional to the depth of the wave as it decays. Fortunately equation 4.9 models the relative change in wave height with respect to time.

Recent developments have led to using focused ion milling, making it possible to cut grooves of a variety of shapes, with great precision into the surface of a specimen shown in **figure 4.4**. In the results using the sinusoidal patterns the AFM was used to measure depth at different time intervals. Whilst a highly accurate measure of the depth and width could be obtained the advantages of real time *in situ* observation in the confocal microscope were lost, and the specimen experiences more chance of contamination.

An approach was eventually found that could optimise measuring surface diffusion using confocal microscopy in terms of reliable measurements, ease of use, in situ observation, minimisation of time and preventing exposure of the sample to the atmosphere.

It is possible to create a "virtual" thermal groove in the focused ion beam mill such as shown in **figure 4.4b**. These artificial grooves will obey the equations well provided

some care is taken in etching particular details. For instance, if a groove is etched such as the one shown in the schematic in **figure 4.1a**, the groove will not decay according to the theory. In fact it appears as if the groove width narrows with time and this is due to surface diffusion filling in the groove. If the groove width is to broaden with time as many grooves as possible must be etched on either side of the central groove as shown in **figure 4.1a**. As the grooves go further out they also must decrease in depth. This provides the correct curvature difference to drive the groove outwards. A groove such as this is harder to produce that the plane sin wave pattern however it lends itself to measuring groove pattern decay with high precision and reliability without removing the sample from the confocal microscope.

4.4. Results

The diffusion coefficients gathered for iron in the δ and γ phases and the corresponding alloy compositions are presented in **table 4.2**. Surface diffusion coefficients in pure iron in the gamma phase have been measured previously and reported in the literature[104, 110]. In order to validate the confocal microscope technique for making surface diffusion measurements, measurements in the gamma iron phase have been repeated.

Table 4.2: Surface diffusion coefficients of iron at various temperatures and alloy compositions.

Temperature °C	D_s (m^2s^{-1})
γ-Fe	
1100	$1.21x10^{-8}$
1220	$5.58x10^{-8}$
1300	$9.98x10^{-8}$
δ-Fe	
1410	$3.89x10^{-7}$

1440	5.22×10^{-7}
1470	8.71×10^{-7}
γ-Fe-0.43C	
1100	1.38×10^{-8}
γ-Fe-0.9C	
1000	5.20×10^{-11}
1100	4.20×10^{-10}
1150	1.20×10^{-9}
1200	2.30×10^{-9}
1250	7.00×10^{-9}
γ-Fe-1.5C	
1100	7.92×10^{-10}
γ+Liquid-Fe-1.5C	
1300	5.42×10^{-6}

4.4.1.Surface diffusion measurements in pure iron

Measurements were made of changing surface topography with time in order to obtain surface diffusion coefficients for particular temperatures. Once a number of coefficients are obtained at these temperatures, an equation for the surface diffusion coefficient with respect to temperature can be formulated. This equation is generally of the form:

$$D_s(T) = D_0 \exp\left\{-\frac{Q}{k_B T}\right\} \qquad (\mathrm{m^2 s^{-1}}). \tag{4.17}$$

Where D_0 is the diffusion pre-factor and Q is the energy required to activate diffusion[110].

Surface diffusion coefficients were measured in γ and δ-Iron phases. The γ-Iron measurements were done in order to make a comparison with pre-existing data. The δ-Iron measurements are the first reported, so far as the authors are aware. Surface diffusion results for γ-iron along with data from other studies are shown in **table 4.3**.

Table 4.3: Results of diffusion in gamma and delta iron.

Please see print copy for Table 4.3

4.4.2. Gamma Iron

Measurements of surface topography were made in γ-Iron by observing the decay of a grain boundary groove, after it had migrated. When the temperature of iron is increased beyond 912°C, austenite grain boundaries are formed on the surface. The advantage of using grooves created by prior grain boundaries, is that this profile conforms closely to that described by King and Mullins[103]. The migration of the grain boundary from a groove created by that grain boundary can be forced experimentally by inducing a step temperature fluctuation of about 50 °C and then returning to the measuring temperature. This effectively leaves behind a single surface scratch that is ideal for observation. A sample of an image of grain boundary groove decay at 1300°C, is shown in **figure 4.5a**.

Measurements of the groove width (w) with respect to time (t') were taken at temperatures of 1100°C, 1220°C and 1300°C. These are plotted in **figure 4.6a-c**. The coefficient of the time in the equation $w = 6.9(B^{1/4})t'^{1/4}$ can be used to obtain the B coefficient and thus the surface diffusion coefficient. The surface diffusion coefficients obtained from these experimental measurements are shown in **figure 4.6d**.

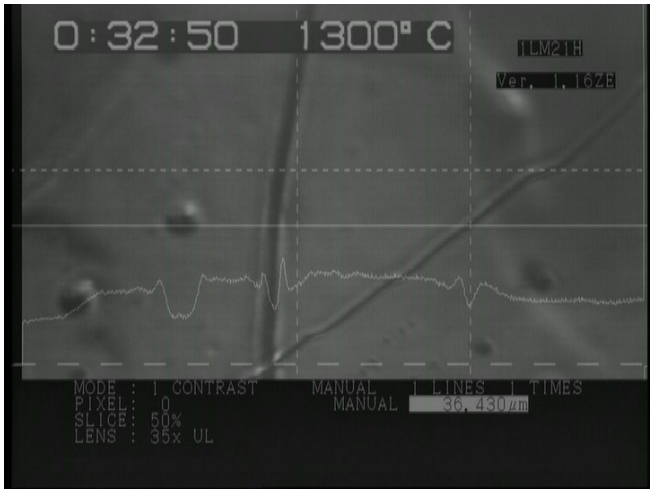

(a)

(b)

Figure 4.5a-b: (a) A sample of an image used to measure surface diffusion in γ & δ-iron, γ - iron, T = 1300 °C. Here the scope trace measures a section of the topography of two grain boundary grooves. **(b)** This is an image of a sinusoidal pattern made by mechanically etching the surface δ - iron, T = 1440 °C.

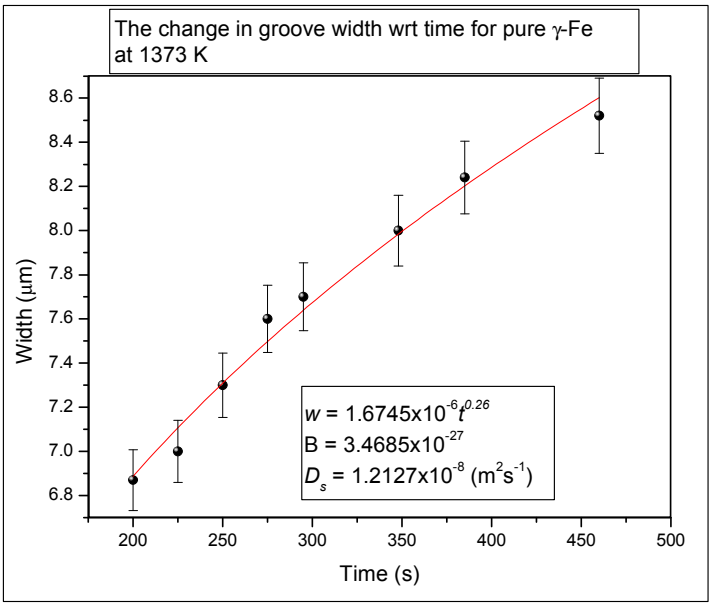
The change in groove width wrt time for pure γ-Fe at 1373 K
Width (μm)
Time (s)
w = 1.6745x10^-6 t^0.26
B = 3.4685x10^-27
D_s = 1.2127x10^-8 (m^2s^-1)

a)

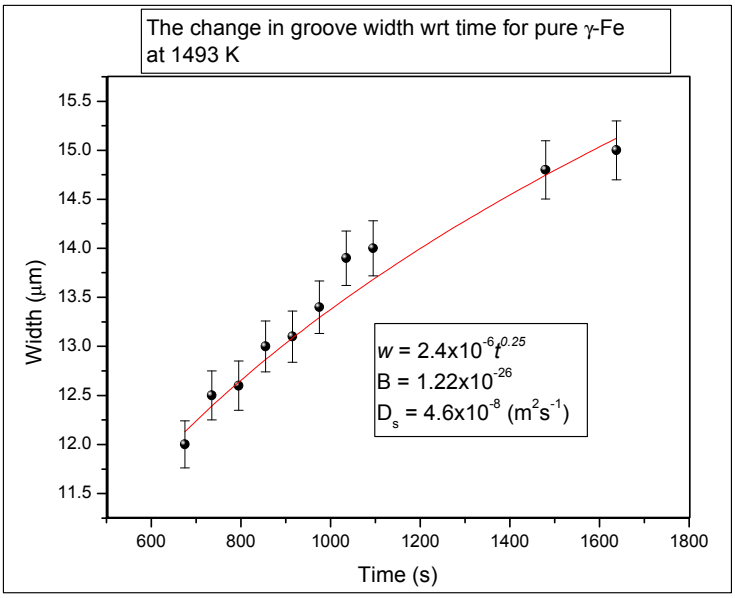
The change in groove width wrt time for pure γ-Fe at 1493 K
Width (μm)
Time (s)
w = 2.4x10^-6 t^0.25
B = 1.22x10^-26
D_s = 4.6x10^-8 (m^2s^-1)

b)

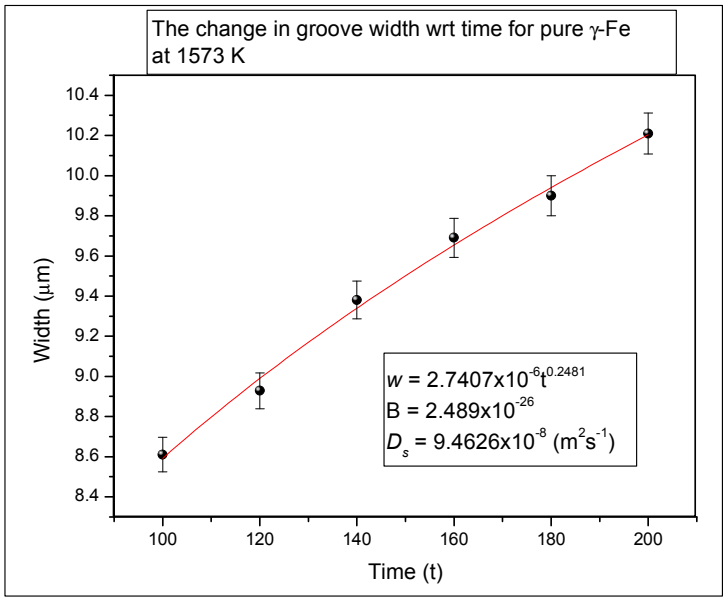

c)

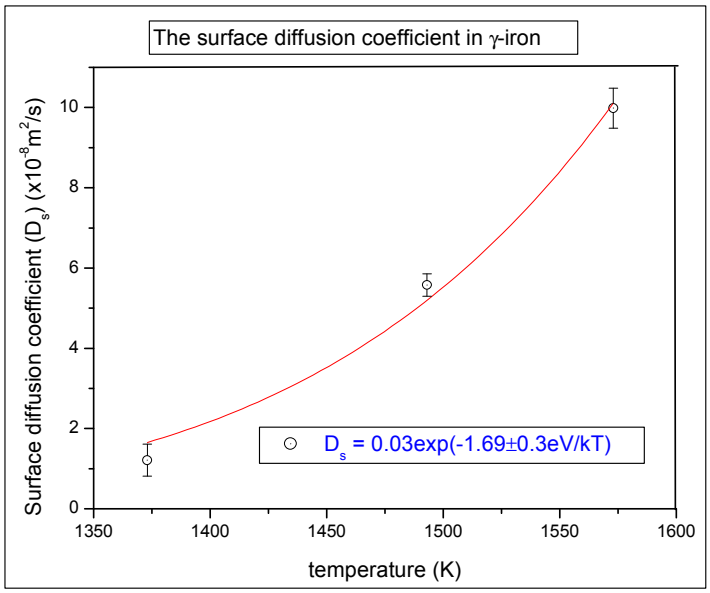

d)

Figure 4.6 a-d: The set of data relating width broadening to time. The time axis here has been adjusted for the time taken to build the profile t_0. The curves here display a w ~ $t'^{1/4}$ relationship. **(a)** T = 1100 °C **(b)** T = 1220 °C **(c)** T = 1300 °C **(d)** Surface diffusion coefficient of γ-iron verses Temperature.

Using equation 4.14 and 4.17, the final equation for the surface diffusion coefficient in γ

- Iron, for this sample of data is then

$$D_s(T) = 0.03 \exp\left\{-\frac{1.69 \pm 0.3eV}{k_B T}\right\} \quad (m^2 s^{-1}) \quad (4.18).$$

4.4.3. Delta Iron

Observing the decay in amplitude of multiple scratches on the surface enabled us to make measurements of the diffusion coefficient in delta iron. A sample image of multiple scratch decay at 1440 °C, is shown in **figure 4.5b**. Utilising equation 4.9,

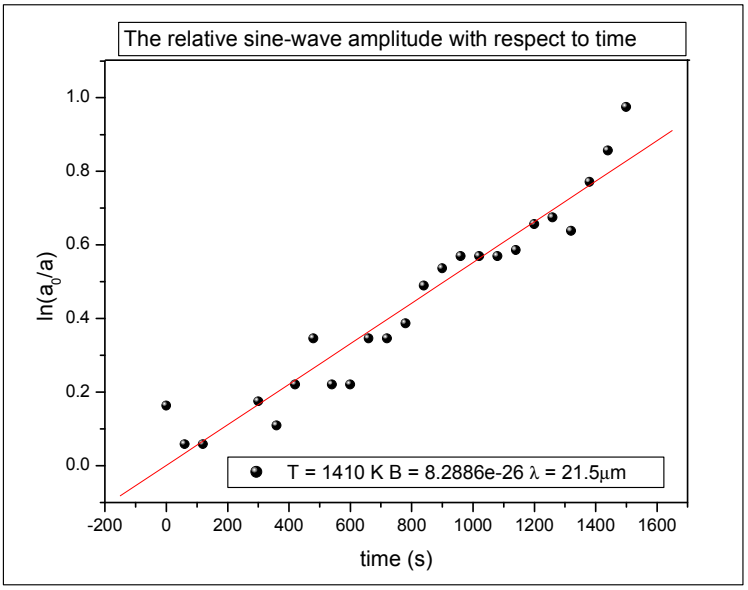

a)

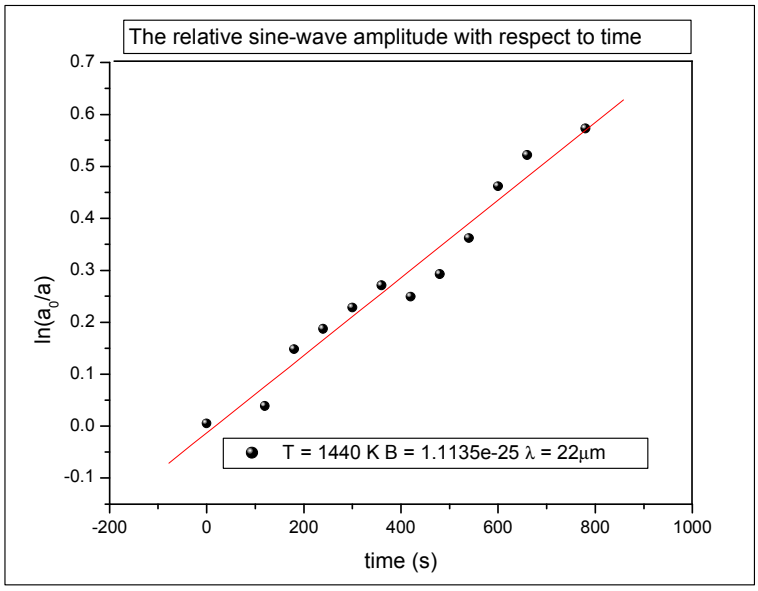
The relative sine-wave amplitude with respect to time
ln(a0/a)
time (s)
T = 1440 K B = 1.1135e-25 λ = 22μm

b)

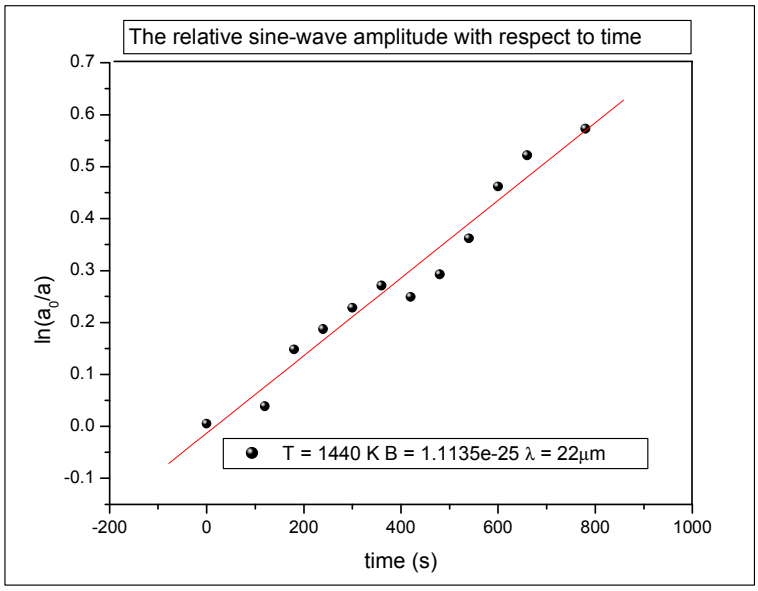
The relative sine-wave amplitude with respect to time
ln(a0/a)
time (s)
T = 1440 K B = 1.1135e-25 λ = 22μm

c)

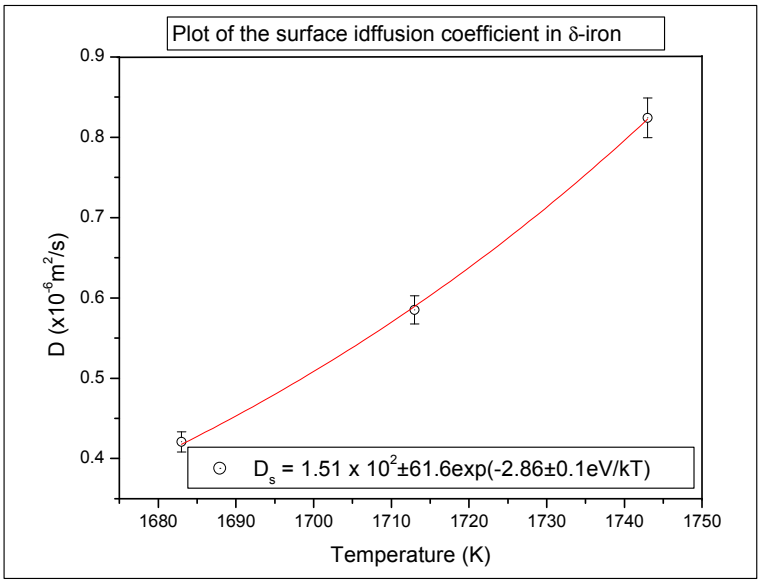

d)

Figure 4.7 a-d: The set of data relating amplitude attenuation with respect to time. **(a)** T = 1410 °C **(b)** T = 1440 °C **(c)** T = 1470 °C **(d)** The plot of the surface diffusion coefficient versus temperature for delta-iron.

the drop in intensity of the returned laser signal from the surface becomes directly proportional to the natural log of the initial amplitude relative to the amplitude changing in time. Plotted against time (**see figure 4.7a-c**), this yields a straight line from which the *B* coefficient can be extracted from equation 4.9 and hence the diffusion coefficient,

$$D_s(T) = 1.51\times10^{2}\ \exp\left\{-\frac{2.86\pm0.1eV}{k_B T}\right\} \qquad (\mathrm{m^2 s^{-1}}) \qquad (4.19).$$

4.4.4. Discussion of the diffusion coefficients determined for iron

In general, the experimentally determined values of groove decay conform reasonably well to the predictions made by equations (4.9) and (4.14). The results in gamma iron obey the $w \sim t^{1/4}$ relationship to within an error of 2 - 5 % (**figure 4.6a-c**). The

experimental measurements of groove decay in delta iron are plotted in **figure 4.7a-b** and they conform to the theoretical linear relationship to within 2-3 %. The better agreement of the experimental measurements with theoretical predictions at higher temperatures may be attributable to the higher degree of smoothing out of the groove profile. The material in this case has had time to anneal, thus reducing the probability of dislocations and removing of impurities away from the surface.

Due to the high-resolution laser optics, and the real time *in-situ* nature of the measurements, the time frame required in observing decay is considerably shorter than previous methods of acquiring surface diffusion coefficients. This fact is an advantage when it comes to assigning a value to λ in equation 4.9 for the sinusoidal wave. In the case of multiple scratch decay, the wave-length on the iron surface will broaden, given long periods of time [104]. However, on the time scale of our experiments, the wave-length broadens by much less than a micron. This means that an average constant value seems sufficient for making practical calculations.

4.4.5. Comparison with previous data

An important question that arises from a study of groove decay, is just how reproducible the results are. It has been argued in a previous review of surface diffusion measurements, that it is difficult to reproduce experimental measurements[110]. This is due to the fact that the mechanism of atom migrations is not governed by a single mechanism and is particularly sensitive to surface impurities.

One of the aims of using confocal microscopy to measure groove decay at temperature is to reduce some of these uncertainties. The main sets of data in measuring surface

diffusion for gamma iron have come from Blakely and Mykura[104]. They used mass transfer techniques in their work. The difference being that in their experiments it was necessary to remove the sample at each time step, for each temperature and to measure the profile by using an interferrogram. This technique is not only time consuming, but it allows for too significant exposure to the atmosphere during transport, hence increasing the potential for surface contamination.

High temperature confocal microscopy measurements on the other hand are made *in-situ* and in real-time and hence, the sample is not exposed to the atmosphere at any stage during the measurement of groove decay. The method is also less time consuming and thus leaving less time for oxidation.

A comparison between our measurements with previously measured results are shown in **table 4.3**. Values for surface diffusion were calculated from measurements at 1373, 1493 and 1573 K. An average was taken and a standard deviation calculated. These results are tabulated in **table 4.4**.

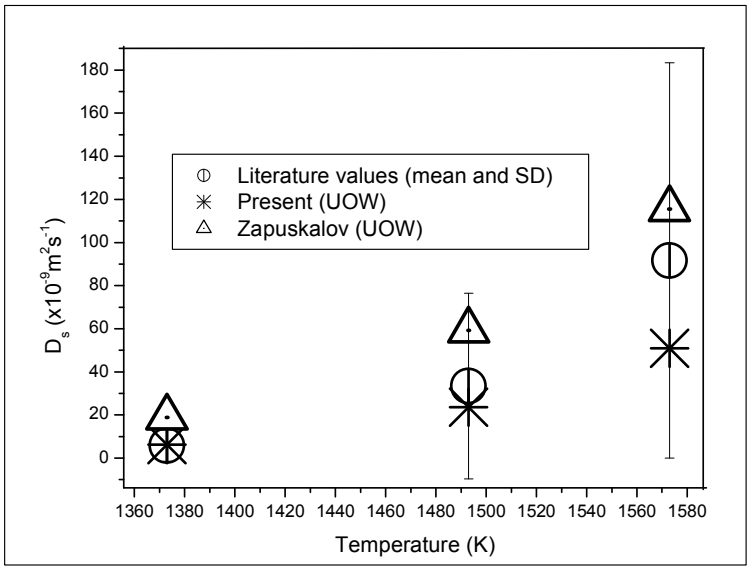

Figure 4.8: The above graph shows the mean and standard deviation of surface diffusion values found in the literature for pure iron for three key temperatures. Compared to these values are the values acquired at Wollongong university for the same temperatures.

Table 4.4: Calculated surface diffusion coefficients from the literature and from the present study. The second and third columns respectively show the average and standard deviation of the values in the literature[110].

Please see print copy for Table 4.4

The results shown in **figure 4.8** and **table 4.4** reveal that the surface diffusion coefficients obtained in the present study are is reasonably good agreement with previously reported values, being within one standard deviation of the mean value obtained from the literature. Results taken in our own laboratory by the same technique by Zapuskalov deviate from our own results by a small amount. The difference is mainly governed by the movements of surface atoms, clusters and planes of atoms that can be "pinned" by impurities and oxides.[110] Contamination and oxidation is a

[8] Values by Nikolai Zapuskalov at Wollongong university 2000.
[9] Values by Daniel Blundell at Wollongong university 2002.

constant variable that can only be minimised and not eliminated by this technique. The difference in these results is only about a factor of two overall which is a good reproducibility for these types of experiments. This can be seen in **figure 4.8** as the literature values show a wide variation.

4.4.6. The influence of carbon and Carbon Steel results

As mentioned earlier, groove decay measurements were made in pure iron in order to benchmark the *in situ* measurements and to compare the subsequent calculated surface diffusion coefficients with values reported in the literature. However, recent developments in focused ion milling techniques have allowed us to produce dimensionally well characterised grooves on the surface of our specimens and this advanced grooving technique is used for the remainder of the study.

Thus surfaces were grooved using the Focused Ion Beam mill described earlier and an example of a surface produced in this fashion is shown in **figure 4.4**. The surface diffusion coefficients calculated from groove-decay measurements for carbon steel are shown in **table 4.2**. Surface diffusion coefficients were obtained at a range of temperatures for a Fe-0.9C steel (see **table 4.2**) in the gamma phase in order to compare the diffusion coefficient in this alloy to that of pure iron. Measurements were made in Fe-0.4%C and Fe-1.5%C steels in order to determine to what extent the diffusion coefficient depends upon carbon.

4.4.7. Surface diffusion in a Fe-0.9C carbon steel

In the case of Fe-0.9C carbon steel the development of this technique was at such a stage that the decay of sinusoidal wave pattern was being observed with time. This technique takes advantage of equation 4.9 enabling a unit-less observation of the change in amplitude with respect to time that is linear. In principle this means that a measurement of the topography can be taken at the beginning and the end of the heating cycle. This principle was tested for straight line accuracy at 1200°C shown in **figure 4.9**. In this figure there is precise agreement with a straight line. The disadvantage in this technique is that the depth of the specimen cannot be measured by confocal microscopy and so the specimen needs to be removed so it can be measured by atomic force microscopy.

This meant that samples could be contaminated through exposure to air and by handling of the material. All other results were subsequently measured via a depth measurement at the start and finish of the experiment over a period of six hours without removal.

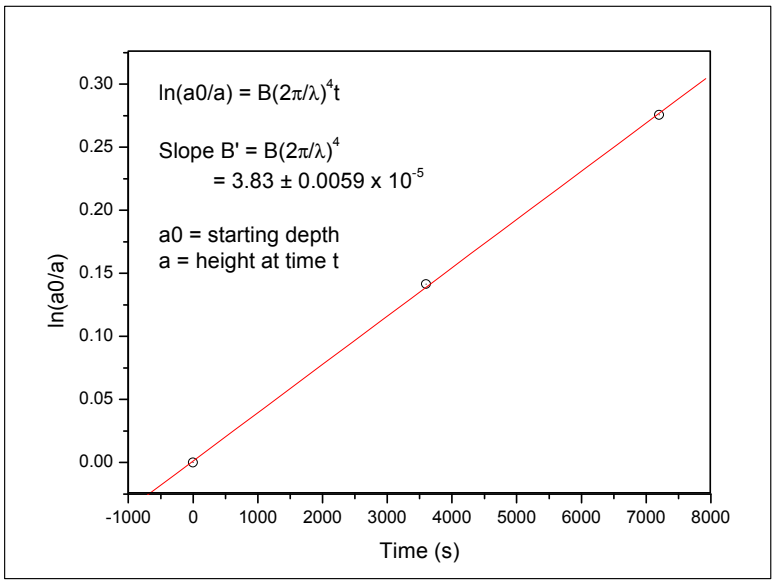

Figure 4.9: A test of the straight line accuracy of the results at 1200°C. The figure shows two intervals of one hour.

It was important then to measure more results at different temperatures in order to ensure that a smooth curve for the surface diffusion coefficient was obtained. The results of this are shown in **figure 4.10**.

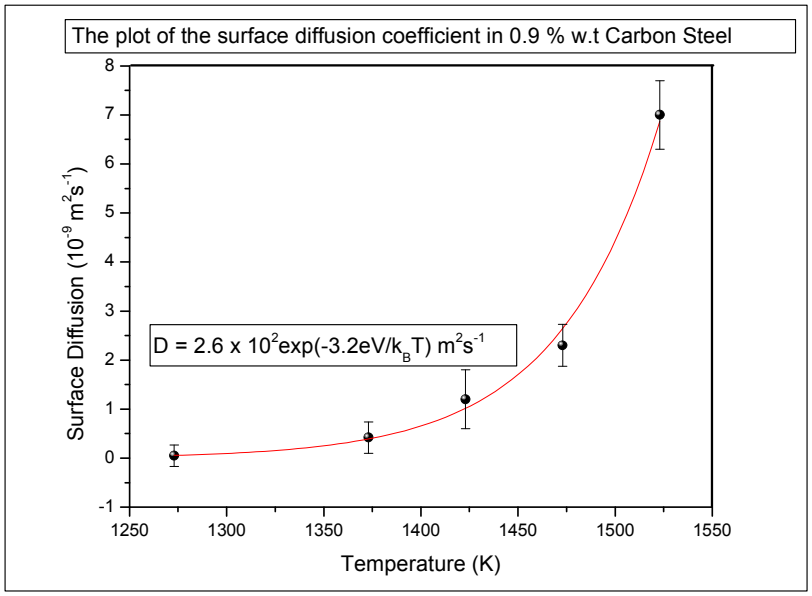

Figure 4.10: A complete set of surface diffusion coefficients in Fe-0.9C steel.

This graph shows the results follow a smooth curve with very little variation. Despite the apparent accuracy of these results, this technique did not take full advantage of the confocal microscope that has the potential to prevent contamination of the sample. The confocal microscope is highly accurate in taking measurements of surface scratch width. The overall result for the diffusion equation for Fe-0.9% carbon steel is therefore:

$$D_s = 2.6\times10^2 \exp\left(-\frac{3.2\pm0.1eV}{kT}\right) \quad (\mathrm{m^2s^{-1}}). \tag{4.19}$$

4.4.8. Results for Fe-1.5C carbon steel

Surface diffusion coefficients in Fe-1.5C steel were measured using a single groove created in the ion beam mill. Over a period of only four hours several clear measurements of width were obtained for Fe-1.5C steel shown in **figure 4.11**. In these results a smooth curve was obtained obeying the theory in equation 4.14.

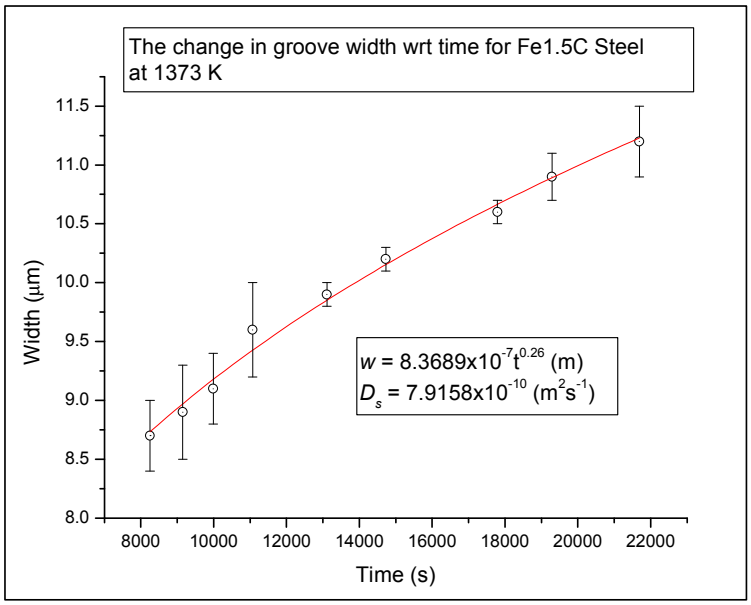

Figure 4.11: The measurement of width broadening with respect to time for Fe-1.5C steel at 1100°C.

4.5. General discussion

The results obtained for surface diffusion coefficients in iron and iron alloys, are the products of an evolution of a technique of measuring surface diffusion coefficients. The different approaches taken over time have various advantages and disadvantages and the aim of developing this technique has been to optimise between streamlining this technique and being more certain of the techniques accuracy.

In the case of pure iron, the samples were prepared by way of polishing and mechanical etching to obtain the required surface geometry for delta iron using a sinusoidal wave pattern. In the gamma iron region thermal grooves were grown on the surface and their decay was observed with time. A single mechanical scratch was not considered as the scratch profile did not conform well to the geometry modeled by the theory. Tests were performed with single scratches matching the profile in **figure 4.1a**. These tended to narrow in width with time. This is due to the fact that since the scratch is surrounded by a flat surface the only gradient was toward the centre of the profile. Profiles matching the one in **figure 4.1b** are curved on either side. These outward ripples provide the necessary gradient for matter to migrate away from the centre.

If it can be obtained, the ideal surface profile to be measured is a naturally occurring thermal groove that progresses to decay. These grooves tend to be difficult to find and they do not tend to decay reliably at the point in time you wish.

Mechanical etching of a sinusoidal pattern is very quick and a surface geometry available to observe is guaranteed. Mechanical etching of this kind of pattern does not ideally conform to a sinusoidal pattern (see **figure 4.5b**) and there is the concern that this will introduce errors by way of its irregularity. The other concern is that the confocal microscope does not measure depth directly but relies on the decrease in signal amplitude as the wave amplitude decreases.

The introduction of the ion beam mill enabled the possibility of creating an ideal geometry on demand. A sinusoidal pattern can be created in less than two hours and

will generally decay according to the theory. The main problem with the sine wave pattern is that if the diffusion coefficient is slow at a given temperature the confocal optics will not measure a change. This means that the atomic force microscope is needed to measure the small change with time. This was true for the high carbon steels especially at low temperatures.

Using the atomic force microscope in combination with the confocal microscope as mentioned does introduce the potential for contamination. In addition the confocal microscope only plays the role of a furnace. This technique is also not very streamlined and makes the process more time consuming.

If special care is taken to create a groove-geometry in the ion beam mill this can be reliably measured for width broadening and is adaptable to a wider range of temperatures.

Despite the various advantages and disadvantages of different approaches to measurement, when comparing the results of different alloy compositions there is an trend in how the surface diffusion coefficients behave. Carbon content of the iron does make a difference to the rates of surface diffusion. This can be noted by the results in **table 4.2**, and presented graphically in **figure 4.12**.

The figure and table show that there is only a slight drop in surface diffusion rates when passing from pure iron to Fe-0.43C. However when the content of carbon is higher at 0.9% carbon the rates of diffusion drop by just over two orders of magnitude and remain

this way in the case of Fe-1.5C steel. The point to note for the 0.9% carbon steel is that it does contain alloying elements although in small quantities. This may artificially drive the diffusion rates down lower. In the most conservative case it can be said that alloying elements will lower the diffusion rates and this is consistent with claims in the literature.

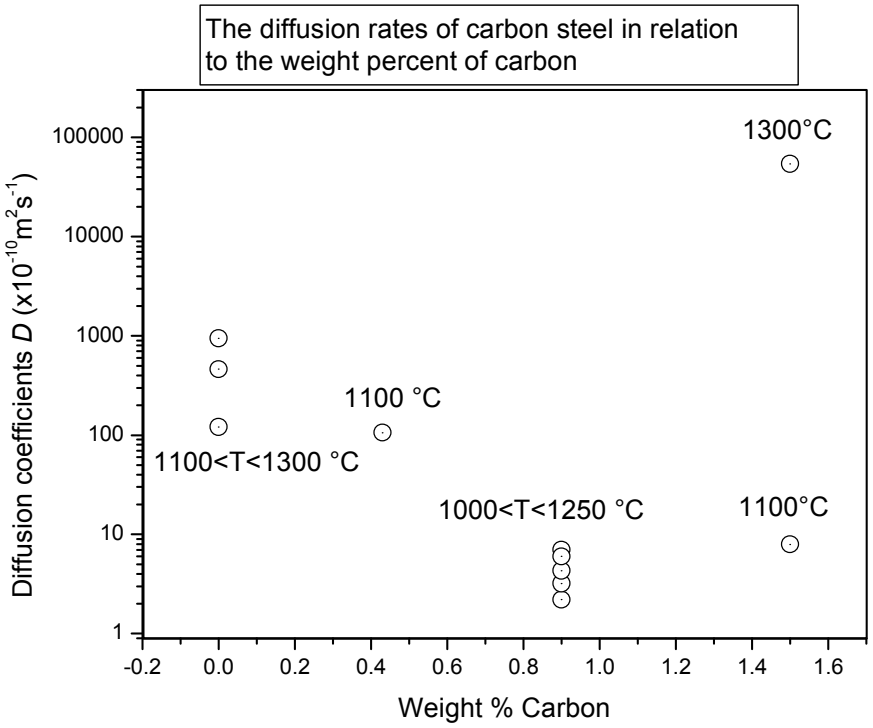

a)

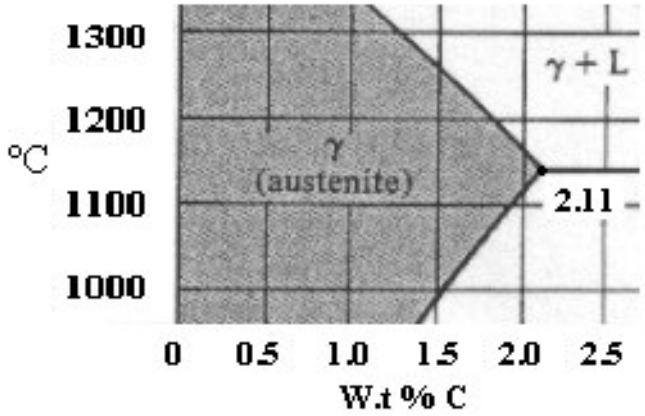

b)

Figure 4.12a-b: **a)** The comparison of surface diffusion rates for various alloys. **b)** The portion of the iron-carbon phase diagram studied for surface diffusion.

4.6. Conclusions

The work presented in this chapter shows the progress and development of a new technique of measuring surface diffusion coefficients in metallic systems using a combination of High Temperature Laser Scanning Confocal Microscopy and Focused Ion Beam Milling (ConFIB Microscopy).

It has been determined that the optimal approach to measurement is to create a single groove profile using focused ion beam milling that closely resembles a thermal groove that evolves naturally on the surface. Atomic force microscope scans of samples prepared in this way show a close match to a naturally occurring thermal groove.

The ConFIB technique is capable of producing reliable results for surface diffusion coefficients ensuring that system contamination is minimised and time efficiency is maximised. This makes the technique accessible for industrial use.

Whilst the exact effects of oxide and oxygen contamination are not studied here quantitatively, the ConFIB method ensures that contamination of the system is reduced to a level of efficiency greater than existing techniques.

Complete equations for the surface diffusion coefficients in pure iron and 0.9 percent carbon steel were obtained using this technique and were shown to be:

γ-Fe: $$D_s(T) = 3.00 \times 10^{-2} \exp\left\{-\frac{1.69 \pm 0.3eV}{k_B T}\right\} \quad (\mathrm{m^2 s^{-1}})$$

δ-Fe: $$D_s(T) = 1.51 \times 10^{2} \exp\left\{-\frac{2.86 \pm 0.1eV}{k_B T}\right\} \quad (\mathrm{m^2 s^{-1}})$$

γ-Fe-0.9C: $D_s(T) = 2.60 \times 10^2 \exp\left\{-\frac{2.30 \pm 0.1eV}{k_B T}\right\}$ $(m^2 s^{-1})$

There is evidence to throughout the results for surface diffusion in iron and carbon steel, that carbon content has the effect of reducing the rate of surface diffusion past the point of 0.5-0.8 percent by weight of carbon. This reduction is significant and can be as much as two orders of magnitude when carbon content is up to 0.9-1.5 percent by weight of carbon.

Chapter 5:

Physical properties and high temperature sticking tests for 0.9 and 1.5 percent by mass carbon steel.

Chapter 5: Physical Properties and high temperature sticking tests for 0.9 and 1.5 percent by mass carbon steel.

5. Introduction

In earlier research relating to sticking of iron ore particles in the FINMET™ reactors at Port Hedland, correlations have been found between the degree of sticking the type of iron ore particles and the extent to which the particles are reduced. The sticking of iron ore particles seems to reach its peak in the second last stage of reduction in reactor two, when the particles are almost completely reduced and the carbon content is in the range 0.4 – 0.9 percent carbon (or an average of 0.5 percent). These trends were verified by a controlled study at the BHP-Billiton New Castle laboratories.

Sticking tests were carried out on reactor samples captured at the peak of metallisation in reactor two and at the peak of carburisation in reactor one where the carbon content is on average 1.5 percent and the reduction is almost complete. In these earlier studies, it was found that the product of reactor 2 that contains about 0.5 %C had a far greater tendency to stick than the reactor 1 product that contained 1.5%C.

In the presents study an attempt was made to quantify the sticking tendency at high temperature in test samples that resemble the iron ore samples containing 0.5 and 1.5 percent carbon respectively. These experiments were specifically designed to assess the sticking propensity of iron based particles as a function of carbon content and to test the proposal by Dippenaar[25] that fully carburised surfaces will reduce the sticking tendency.

5.1. Material composition of samples

Two types of sample were selected for high temperature sticking tests. One sample, matching the Reactor 2 product contains 0.9 percent by mass of carbon, denoted Fe-0.9C. The other contains 1.5 percent by mass of carbon, denoted Fe-1.5C. The compositions of these two materials are the same as those described in chapter 4 (see table 4.1b). The Fe-0.9C alloy used is a commercially available steel commonly known as "silver steel" and the Fe-1.5C sample is a specially manufactured high purity iron-carbon alloy obtained from Special Alloys™.

5.1.1. Phases present for a given temperature

High temperature adhesion tests were conducted in the temperature range 600-900°C. In the pure Fe-1.5C alloy the phase compositions at a given temperature are easily determined from the diagram shown in **figure 5.1**.

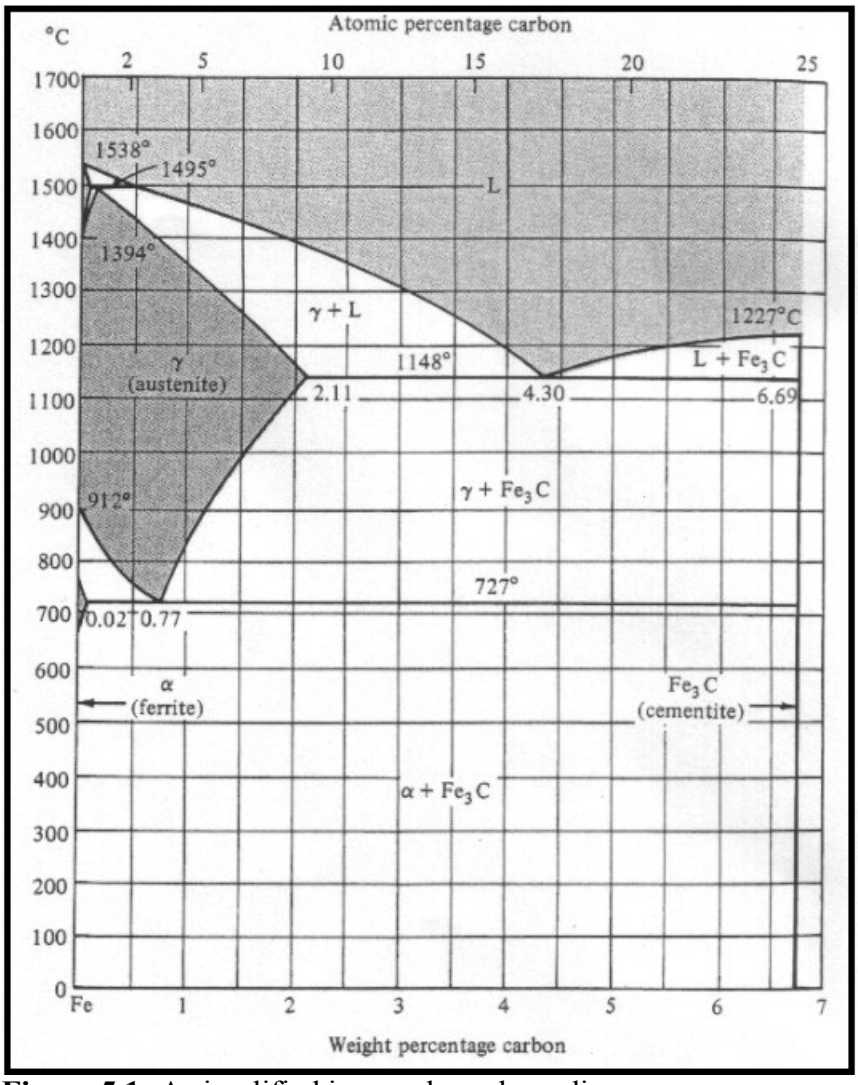

Figure 5.1: A simplified iron carbon phase diagram.

However, the commercial Fe-0.9C steel contains carbide formers and the phases present at a given temperature will be a function of the thermal history. Hence it was necessary to determine experimentally the exact phases present in the Fe-0.9C steel between 700 and 900°C.

5.2. Dilatometry

A Theta Industries-Dilatronic Dilatometre™ was used to determine the exact temperature at which the α to γ phase transition occurs in this Fe-0.9C steel at given heating and cooling rates. Tubular samples were machined to 10 mm long, 5 mm in diameter with an inner diameter of 3.5 mm. The temperature was recorded by a set of type K thermocouples (Ni-Cr, Ni-Al) spot-welded to the sample. The samples were heated at a rate of 100°C per minute. The dilatometer traces are shown in **figure 5.2.**

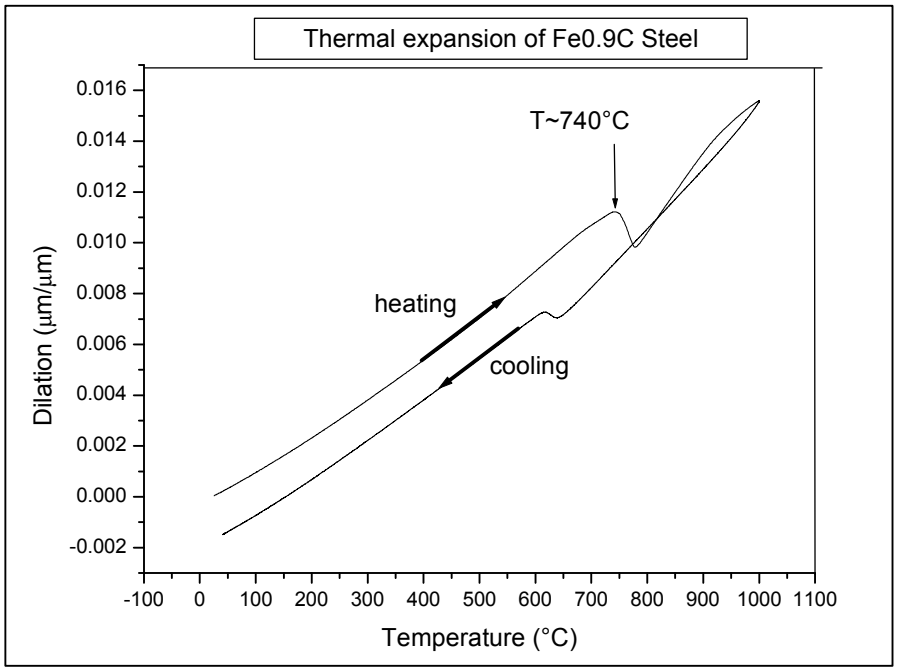

Figure 5.2: A dilatometer curve showing the linear expansion of the Fe-0.9C steel. The α to γ phase change occurs at approximately 740°C.

5.3. High temperature adhesion tests

In an attempt to provide a more quantitative assessment than the sticking test described by Shook and Honeyands[3] to determine the sticking tendency of Fe-C alloy particles, a new adhesion test was developed. High temperature quantitative adhesion tests were carried out at Wollongong University for samples of Fe-0.9C and Fe-1.5C in order to compare them with results found at BHP-Billiton. In addition, the tests were done to provide information on the difference between the adhesion behaviour of Fe-0.9C and Fe-1.5C steel.

5.3.1. Experimental approach to adhesion tests

The newly developed adhesion test is carried out on a Gleeble 3500 thermo-mechanical simulator (*Gleeble*). The *Gleeble* is capable of performing integrated, digital, closed loop controlled thermo-mechanical testing. Programmed automatic or manual control testing is achieved via a series 3 digital control-system. The *Gleeble* mechanical testing system utilises a hydraulic servo capable of controlling tension and compression modes of up to 10 tons of force. The *Gleeble* is capable of control line stroke, stress, strain and force under conventional tensile and compression tests. Samples in the *Gleeble* are resistance heated in a vacuum as low as ~10^{-3} Torr or under controlled gas atmosphere and under controlled heating rates of up to 10^{4}°C/s can be achieved.

In order to conduct the adhesion tests, the *Gleeble* operation had to be slightly modified. For conventional tensile tests in the *Gleeble*, samples are machined into cylinder shape, 115mm in length and 10 mm in diameter. The sample is clamped by copper grips in the

jaws of the *Gleeble* and C-shaped clamps are used to hold the copper grips in position. Two type K thermo-couples are welded at the centre of the sample in order to record temperature.

Samples prepared for adhesion tests in the *Gleeble* are cut to just over 155mm to ~120mm in length. The sample is tapped at each end with a 15 mm thread and is cut exactly in half. The two ends of the sample are then machined level in a lathe leaving a sinusoidal pattern of ripples on the surface as shown in **figure 5.3a**. The sinusoidal ripples on the surface provide a curvature difference between the surfaces such that diffusion can occur.

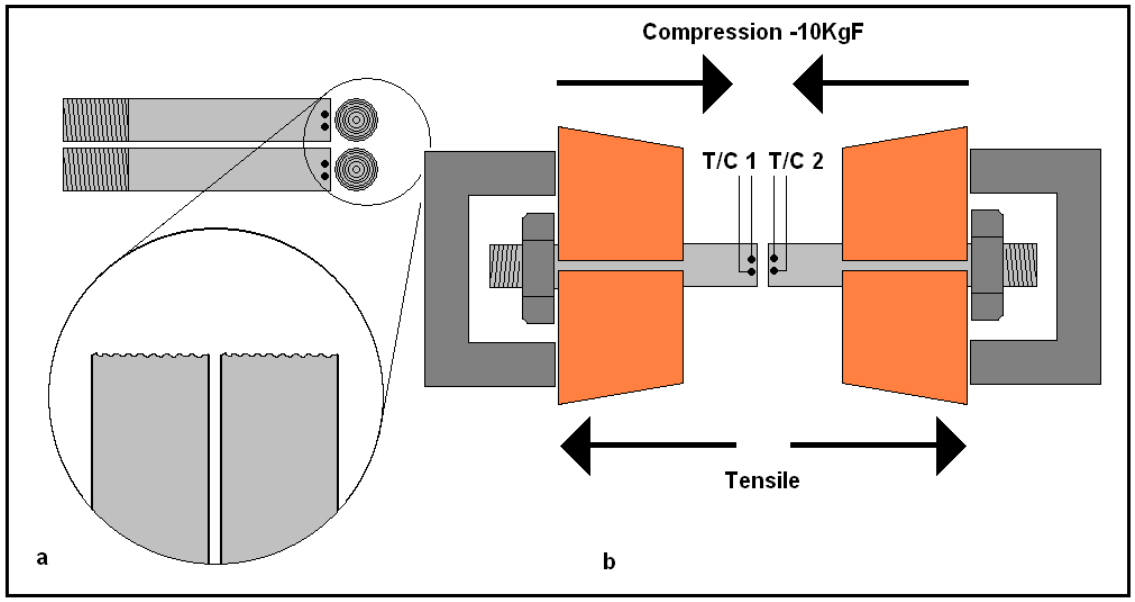

Figure 5.3a-b: a) A schematic representation of the samples used in the adhesion tests. **b)** A schematic representation of the experimental set up of the adhesion test.

The samples are inserted into the *Gleeble* as shown in **figure 5.3**. The two ends of the samples are brought under a compressive force of 100 N with respect to the ends surface area. Once the samples are in contact under a constant pressure, the *Gleeble* chamber is pumped down to a vacuum of ~10^{-3} Torr. The samples are then heated at a rate of 60°C/minute to a pre-determined temperature and allowed to soak at that

temperature for five minutes. One second before the samples are ready to be separated the heating power is cut. This procedure is followed in order to eliminate electric arcing and spot-welding of the surfaces. When the power was turned off, the temperature dropped by less than 50°C. The samples are then separated at a slow strain rate of 3mm/minute. Measurements of stroke, force, temperature and the power input were continuously recorded.

This procedure ensured that contacting surfaces made sufficiently good contact so that arcing did not occur and so that the force required to separate the two contacting surfaces could be used as a reliable measure of the tendency of the material to stick at temperature.

5.4. Results

Adhesion tests were conducted across a temperature range of approximately 550<T<900°C. An example of these results is shown in **figure 5.4a-b**. **Figure 5.4a** shows an adhesion test for the Fe-0.9C steel at 750°C showing the temperature, force and the power input with respect to the time. The top curves (marked "1"), show the heating of the sample to temperature, holding for five minutes and then the separation of the samples. The curve second from the bottom (marked "2"), is the power input and the bottom curve (marked "3"), represents the force. The peak shown at the far right is the peak force at separation of the two samples. The second graph (**figure 5.4b**) shows a close up of the peak force region. This graph shows that at the time of peak force the power input is zero and the temperature drop is approximately 25°C making the effective test temperature 725°C in this case.

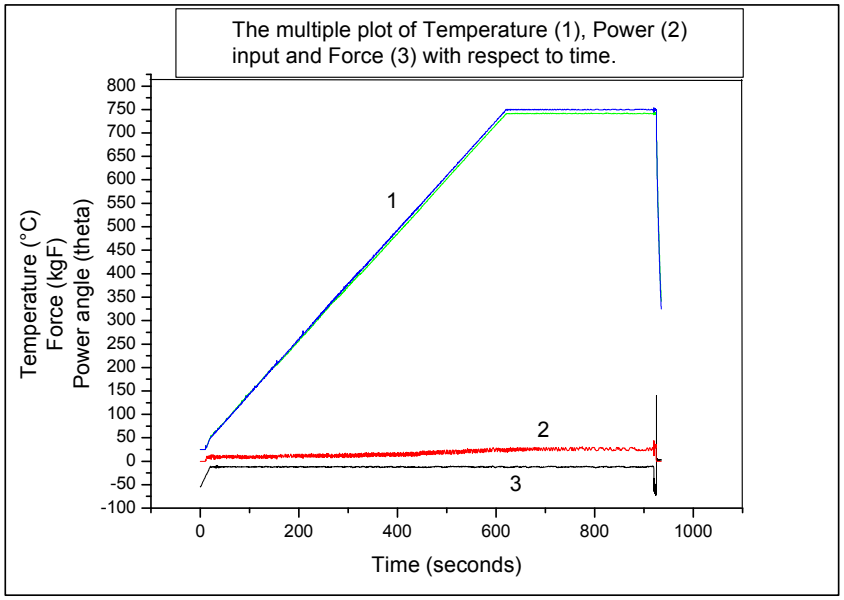

a)

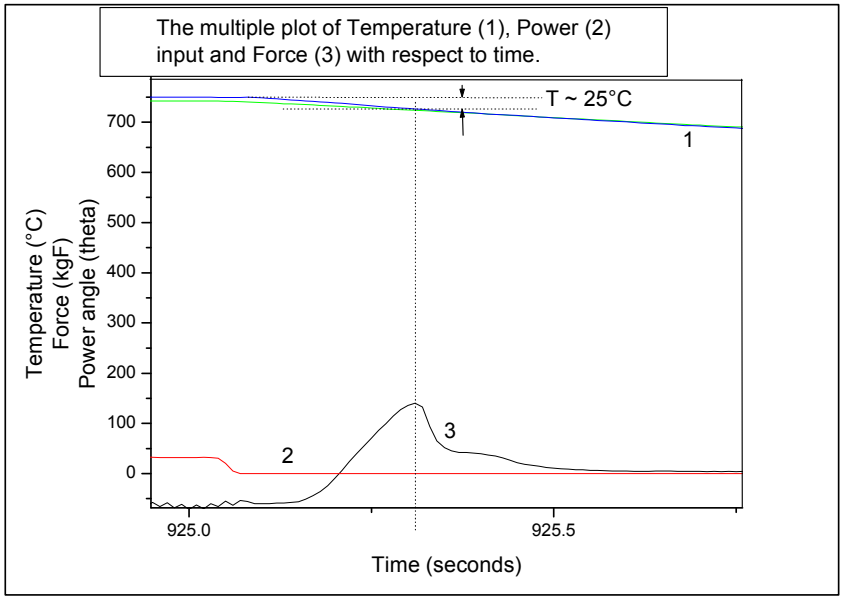

b)

Figure 5.4a-b: a) The entire curve of force, temperature and power input with respect to time in Fe-0.9C carbon steel for 750°C. **b)** The same graph focused in on the peak force showing zero power input and a moderate drop in temperature of 25°C.

The maximum pull-off force, measured from the peak of curve three shown in **figure 5.4b**, were determined at several predetermined temperatures and repeated for least three trials at each temperature. The force measurement however is not a definitive

measure of the adhesion for a particular temperature. Every sample did not contact and stick with exactly the same surface area. When the samples were inspected there was usually an elliptical region where the two surfaces were in true adhesive contact. The surface-areas of these elliptical contact points were measured individually using Vernier calipers and calculated using the formula for an ellipse.

The force of contact is converted into a measurement of the stress of adhesion and the results for the Fe-0.9C steel and the Fe1.5C alloy are shown in **figure 5.5**.

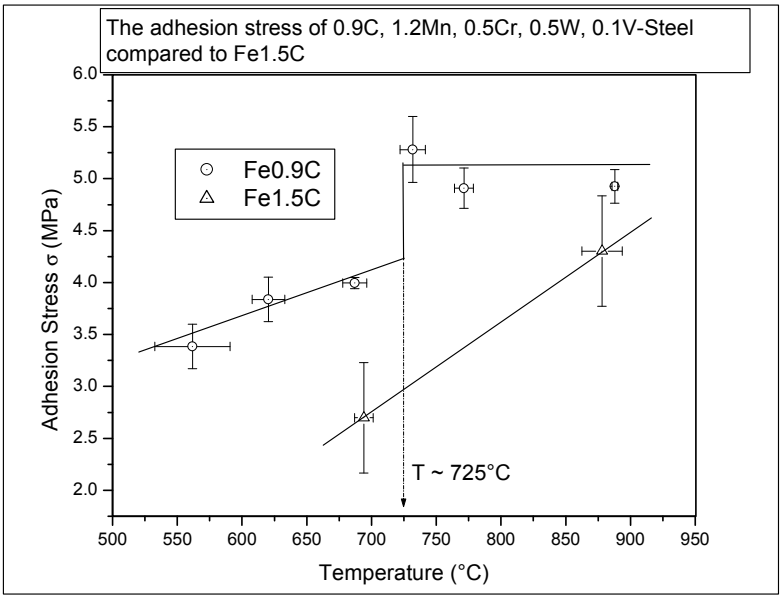

Figure 5.5: Stress of adhesion of the Fe-0.9C steel and the Fe-1.5C alloy as a function of temperature. The error bars encompass the variation across 3-4 tests per temperature.

5.5. Discussion

High temperature adhesion tests between well-defined metal surfaces, particularly at such high temperatures, have never before been quantified under such controlled

conditions as far as the author is aware. It is therefore important to highlight the advantages and potential errors of this technique.

5.5.1. Assessment of the accuracy of the technique

The first issue with this technique relates to the accuracy and sensitivity of the 10 Ton loading cell (i.e. ~10^5N) of the *Gleeble*. In a typical measurement of the tensile stress of Fe-0.9C steel the tensile stress in the temperature range studied is of an order between 100-300 MPa (see **figure 5.6**).

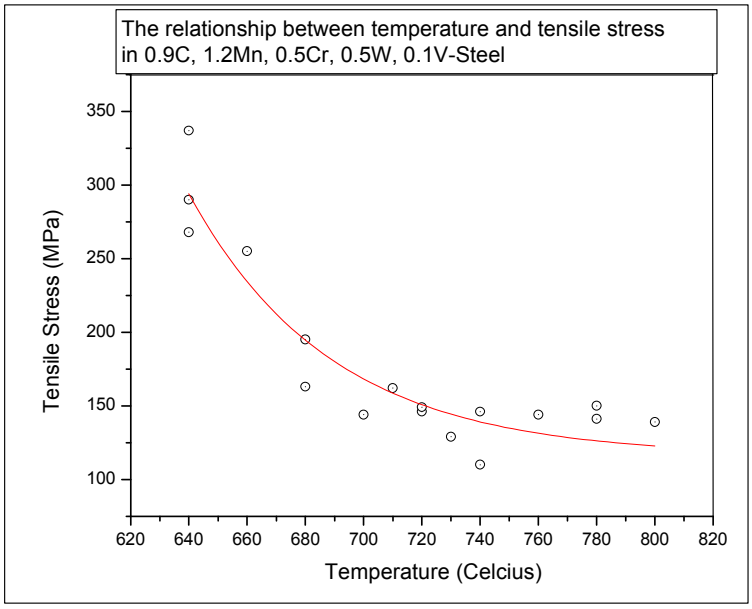

Figure 5.6: The tensile stress of Fe-0.9C steel as measured in the *Gleeble*.

The stresses measured for the adhesion tests begin with an applied pressure of not greater than ~1-1.2MPa. The stress of adhesion, measured as the force of separation is between 2.5-5MPa. This magnitude of stress is between 1-2% of the tensile stresses normally measured in this machine. The sensitivity of the adhesion tests for example are indicated by the error bars of **figure 5.5**. The variation here is approximately

±0.5MPa, yielding an error of up to 25%. It would not be advisable therefore to take these stresses as a precise measurement of a sticking force at a particular temperature. However, it would be reasonable to suggest that these quantities measure a reasonable quantitative trend in adhesion force in relation to temperature. This assessment is not unreasonable as the results show little scattering in **figure 5.6**, at a particular temperature in repeated tests. Viewing the curve, the rise in the force does not fluctuate as the temperature rises nor does it fluctuate from one test to another for a particular temperature. If errors are creeping into the result it is a sensitivity error that remains constant and thus the relative change is reliable.

The other issue is the switching off of the heating power once the tensile phase of the operation begins. It has been said that in order to eliminate welding effects the power needed to be shut down. This introduced a drop in temperature. The drop in temperature of ~25°C however is not high at the time of the peak force of separation. The temperatures for all tests dropped by a consistent temperature in all cases to within ±2°C. The temperatures reported are the real temperatures at the time of peak force of separation and not the programmed temperatures.

5.5.2. Adhesion stress as a function of temperature

The experimentally measured adhesion stress of the Fe-0.9%C steel increases linearly with temperature up to the phase change from alpha to gamma as shown in **figure 5.5**. The step-change in adhesion stress at the eutectoid temperature provides evidence of the accuracy and sensitivity of the measuring technique. In the two-phase region ($\gamma + Fe_3C$)

between 725 and 740°C the adhesion stress attains a peak and then is constant in the gamma (FCC) phase in the temperature range investigated.

A major physical-mechanical difference between the BCC and the FCC phases is the yield strength and the hardness of the material. In general, metals in the BCC phase are much harder than the FCC phase. The BCC phase can display yield strengths an order of magnitude or more than the FCC phase in pure materials, and for iron in the BCC phase the yield stress is always high despite impurities[119]. This is born out by a general decrease in tensile stress as **figure 5.6** shows.

5.5.3. The effect of carbon content

A main observation in the adhesion of iron ore particles in the FINMET™ was that particles of higher carbon content were resistant to adhesion. Adhesion tests were carried out on a pure Fe-1.5%C alloy. These tests confirmed that the Fe-1.5C alloy had less propensity towards adhesion.

These results shown in **figure 5.5** are qualitatively similar to the results obtained in the BHP-Billiton laboratories (note **figure 5.7** for a comparison).

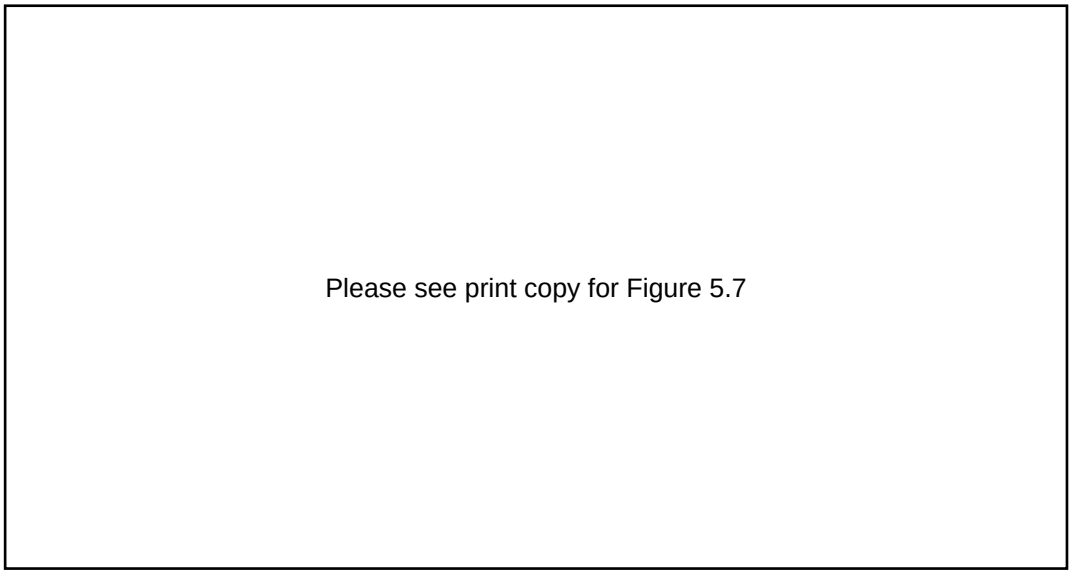

Figure 5.7: The results of the angle to failure sticking tests at BHP-Billiton. Reactor 2 products hold the 0.5-1.0% carbon steel and reactor 1 holds the Fe-1.5+C steel[3].

In comparing **figures 5.5** and **5.7**, is has to be remembered that steels were used in the Gleeble tests while actual fluidised-bed reactor product was used to determine **figure 5.7**. However, there is a remarkably good correlation between these two tests, providing confidence that the carbon content of the Fe, and hence the phase composition at a given temperature plays an important role in determining the sticking tendency.

During carburisation of iron particles in the fluidised bed reactor, carbon diffuses into the iron and a thin Fe_3C layer is formed on the surface of particles at sufficiently high carbon activity in the reduction gas. Hence, when highly carburised particles come in contact, it is essentially Fe_3C/Fe_3C contacts that are formed (see chapter 2; section 2.10.1).

It is pertinent to compare such contacting Fe_3C/Fe_3C surfaces with the surfaces of the steel samples that were brought into contact in the Gleeble tests. In the Fe-0.8%C alloy,

ferrite/ferrite surfaces are in contact at temperatures lower than the α/γ phase transition and γ/γ interfaces are in contact at higher than the transformation temperature. In the Fe1.5%C alloy, austenite grain boundaries are delineated by primary Fe_3C in the two-phase ($\gamma + Fe_3C$) field in the approximate temperature range 750°C to 900°C. This Fe_3C network evidently prevents γ/γ contacts and adhesion is less than that of pure γ/γ interfaces. If the temperature is high enough to render a fully austenitic structure, γ/γ contacts are made and the adhesion stress approximates that of the Fe-0.8C alloy.

5.6. Conclusions

This study has revealed the results of the first well controlled high temperature adhesion test for metallic surfaces capable of giving quantitative adhesion stresses with an order of magnitude accuracy. The relatively low error range of the plot of adhesion results shows that the procedure can produce good results for comparison of adhesion properties of different materials at high temperature.

There is good agreement between the results of the industry based "sticking test" conducted by Shook and Honeyands[3] and the Gleeble tests of this study on well defined metallic surfaces of similar carbon contents to the HBI reactor products.

Results suggest, that the property most likely related to adhesion at high temperatures is the presence of cementite in the material. Comparing the high carbon and low carbon steel, there is an observable difference in sticking tendency. The high carbon steel exhibits a lower adhesion stress to that of the low carbon steel both above and below the eutectoid temperature. The fraction and distribution of cementite in this alloy at

temperatures in the two-phase field ($\gamma + Fe_3C$) is thought to account for the difference. It is thought that a carburised layer on the surface of the iron would further decrease adhesion stress.

Chapter 6:

Fundamental mechanisms of sticking: General analysis, discussion and conclusions

Chapter 6: Fundamental mechanisms of sticking: General analysis, discussion and conclusions

6. Introduction

It was the objective of this study to examine experimentally and theoretically the possible mechanisms responsible for the phenomena of adhesion of partially or fully reduced iron ore particles in a fluidised bed. It has been explained and described in the literature review that the premature agglomeration of particles in this process has been ever present.

The majority of the industrial work undertaken to remedy the problem of agglomeration has been concerned with the manipulation of plant-scale industrial parameters such as production temperatures, pressures, gas mixtures and some surface analysis. Many useful correlations have been found that indicate when sticking is predominant and when it is minimised. Unfortunately, these considerations have not eliminated sticking altogether. The most effective attempt to eliminate sticking has been the use of MgO additives in the reduction process. Despite the effectiveness of this technique, the exact mechanism by which MgO additions prevent sticking has not been established.

It has not been possible to identify the fundamental mechanisms of sticking or agglomeration and its remedy most possibly because of the industrially oriented focus on the problem. Because plant based studies are generally not designed to gain fundamental explanations it is instructive to turn to fundamental analysis to gain enhanced insight.

It is for this reason that a study of the fundamental properties of the adhesion process was undertaken. It was important from the outset to identify the forces and binding processes that take place when two particles make contact at their surfaces.

In this chapter, a review is given on how the system is defined and what elements are involved in causing adhesion particular to that system. Quantitative values gathered for these elements are summed up. Finally, a theory is offered based on this data of the primary adhesion mechanisms.

6.1. The system studied and potential adhesion mechanisms

6.1.1. System complexity

It is important to note that the real system inside a fluidised bed reactor is extremely complex and has almost limitless potential for variation.

No two ore samples from different locations are identical. Atmospheric conditions of reduction such as gas composition, pressure and temperature can have a multitude of combinations and all can, as noted in chapter two, affect the adhesion between particles.

When iron ore particles are reduced to metallic iron their impurity levels will vary depending on the ore type and reduction gas. This can potentially affect the outcome of adhesion indirectly via diffusion[120]. It is found at Port Hedland that alloy composition can affect adhesion. In addition, surface additives of MgO can as mentioned, affect adhesion.

In chapter two an outline was given on the work conducted to date in an attempt to find a solution to the problem of agglomerating of particles in fluidised beds. The research from the 1960's covers a diversity of experiments that have catalogued the conditions in a fluidised bed that are most likely to lead to adhesion of particles. This research has certainly assisted the Port Hedland production team to reduce the problem. However agglomeration of fully or partially reduced iron ore particles remains an impediment to gaining desired production output.

The approach to date has been a so-called top down approach to the problem. Workers have constructed a variety of situations and made some very useful correlations. However, general principles and fundamental mechanisms have not been identified.

In this study an attempt has been made to draw some general principles and apply them to the problem at Port Hedland. In this study a more bottom up approach has been taken.

6.1.2. Mechanisms of adhesion studied

The possible mechanisms of adhesion are outlined in section 2.9. Metallic bonding and sintering were considered seriously in this study. The cohesiveness of a substance is the most obvious fundamental mechanism of adhesion. The hardness of a surface has been shown in the past to be roughly proportional to the chemical binding energy of the substance[121].

Sintering as an adhesive mechanism, breaks down into several other sub mechanisms. For reasons discussed below, the first two mechanisms "adhesion" and surface diffusion were considered important in sintering as an adhesive mechanism. Depending on the system, adhesion may involve van der Waal's forces, electrostatic forces, capillary forces and perhaps magnetism[58, 59, 69].

Other adhesive mechanisms considered were whisker growth and frictional forces due to surface roughness. In the Port Hedland reactor, the particular gas mixture discourages whisker growth. Frictional forces were not studied as surface roughness is a highly variable phenomenon. In addition, there is a problem in reaching consensus in defining what the origin of frictional forces really is. Frictional forces also have the exacerbating problem of a discrepancy between the frictional forces measured at atomic scales and those measured at the macro scale[122-124]. It is for these reasons that friction was not studied.

The atmosphere in the Port Hedland reactor is not likely to have a problem with capillary forces arising from water vapour as there is typically no water in the system. Electrostatic and magnetic forces may be present in the system. However, if they were present they would be random events and would not follow such a consistent pattern as to be primarily responsible for adhesion. Electric charging is notoriously capricious, as charging may or may not occur depending on the electronic properties of the materials surfaces in contact[58]. As temperatures are increased beyond a materials ferromagnetic curie temperature (about 770°C+ for iron) the material is no longer ferromagnetic. The material then becomes paramagnetic and it is unlikely to maintain a consistent magnetic field at temperatures of 750°C[87].

Following this rationale the mechanisms of iron particle adhesion considered of primary importance in this study were van der Waal's forces, surface diffusion and the physical properties of the material such as hardness, tensile strength and high temperature quantified sticking properties under controlled conditions.

The system of study is outlined in section 2.10. It was the aim of this study to quantify the mechanisms stated above and make several comparisons between substances that stick and those that do not stick very much. Essentially the reactor-2 product, generally consistent with a 0.5-1.0 % by mass of carbon will stick more that the reactor-1 product containing 1.5 %C and more. The other major factor to be considered is temperature. Above the eutectoid temperature sticking was extensively observed, below, it was minimal.

To simulate the interaction between the surfaces of the particles products of the FINMET™ we chose specially manufactured and commercial carbon steels. This was partly done in order to simplify the system for study. It was considered most important to focus on the variables that are similar to all situations where adhesion is concerned rather than the myriad of variables that are not common and have a potentially minor effect on the outcome.

6.2. Analysis and application of results

The question remains as to what the divers results of van der Waal's forces, surface diffusion, high temperature adhesion and the physical properties of hardness and yield strength have to do with understanding the sticking problem. It is not argued here that these mechanisms are the only mechanisms involved in sticking. It is only argued that these mechanisms are ever present when iron particles make contact. It is also argued that in the most conservative estimate, if these mechanisms were the only ones present, that they would be more than sufficient to account for the sticking problem and are indeed fundamental to it.

The various quantities that have been experimentally derived and presented in the previous chapters of this thesis will in this chapter be applied to the probable scenario of a typical system of iron particles coming into contact in the reduction process at the stage of iron ore metallisation prior to carburisation. To guide us through this analysis lets us outline the steps of metallisation and the contact process.

Initially we must go back to the reduction stage of metallisation and ask, "What type of surface does metallisation create?" In chapter two it was argued that metallisation of and iron ore particle occurs via the Wagner mechanism of reduction, and, what is controlling the rate of reaction, determines the surface topography. Recall that if the diffusion of iron ions to the surface is rate controlling, then iron "platelets" will form all across the surface and eventually merge. This is the ideal case for reduction as oxygen removal control leads to whiskers that are correlated with sticking. Given that the reaction is diffusion controlled, the surface in the early stages will look like **figure 6.1**.

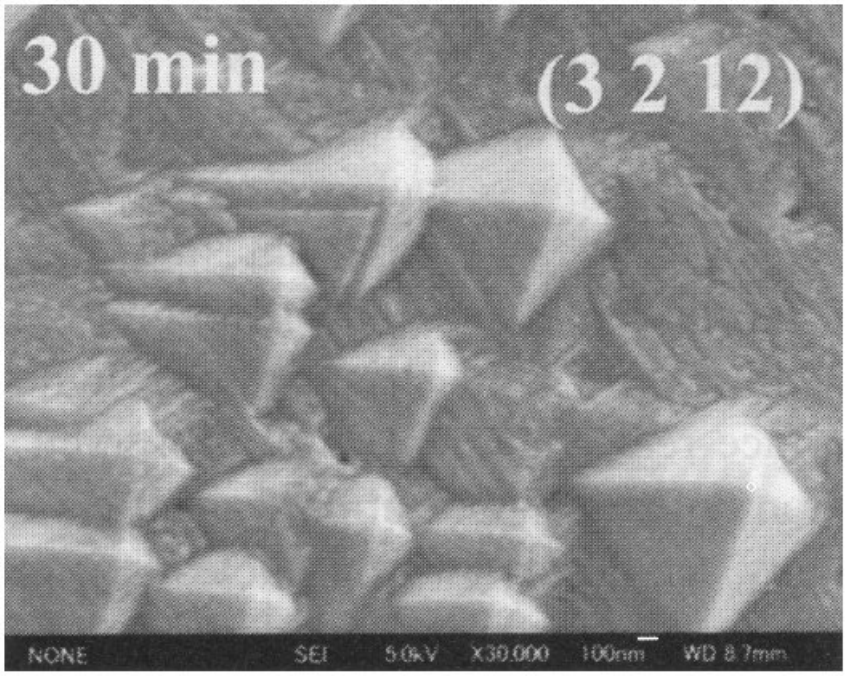

Figure 6.1: A typical image of iron "platelets" formed under diffusion control[41]. Note that the platelets are associated with a tiny radius of curvature of approximately 20nm at the tip.

These will continue to nucleate and cover the surface and produce a "sponge" iron layer. A typical layer of this sort is covered with ripples with radii of curvature of approximately 1 micron as shown in **figure 2.11**. Particle contacts are made at all stages of reduction in a fluidised bed. However it is the stage at the onset of metallisation that is of particular interest as this is the point where sticking and defluidisation begins[5]. It is of course true that surface ripple curvatures can be much larger than 1 micron. However, typically they are small, and when understanding the adhesion process *in situ* the local conditions are what determine the degree of adhesion and not the overall particle radius.

In our analysis then, we have a typical particle of metallising ore coming to rest on other particles with local surface ripples having radii of curvature somewhere between 20nm and 1-2 microns as schematically shown in **figure 6.2**.

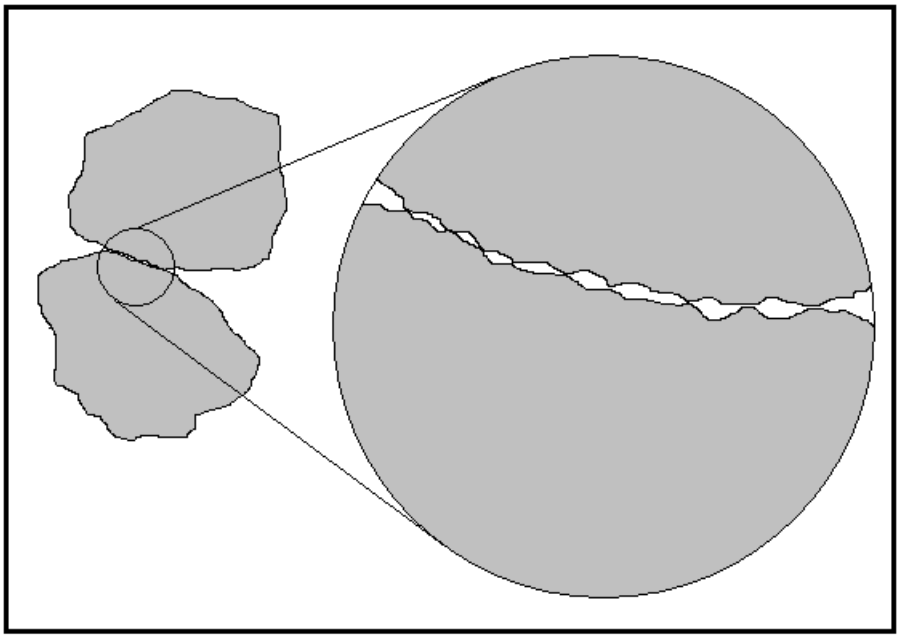

Figure 6.2: Typical iron particle contacts at any particular stage of metallisation. Although the overall surface may be reasonably smooth at larger scale lengths, the local conditions of contact represent a multitude of particle radii coming into contact.

When the local surface curves come into contact an initial contact radius is formed as a function of the van der Waal's pressure and any potential loading force F_l that may arise whether it is electrostatic, mechanical force or capillary forces, according to the equations:

$$a = \left(\frac{R}{K}\right)^{1/3}\left(\tau\sqrt{\frac{3}{2}\pi R\gamma_w} \pm \sqrt{\left(2-\frac{\tau^2}{2}\right)\pi R\gamma_w}\right)^{2/3} \quad \text{(m)} \qquad (3.20)$$

$$\sigma(r) = \frac{3Ka}{2\pi R}\sqrt{1-\left(\frac{r}{a}\right)^2} - \tau\frac{\sqrt{\frac{3K\gamma_w}{2\pi a}}}{\sqrt{1-\left(\frac{r}{a}\right)^2}} \quad (\text{Nm}^{-2}) \qquad (3.21).$$

It has been deduced already that the primary and constant force is the van der Waal's force incorporated into the work of adhesion γ_w and F_l (the external loading force) is treated as being negligible to simplify the analysis.

After initial contact, given a temperature T<1323K, previous researchers generally agree that surface diffusion will drive the sintering process[13, 67]. Sintered necks will continue to grow in this way based on surface diffusion up to 100 hours or more before other mechanisms such as volume diffusion become dominant[13, 69]. Since defluidisation occurs within 30-90 minutes after metallisation begins,[5] it is reasonable to focus more closely on surface diffusion after initial contact as the primary adhesion mechanism.

6.2.1. van der Waal's forces and adhesion

In Chapter 3, the van der Waal's constant (A) was obtained experimentally, and the work of adhesion (γ_w) was derived from the contact curve in the atomic force microscope. The contact mechanics theory used and described in chapter 3 is applicable for ideal elastic contacts and can be extended to approximate the situation where there is plastic deformation at particle contacts.

The adhesion contact radius, adhesion pressures and surface sintering rates calculated for various sized iron particles were done using a MATLAB© program written for this study called "sinterFe", based on the theoretical framework laid out in the previous chapters. This code with a full explanation and references are outlined in **appendix 2**.

Prior to constructing sintering diagrams, it is important to compare how well the theory "approximates" the true situation of two iron spheres in contact or an iron sphere in contact with a flat surface. The geometry that is being modeled here is that shown in **figure 2.14** or **3.19.** To make this comparison, some SEM and TEM microscope images made by Easterling, Tholen and Yao [89, 125, 126]were examined. Across various papers these writers produced agglomerates of iron particles from 10-100 nm in radius at 25°C, 800°C and 900°C. Samples at high temperatures were sintered for 60 minutes. In these pictures, the agglomeration neck radius can be clearly seen in **figure 6.3a-e**.

The images in **figure 6.3a-e** were carefully analysed and some sample neck and particle radii were determined. These values are presented in **table 6.1**. It should be explained that the initial neck radius created due to elastic deformation of the particle was used to determine the adhesive pressure. After this is measured, the approximate plastic deformation neck radius is calculated, all according the equations presented in **Appendix 2**. The radius R of the particle in **table 6.1** is the radius of the smaller particle in contact with a larger particle or a flat surface, a_e and a_p is the elastic and plastic radius of contact respectively. In addition, σ_{max} and σ_{mean} are the maximum and the mean adhesive pressures across a given radius of contact respectively.

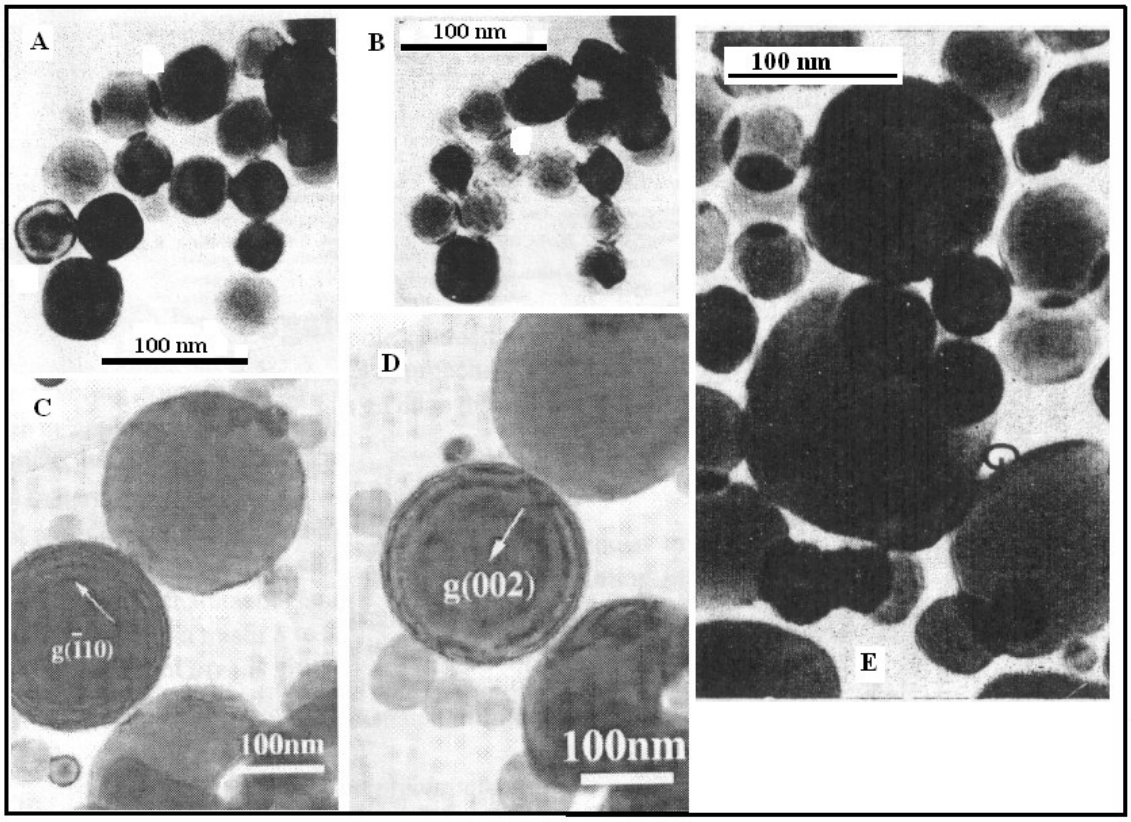

Figure 6.3a-d: Samples of spherical iron particles. **a)** Particles agglomerated at room temperature in the range of 10-30nm in radius. **b)** Particles of radius 10-30nm sintered at 800°C for 60 minutes. **c-d)** Particles of radius 100 nm at room temperature. **e)** Particles of radius 50-70 nm sintered at 900°C for 60 minutes.

Table 6.1: Values of the neck to particle radius ratio and the adhesive pressures. In the case of the experimental values at room temperature a value is noted in brackets which is the value taking surface diffusion into account. [a] Theoretical value if only elastic deformation occurs. [b] Theoretical value if plastic deformation occurs. [c] Experimental values (after Easterling and Tholen[89, 125, 126]). [d] Experimental values derived from AFM adhesion curves.

T (°C)	R (nm)	a_e/R^a	a_p/R^b	a/R^c	a/R^d	σ_{max} (GNm^{-2})	σ_{mean} (GNm^{-2})
25	11.21	0.04	0.160(0.37)	0.57	--	3.6138	2.7122
25	50.00	0.0292	0.074(0.12)	0.12	--	2.1061	1.5120
25	100	0.0247	0.072(0.11)	0.25	0.37	1.7491	1.2285
25	3000	0.0102	0.010(0.02)	--	0.07	5.8577	3.0616
800	9.37	0.0809	0.62	0.71	--	1.7010	1.2058
900	58.00	0.060	0.30	0.48	--	2.1997	1.5864
800	100	0.0421	0.239	--	--	0.7848	0.4800
800	3000	0.0170	0.050	--	--	0.2665	0.1197

When the experimental values of neck to particle radius are compared to the theoretical values there is an agreement under some conditions and not others. The Schwarz theory of contact mechanics used to model contact behaviour in this study, makes the assumption that the surfaces in contact are smooth and continuous smooth and atomistic. This assumption is not realistic as has been shown in the literature and is only an approximation to real surfaces[124].

In the case of the agglomerated particle at room temperature the theory predicts a value of the neck to particle radius less than that measured in the electron micrographs. The value for the larger particle is closer to the theoretical value. This is expected as sintering is thought to take place at lower temperatures for smaller particles[89], causing the neck to appear larger than would be expected by van der Waal's adhesion alone.

The experimentally derived values of the ratio of neck radius to particle radius from AFM data show a similar deviation from the theory. In the case of the 0.1 and 3 μm spheres the experimental values are both about 7 times larger than the theoretical prediction.

At higher temperatures of 800-900°C the theory will also predict a lower value for the ratio of neck to particle radius.

In any event the theory seems likely to predict values that are lower than the experimental values. If surface sintering is taken into account the values are closer to the observed values (values in brackets in **table 6.1**).

The adhesion stress in all cases is well above the tensile and plastic yield stress for iron and so plastic deformation is taken into account. The plastic deformation neck radius is approximated with an equation by Johnson[127] (see **appendix 2**). A histogram of the distribution of values for the adhesion stress across a contact shows a heavy skew of values near the maximum adhesion stress at the centre of contact. Approximately 65% of values are within one standard deviation of the maximum value and the mean value is within this range. The mean adhesion stresses for these particles can thus be taken as a sensible conservative estimate of the overall adhesion stress. It remains to be said so far as to what the significance is of adhesion stresses of this magnitude. To answer this, take as an example an iron ore particle that is undergoing nucleation of pure iron on its surface similar to the case in **figure 6.1**. Supposing that this particle were to make contact with another iron particle and they intermesh with each other, what then would the adhesive stress be for the whole particle?

The average tip radii for these nuclei is between 10-20 nm as a conservative estimate. The surface density of nuclei at this early stage of reduction is approximately one nuclei for every square micron of surface with a tip radius of say 20 nm. Taking into account the adhesion stress of each nuclei contact which is $\sim 10^{3}$ Nm^{-2} or 10^{-3} N/mm^{2}. This can be thought of as a typical lower estimate of the adhesion stress if only van der Waal's forces were involved.

In order to find a tangible comparison to this adhesion stress, we can consider the adhesion strength of the Tokay Gecko. The Tokay Gecko uses van der Waal's forces to climb up vertical surfaces and to suspend its weight on a ceiling directly under gravity. On average, it will apply approximately 40 Nmm^{-2} through all four foot-pads to support

a weight of ~15 – 50g[61] (see **figure 6.4**). Essentially the Tokay Gecko will exert 1-3 Nmm^{-2} for every gram of body weight ($Nmm^{-2}g^{-1}$).

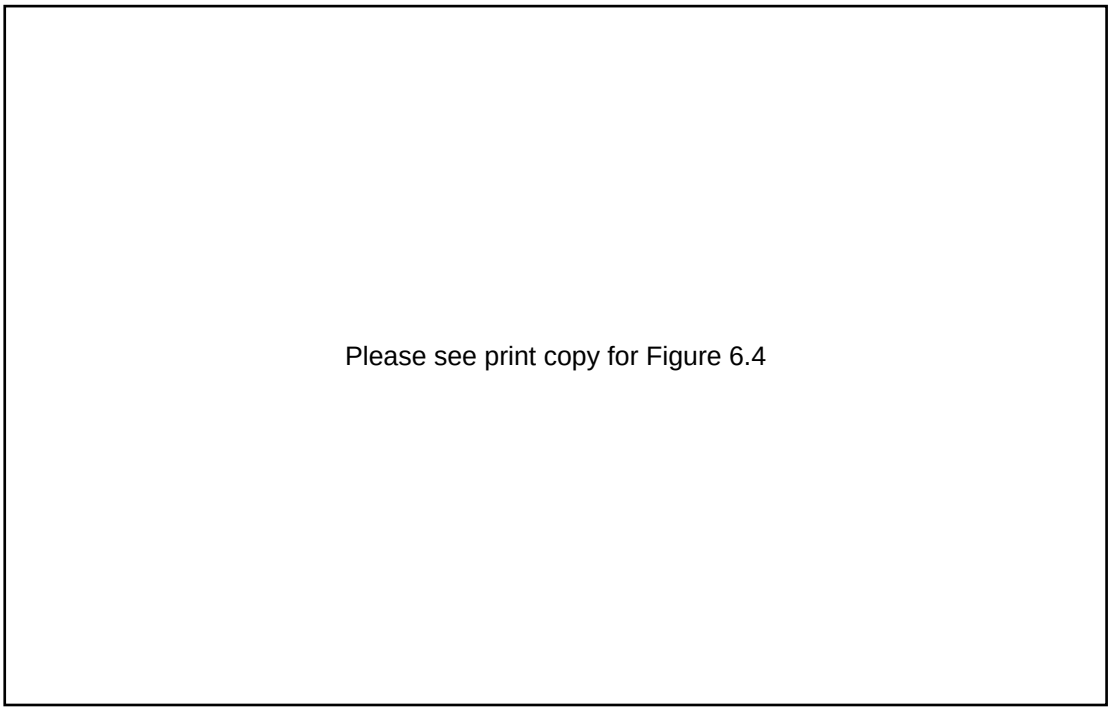

Figure 6.4: Adhesive stress of 40 Nmm^{-2} across all four footpads to support its body weight of 15 – 50 grams (after Autumn, K., et al., *Adhesive force of a single gecko foot-hair.* Nature, 2000. 405: p. 681)

A typical metallised iron particle will have a mass between ~10^{-8} – 10^{-5} g. The stress mentioned above supporting this weight translates to 10^{2} – 10^{5} $Nmm^{-2}g^{-1}$. Clearly adhesion to the walls of an iron ore reactor can be accomplished by van der Waal's adhesion. Finer particles being of lesser mass are thus more susceptible to sticking by the van der Waal's mechanism.

6.2.2. Surface sintering and temperature effects

The mechanism of van der Waal's adhesion is of course not the only mechanism involved in achieving adhesion in an iron ore fluidised bed. Surface sintering and temperature effects also come into play.

Surface diffusion coefficients for pure iron determined using confocal microscopy in chapter 4 and adhesion values from van der Waal's forces determined in chapter 3 were combined to create simplified sintering diagrams. The values for the diagrams were calculated using the computer program *sinterFe*. Four diagrams for four particle radii were constructed for pure iron as shown in **figures 6.5a-d**.

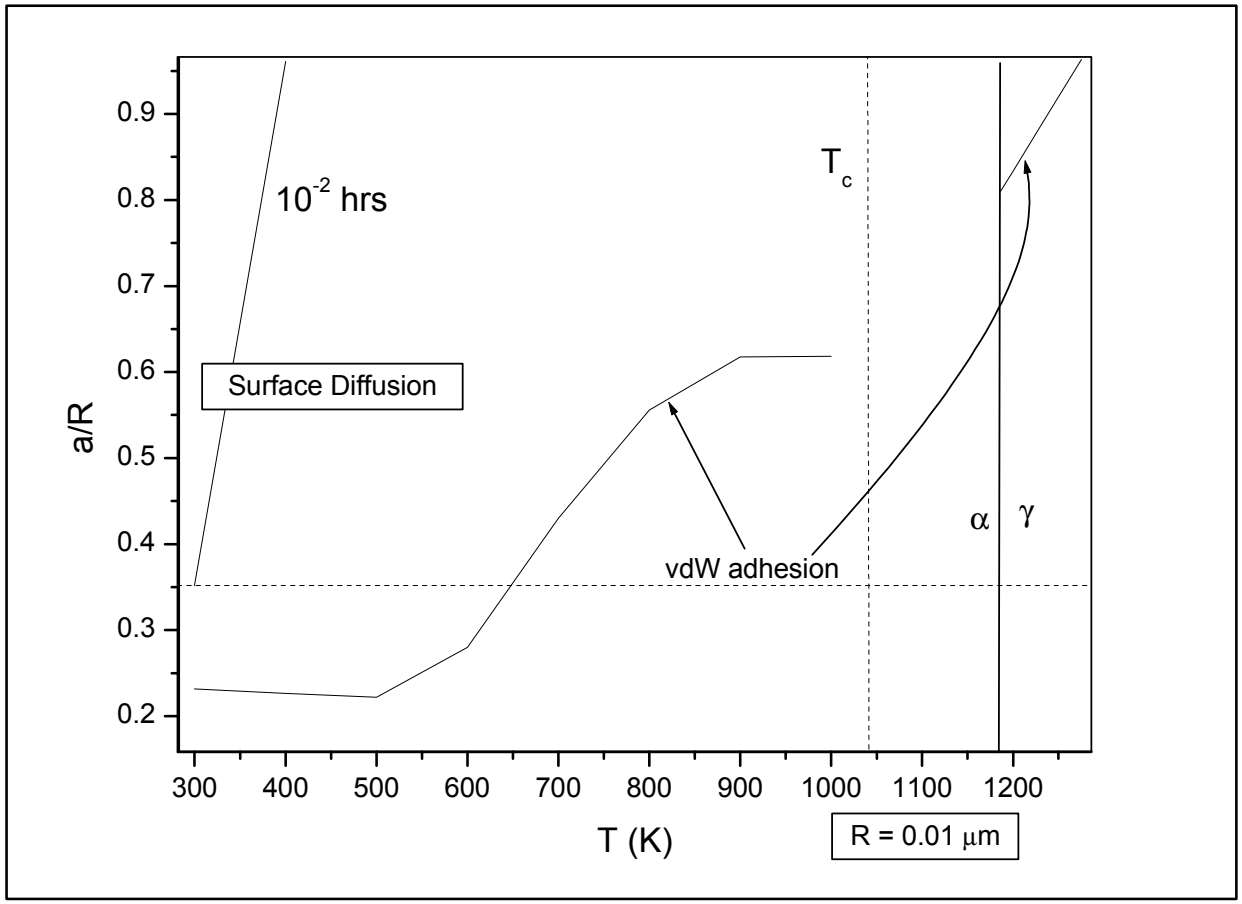
0.9
0.8
0.7
0.6
0.5
0.4
0.3
0.2
a/R
10^{-2} hrs
T_c
Surface Diffusion
vdW adhesion
α
γ
300
400
500
600
700
800
900
1000
1100
1200
T (K)
R = 0.01 μm

(a)

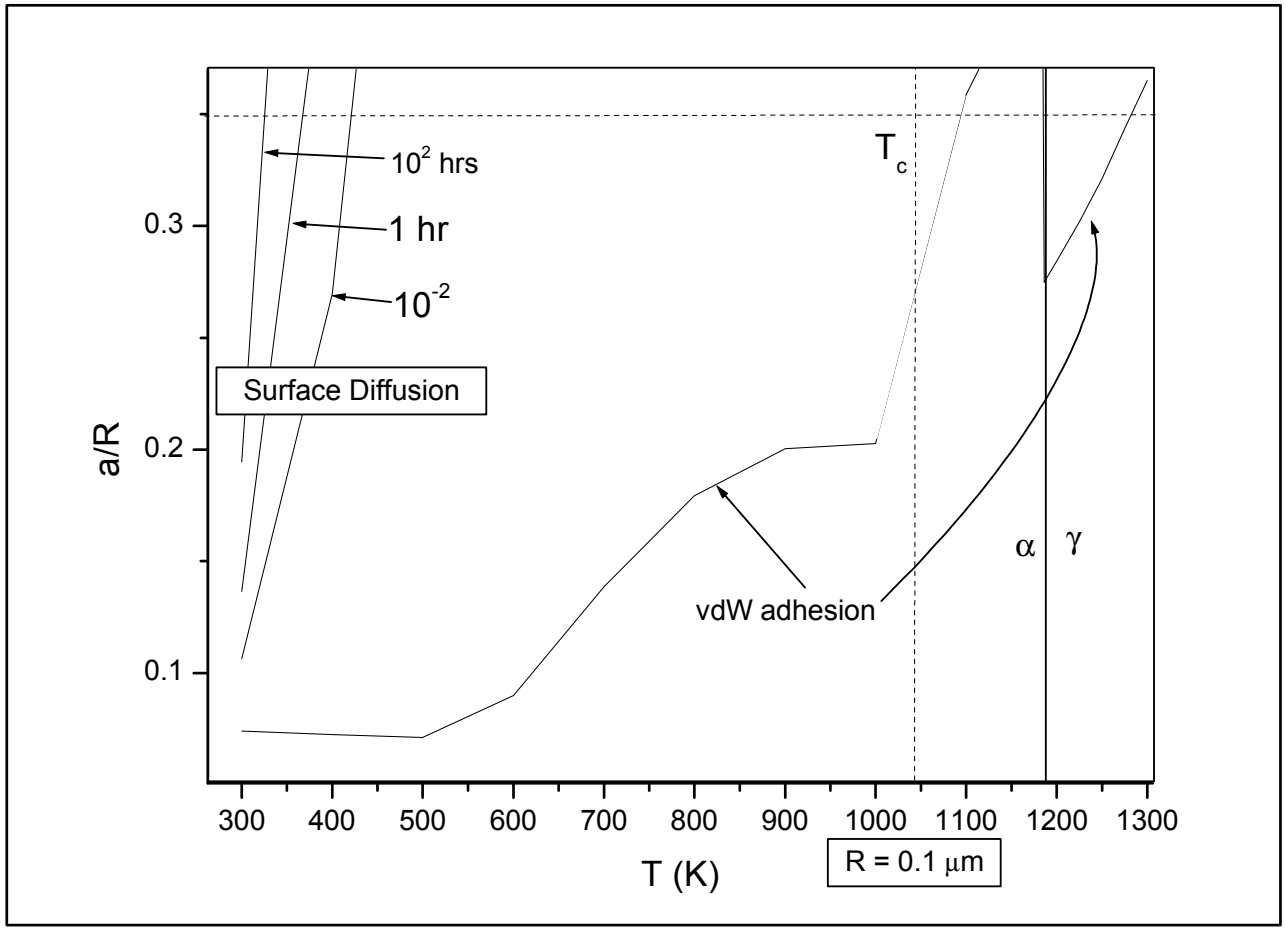
10^2 hrs
1 hr
10^{-2}
Surface Diffusion
T_c
vdW adhesion
α
γ
a/R
0.1
0.2
0.3
300
400
500
600
700
800
900
1000
1100
1200
1300
T (K)
R = 0.1 μm

(b)

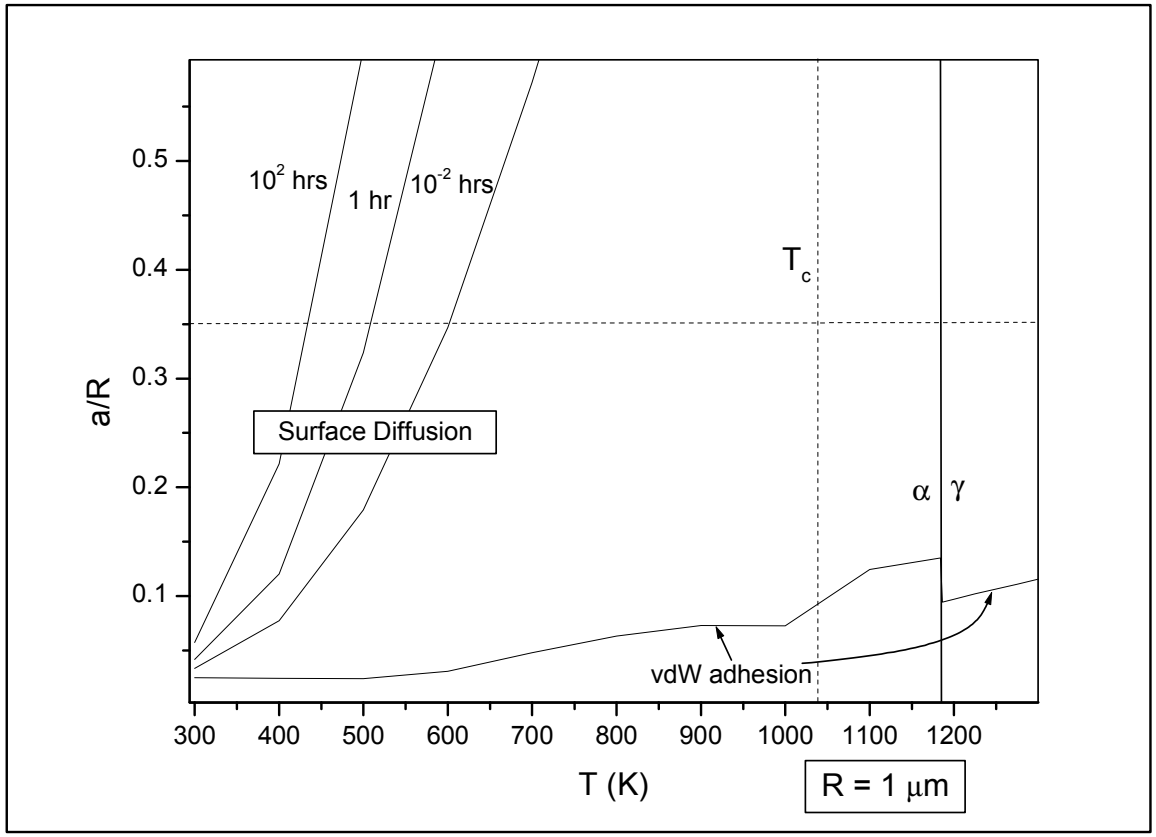
0.5
0.4
0.3
0.2
0.1
a/R
10^2 hrs
1 hr
10^{-2} hrs
T_c
Surface Diffusion
α
γ
vdW adhesion
300
400
500
600
700
800
900
1000
1100
1200
T (K)
R = 1 μm

(c)

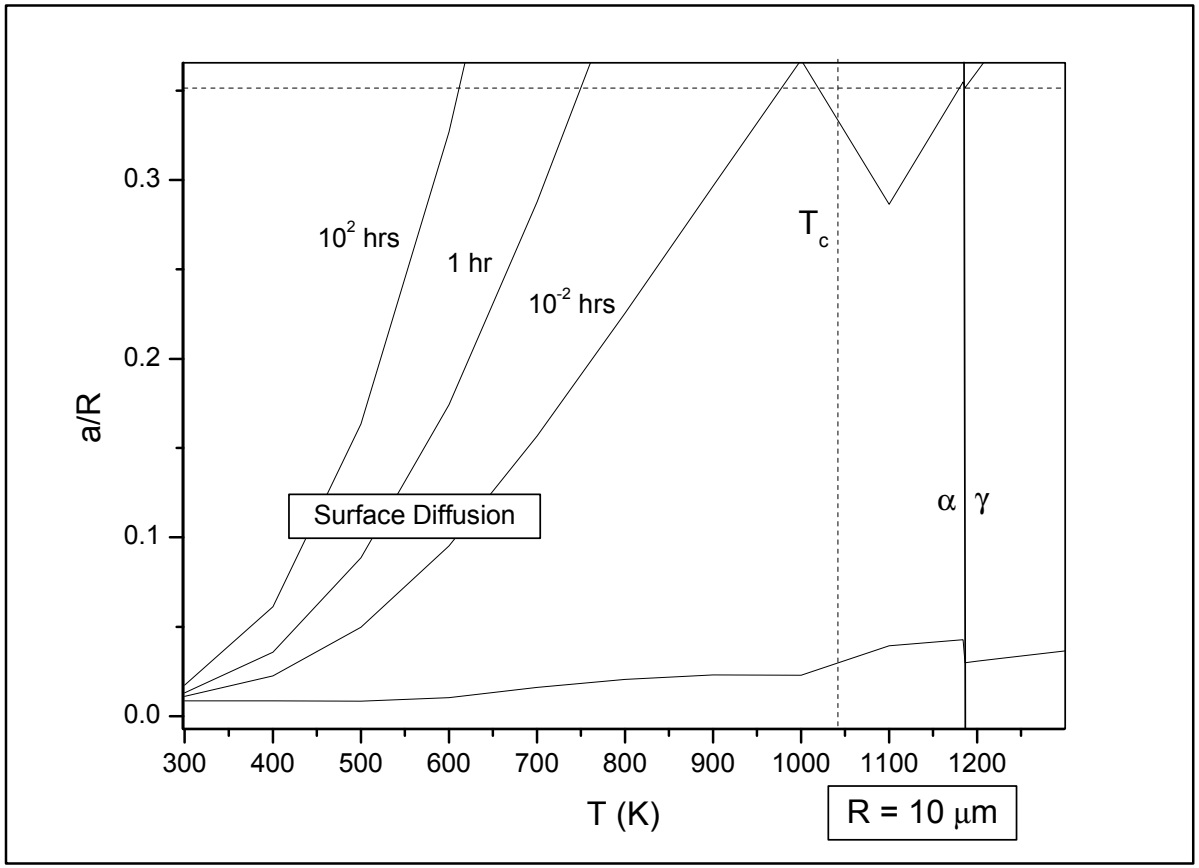
0.3
0.2
0.1
0.0
a/R
10^2 hrs
1 hr
10^{-2} hrs
T_c
Surface Diffusion
α γ
300 400 500 600 700 800 900 1000 1100 1200
T (K)
R = 10 μm

(d)

Figure 6.5a-b: Sintering diagrams for the neck radius relative to the particle or contact radius involving adhesion and surface diffusion with respect to temperature. The adhesion line is regarded as resulting from instantaneous contact at the particular temperature. **a)** R = 10 nm **b)** R = 100nm **c)** R = 1 micron **d)** R = 10 microns.

The sintering diagrams above show a general picture of neck formation by sintering via the mechanisms of surface diffusion and van der Waal's adhesion. The contact neck sizes can refer to a surface radius of curvature or a particle of a given radius. The adhesion line on all four of the graphs has been constructed using specific mechanical properties of iron at the given temperature. Neck radius is an important quantity for sintering as it provides the conduit for atomic transport leading to particle cohesion.

There is considerable detail in the sintering diagrams in **figure 6.5** and so it is worth taking the time to deconstruct them. The y-axis on the left of the diagram is indicating the ratio of the contact neck radius to the particle radius expressed as *a/R*. Along the x-axis on the bottom is the temperature (Kelvin) the particle and surface are at when they come into contact. The size of *a/R* due to van der Waal's forces alone is shown as a function of temperature. The other quantity shown on the graph is the resulting *a/R* due to surface diffusion after the particles are in contact for a certain time. The lines are labelled surface diffusion and the length of contact time is indicated on each line. All four diagrams show the Curie temperature (T_c) and the alpha-gamma phase boundary. On the bottom right of the diagrams, the particle size is indicated.

Previous authors have not typically considered that neck formation via adhesion to change significantly as temperatures are raised[68, 69, 128]. This approximation is justified for a spherical particle of a large radius say R > 10 microns. It has also been assumed that surface diffusion is the dominant sintering mechanism for temperatures

below about 1373 K[13, 67]. This is also a justified assumption for larger particles. When the particle, or radius of contact is much smaller, the situation changes.

The diagrams in **figure 6.5a-d** show a trend of surface diffusion lines pulling back towards the left and so surface diffusion is minimal past certain temperatures. It is noted by authors that surface diffusion if present will contribute greatly to the broadening of neck sizes and that other mechanisms of sintering such as volume diffusion will contribute more to neck densification after surface diffusion becomes less dominant[67-69]. The adhesion line rises with higher temperatures as the particle size gets smaller. In the cases of the 10nm and 100nm diagrams surface diffusion is rapid at lower temperatures and seems to give way to van der Waal's adhesion at higher temperatures. There is some direct evidence that neck formation via surface diffusion is possible at room temperature. Investigations in gold contacts shows rapid surface movements of atoms surrounding a particle radius of curvature of 5-10nm[60]. Whatever the case may be at room temperature, neck growth seems dependent on the adhesion properties rather than by surface diffusion at higher temperatures.

In the case of the iron spheres mentioned in section 6.2.1, spheres in the size range 10-50 nm were sintered at 800 °C and some at 900 °C for a period of 60 minutes. The necks did not grow in size during this period much beyond that which is predicted for van der Waal's adhesion. However, what was observed for particles in contact was a shrinking in the distance between two particle centres. This implies a densification of the bulk material via volume diffusion[125]. Thus, in the case of smaller particles or smaller radii of curvature contacts at high temperature, the neck size is largely dictated

by the adhesion properties of the iron. In the case of larger particles, surface diffusion is more predominant and adhesion by van der Waal's forces makes less of a contribution.

6.2.3. The effect of temperature

The sintering diagrams above are constructed for pure iron[129]. In any practical instance a specimen of iron is unlikely to be pure. It is generally accepted that a tolerance of 0.02-0.05 percent by weight of carbon be accepted for mechanical testing of steels. Specimens with 0.02 percent by weight of impurities are considered in the range of ferrite. Samples of "pure" iron created by POSCO Technical Research Laboratories were made for mechanical testing in the Wollongong University mechanical testing laboratory. These samples had carbon contents in the range of 0.02 – 0.05[130]. The point being made here is that any reported mechanical properties of pure iron are only very nearly pure at best.

This distinction is important as the van der Waal's adhesion values for the neck radius are highly dependent on the mechanical properties of the material. The equations used to calculate the van der Waal's adhesion line in these diagrams are dependent on the physical data inputted. According to this data a transition occurs at 1043K where the plastic yield strength is considerably lower. This temperature happens to be the Curie temperature where the ferromagnetic material loses its permanent magnetic properties and becomes paramagnetic[88]. There is in fact not reason to believe that such a dramatic change in yield strength should be linked to the Curie temperature. The implication here is that the change in yield strength is connected to the change from the α to the $\alpha + \gamma$ region according to **figure 2.4**.

The sintering diagrams are calculated for the situation of two spherical particles of the same radius. They can be calculated for a particle sticking to a flat surface according to the program in **appendix 2**. In the case of larger particles in **figure 6.5c-d** the difference between particle adhering to a similar sized particle or to a flat surface makes little difference. In the case of the particles in **figure 6.5a-b** the particle adhesion is much higher. To take an example, for particles of 100 nm in radius at T = 1043K sticking to a flat surface, $a_p/R \sim 0.33$. If the particles are comparable in size the value is more like $a_p/R \sim 0.24$. In the case of particles of 10 nm in radius at T = 1043K sticking to a particle comparable in size, $a_p/R \sim 0.71$. If the particle is sticking to a flat surface the value of a_p/R from 1043K to 1185K is singular, meaning that the material is soft enough and the pressure is high enough at this point to forge to the surface completely.

There is another striking effect of temperature when it comes to adhesion. The results in chapter five show quantitatively that a transition in a sticking stress occurs at the eutectoid line and that from an analysis of Dilatometre experiments and visual analysis of samples that the test material used was equivalent to a 0.6-1 percent by weight carbon steel. This transition in sticking properties across the eutectoid temperature was also observed at New Castle laboratories in powdered samples. Why then should this be the case?

Visual analysis of the carbon steel samples having been quenched from 750°C and 800°C shows that they are of a partial martensite composition for 750°C and a full martensite composition for 800°C. When at temperature these samples were mostly transformed to the FCC structure by 750°C and completely transformed by 800°C. The diagram in **figure 6.6a** shows that the transition to the higher degree of sticking has

taken place by ~730°C and dips slightly by ~770°C onwards. In general, the yield properties of metals in the BCC structure are much higher than their corresponding FCC structure[119] and the degree of difference will vary depending on the purity and grain structure. It is argued here therefore that the change in sticking quantities across this temperature is due the lowering in the hardness of the material thus creating a wider interface for further sintering.

6.2.4. The effects of carbon content

A higher carbon content in iron, tends to have a direct effect on the physical properties of a material, which in turn appears to affect the sticking properties. The two main properties affected by carbon content are the mechanical and the transport properties of the material. The main quantities of these properties were outlined in chapters 4 and 5 and here some important comparisons will be made from the data.

In the beginning of this study an aim was identified to compare products of the reactors that contained ~0.5-1 % by weight of carbon and 1.5 % by weight. It was shown in chapter 5 that Fe-1.0C steel contained more martensite than the Fe-1.5C steel. Fe-1.5C steel was richer in cementite and that it revealed a higher Vickers hardness overall. It is a generally recognised property that the hardness of carbon steel will reduce with increasing carbon content and also be reduced with increasing temperature[131]. When the basic sticking quantities are compared they show that the Fe-1.5C sticking is lower (see **figure 6.6**) and that this trend compares well to the qualitative test carried out at BHP-Billiton (see **figure 6.6a-b**).

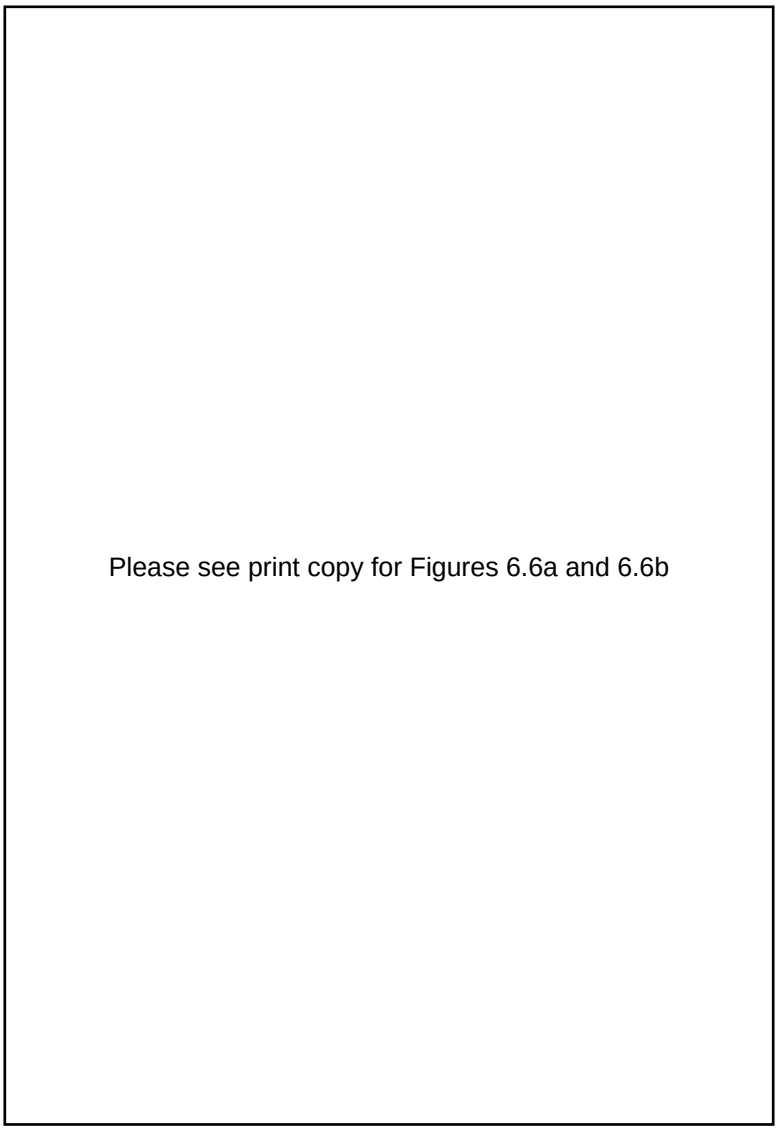

Figure 6.6b: Qualitative sticking test courtesy of BHP-Billiton.

The carbon content does have some affect on the surface diffusion properties. Referring to **figure 6.7** the overall trend in surface diffusion coefficient with respect to carbon

content is shown. Choosing a reference temperature of 1100°C, pure iron, 0.5-1.0 and 1.5 % by weight carbon steel are all in the γ-phase.

Moving from left to right it can be seen from **figure 6.7** that the surface diffusion rates do not deviate from the pure iron to 0.4 % by weight carbon steel. However, at 0.9 % carbon the surface diffusion rate drops nearly two orders of magnitude and this rate continues on until 1.5 % carbon steel. Thus in terms of how surface diffusion rates affect inter-particle neck growth, there is a significant difference between pure iron and high carbon steels. However the difference in surface diffusion between carbon steels of 0.9 and 1.5 % carbon is negligible.

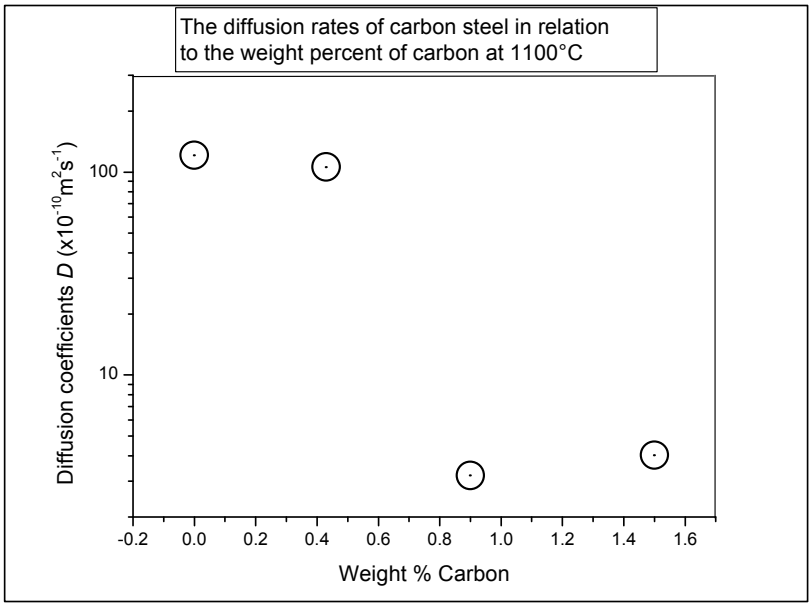

Figure 6.7: The change in the surface diffusion rate as the carbon content of the iron is increased.

Chapter 7:

Summary and general conclusions

Chapter 7: Summary and general conclusions

A background study into the field of the agglomeration of iron ore particles inside a fluidised bed reactor, leading to defluidisation, has revealed a long history and many studies into understanding this issue. The literature search has proven useful in constructing a novel starting point for the present study. In the past, most studies into this problem have been plant based or laboratory simulations especially with work conducted at BHP-Billiton. This has proven to be an invaluable source of data in giving direction to this study. However, the present study has taken a less traditional approach to the problem and has sought to understand some fundamental physics and thus quantify the phenomena of sticking of iron ore particles.

In summing up the various observations made in this study, it can be asserted that a number of fundamental properties of the sticking of iron ore particles have been uncovered.

The general mechanism of the agglomeration of fine iron ore particles is by sintering. A study of the sticking of iron ore particles has been conducted by delineating the sub-mechanisms involved in sintering such as van der Waal's adhesion and surface diffusion, and endeavouring to quantify these attributes for iron.

The basic adhesive properties of metals in general, prior to this study, had limited experimental quantification. The existence of work of adhesion values for metals was rare in the literature. The derivation of work of adhesion values, are important in estimating the adhesion stress and evaluating the size and extent of inter-particle contacts. In this study, van der Waal's forces and the work of adhesion for iron surfaces

in contact has been evaluated using atomic force microscopy. It was shown that the pressure exerted at a local infinitesimal point on one iron particle by another was higher than the yield stress of iron and probably leads to plastic deformation of the surface, giving rise to large contact areas between them. Inference from atomic force microscope adhesion curves lends support to this theory.

Surface diffusion values in iron had been well quantified prior to this study. In this study however, a new and more efficient technique of quantifying the surface diffusion rates in metals had been developed using confocal microscopy and ion beam milling. Surface diffusion rates in iron were measured and benchmarked against earlier quantities. The new quantities compared well with the old values, considering the difficulty involved in repeating surface diffusion experiments.

Carbon content in the Port Hedland reactor showed a correlation of sticking and carbon content in the metallised powders. Surface diffusion rates in pure iron and iron-carbon alloys were measured for comparison. It was found that quantities of carbon higher than 0.5%C led to a 100-fold decrease in surface diffusion rates. It is concluded that high carbon content will retard the transport of iron material to a contact site between two particles.

A high-temperature sticking test was developed in this study to test and quantify observations made at BHP-Billiton. It was found that in commercial carbon-steel conforming to a carbon content of approximately 0.8%C, a distinct difference exists between sticking quantities of contacts made below and above the eutectoid temperature. Sticking stress was observed to be higher above the eutectoid temperature

and it is inferred that the gamma phase of iron is highly susceptible to sticking. This is in contrast to the high carbon steel. It is shown here that Fe-1.5%C steel shows less potential to stick. Iron powders from port Hedland showing minimal sticking are covered in a thin layer of cementite. Thus, the low sticking strength of the high carbon steel is probably due to its content of cementite.

Sintering diagrams were constructed for iron to study the combined effect of surface diffusion and van der Waal's adhesion between iron particles. Two main insights were gained from this. Firstly, the potential to form interparticle contacts via van der Waal's adhesion were not constant with temperature and would vary according to the change in plastic yield strength. It was found that over all that inter-particle contacts grew larger with increasing temperature. Secondly, van der Waal's adhesive properties were more significant when operating on smaller sub-micron particle contacts. In larger particles, the formation of inter-particle contacts relies more of the rates of surface diffusion.

Particles found in iron ore reactors are typically rough on the surface and irregularly shaped. It is therefore likely that even though the overall radius of the particles is large, the true inter-particle contacts involve contact sites of low radius of curvature, that is, effectively similar to sub-micron particles. It is concluded therefore that van der Waal's forces play a ubiquitous significant role in the sintering of iron ore particles.

An entire understanding of the mechanisms involved in the cohesion of fine iron particles is by no means complete. There are still open questions on the role of electrostatics and magneto-statics in the adhesion characteristics of agglomeration. This

study however has been successful at identifying the key fundamental contributions to the sticking phenomena.

Appendix 1: Magnetic force field

The energy of a spherical dipole moment $\vec{m}_1$ magnetised by a magnetic flux density $\vec{B}$ in the proximity of another spherical dipole moment $\vec{m}_2$ is given by[88]

$$E = -\vec{m}_1 \bullet \vec{B} \qquad \text{(J)}. \tag{A1}$$

Thus the force is given by the energy gradient between them[132]

$$\vec{F} = \underset{\sim}{\nabla} E = -(\vec{m}_1 \bullet \underset{\sim}{\nabla})\vec{B} \qquad \text{(N)}. \tag{A2}$$

To calculate the flux density, consider a spherical magnet with a magnetic flux density $\left|\vec{B}\right|$ at a distant point *P* as in figure A1. The magnetic potential for the sphere is if r>>R:[132]

$$V_m = \frac{1}{4\pi}\frac{\vec{m} \bullet \vec{a}_r}{r^2} = \frac{1}{4\pi}\frac{m\vec{a}_z \bullet \vec{a}_r}{r^2} = \frac{1}{4\pi}\frac{m\vec{a}_z \bullet \vec{a}_r}{r^2} = \frac{1}{4\pi}\frac{m\cos\theta}{r^2} \qquad \text{(A)} \tag{A3}$$

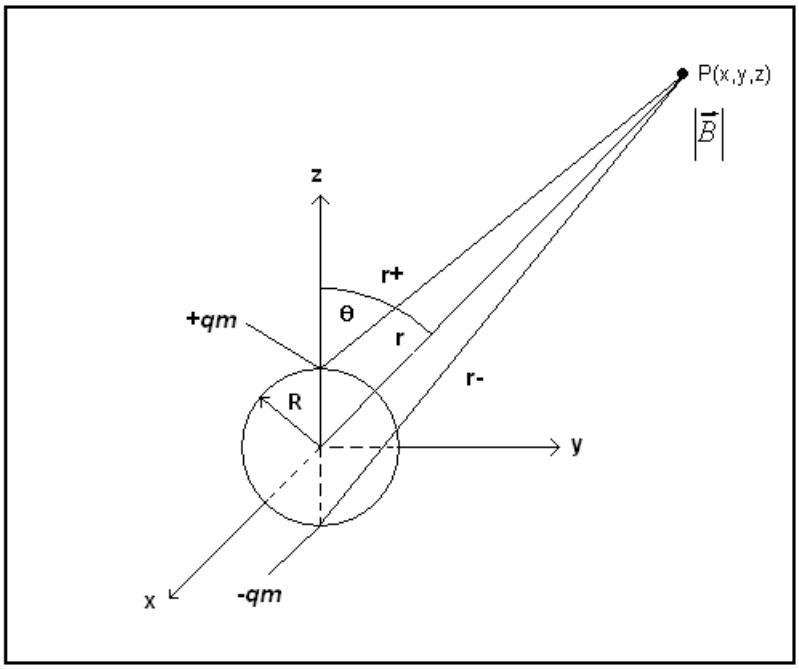

Figure A1: The magnetic flux density experienced at and arbitrary point P.

Where $m = MV$ and $\vec{M} = \vec{a}_z M$ is the magnetic dipole moment density and V is the volume of the sphere. It is simple then to show that the magnetic flux density at a given point is:

$$\vec{B} = \mu_0 \nabla V_m = \frac{\mu_0 m}{4\pi r^3}(\vec{a}_r 2\cos(\theta) + \vec{a}_\theta \sin(\theta)) . \qquad \text{(T)} \qquad \text{(A4)}$$

Assume that you want to find the flux density above the pole along the z-axis. Then $\theta =$ 0, $r = z$ equation 3 becomes:

$$\vec{B} = \vec{a}_z \frac{\mu_0 m}{2\pi z^3}$$

The force from equation (2) given that $\vec{m}_1 = \vec{a}_z m_1$ is then

$$\vec{F} = \underset{\sim}{\nabla} E = -(\vec{m}_1 \bullet \underset{\sim}{\nabla})\vec{B} = -m_1 \frac{\partial}{\partial z}\vec{B} = -\vec{a}_z m_1 \frac{\partial}{\partial z}\frac{\mu_0 m}{2\pi z^3} = \vec{a}_z m_1 m \frac{3\mu_0}{2\pi z^4} . \quad \text{If } m_1 = m = MV$$

and $M = \frac{1}{\mu_0} B$ and $V = \frac{4\pi R^3}{3}$ this makes the final value for the force

$$\vec{F} = \vec{a}_z \frac{8\pi}{3}\frac{B^2}{\mu_0}\frac{R^6}{z^4} \qquad \text{(N)} \qquad \text{(A5)}$$

Appendix 2: MATLAB™ program *SintrFe*

This appendix has the complete MATLAB© code for *sinterFe* which calculates the van der Waal's force and adhesion pressure, work of adhesion, equilibrium separation distance of two particles in contact, the contact neck radius and values to construct a sintering diagram by surface diffusion. It can calculate these numbers for any single atomic or binary alloy provided some empirical values are known. All steps are explained and references sited for values used in the pure iron system and for methods of calculation.

Please see print copy for Appendix 2

References

1. Brent, A., P. Mayfield, and T. Honeyands, *The Port Hedland FINMET Project - Fluid bed production of high quality virgin iron for the 21st century.* ICARISM, 1999. **99**: p. 111.
2. Whipp, R., *FIOR briquettes - now a reality.* AIME Electric Furnace Conference Proceedings, 1980. **38**: p. 46.
3. Shook, A. and T. Honeyands, *Solids transfer and sticking project*. 2000, BHP-Billiton: Minerals Research: Newcastle.
4. Crawford, D., P. Mayfield, and J. Truelove, *Preliminary Analysis of Causes for Metallisation Limitations in FINMET Process Trains 1 and 2 During Initial Commissioning Operations*. 1999, BHP-Billiton: Centre for Metallurgy and Resource Processing: Newcastle.
5. O'Dea, D., *Effect of MgO anti-Sticking Additives on FIOR and FINMET Fluidisation*. 1997, BHP-Billiton: Newcastle.
6. Gransden, J.F. and J.S. Sheasby, *The Sticking of iron ore during reduction by hydrogen in a fluidised bed.* Can. Metall., 1974. **13**: p. 649.
7. Nicolle, R. and A. Rist, *The Mechanism of Whisker Growth in Reduction.* Metall. Trans. B., 1979. **10B**: p. 429.
8. Fuller, D., *Sticking Phenomena on Fines Processing by Direct Reduction in a Fluidised Bed.* ILAFA, 1977.
9. Ezz, S.W., *Gaseous Reduction of Fine Ores in the Fluidised Bed Reduction.* J. Metals, 1960: p. 312.
10. Ezz, S., Trans. Metall. Soc., 1959. **48**: p. 709.
11. Gransden, J., J. Sheasby, and M. Bergougnou, *An investigation of defluidisation of iron ore during reduction by hydrogen in a fluidised bed.* Chem. Eng. Symp. Proc., 1970: p. 208.
12. Hayashi, S., S. Sayama, and Y. Iguchi, *Relation between sulphur pressure and sticking of fine iron ores in fluidised bed reduction.* ISIJ Int., 1990. **30**: p. 722.
13. Mikami, T., K. Hidehiro, and H. Masayuki, *The Mechanism of defluidisation of iron particles in a fluidised bed.* Powder Technology, 1997. **89**: p. 231.
14. Haas, H.d. and e. al, *Reflections on the mechanism of the oriented iron growth in reduction of iron ores by means of CO gases.* Arch. Eisenhuttenwes, 1980. **51**: p. 167.
15. Neuschutz, D., *Sticking prevention during fine ore metallisation in two stage smelting reduction processes.* Steel Res, 1991. **62**: p. 333.
16. Conejo, A.N. and G.P. Martins, *Conversion of Hematite to Iron Carbides by Gas Phase Carbidisation.* ISIJ Int., 1997. **37**: p. 967.
17. Wong, P., et al., *Sticking Behaviour in Direct Reduction of Iron Ore.* Iron and Steelmaking, 1999. **26**: p. 53.
18. Nascimento, R.C., M.B. Mourao, and J.D.T. Capocchi, *Microstructures of Self-reducing processes.* ISIJ Int, 1997. **37**: p. 1050.
19. Matthew, S. and P. Hayes, *Microstructural Changes occurring during the gaseous reduction of magnetite.* 1989.
20. Kopfle, J., *The History of Direct Reduced Iron*, in *Direct Reduced Iron*, J. Feinman and D.M. Rae, Editors. 1999, The Iron & Steel Society. p. 99.
21. MIDREX, MIDREX.

22. Panigrahi, R., *Direct reduction processes*, in *Direct Reduced Iron*, J. Feinman and D. MacRae, Editors. 1999, ISS Society.
23. Chatterjee, A., *Beyond the Blast Furnace*. 1994: CRC. 224.
24. Stephenson, R., ed. *Direct Reduced Iron- Technology and Economics of Production of Use*. 1980, Iron and Steel Society: Warrendale, P.A.
25. Dippenaar, R., *Report on Stickiness Encountered in HBI Production*. 2000, BHP Institute for Steel Processing and Products: Wollongong.
26. Melfo, W., *Early Sintering Phenomena Pertaining to Hot Briquetted Iron*, in *BHP Institute for Steel Processing and Products*. 2002, University of Wollongong: Wollongong. p. 100.
27. Chipman, T., *Thermodynamics of phase diagrams of the Fe-C System.* Metall. Trans., 1972. **3**: p. 58.
28. Porter, D.A. and K.E. Easterling, *Phase Transitions in Metals and Alloys*. Second Edition ed. 1992: Chapman and Hill.
29. Pelton, D. and C. Bale, *Thermodynamics*, in *Direct Reduced iron*, J. Feinman and D. MacRae, Editors. 1999, Iron & Steel Society. p. 25.
30. Turkdogon, E., *Fundamentals of Steelmaking*. 1996, London: The Institute of Materials. 57-62.
31. Wagner, C., *Diffusion and High Temperature Oxidation*, in *Atom Movements*. 1951, ASM: Cleveland. p. 153.
32. Janssen, P., *Effect of Carbon and Sulphur of the sticking behaviour of the fine ores during metallisation in the fluidised bed*, in *Aachen*. 1994. p. 1-106.
33. Hayashi, S. and Y. Iguchi, *Production of Iron Carbide from Iron Ores in a Fluidised Bed.* ISIJ Int., 1998. **38**: p. 1053.
34. Ghosh, D., A. Roy, and A. Ghosh, *Reduction of Ferric Oxides with Methane.* Trans. ISIJ, 1986. **26**: p. 186.
35. Zhang, J. and O. Ostrovski, *Iron Ore Reduction and Iron Carburisation by H-Ch-Ar Gas.* Belton Symp. Proc., 2000: p. 431.
36. Sinha, A., *Ferrous Physical Metallurgy*. 1989: Butterworks.
37. Huebler, J., *Gas reactions in reduction processes*, in *Iron ore reduction proceedings of a symposium of the electrothermics and metallurgy division of the electrochemical society*, R. Rodgers, Editor. 1962, Pergamon Press: Chicago.
38. Lu, W.-K., *Kinetics and Mechanisms of Heterogeneous Reactions*, in *Advanced Physical Chemistry for Process Metallurgy*, N. Sano, W.-K. Lu, and P. Riboud, Editors. 1997, Academic Press: New York. p. 217-247.
39. Lu, W.-K., *Kinetics and mechanisms in direct reduced iron*, in *Direct Reduced Iron*, J. Feinman and D. MacRae, Editors. 1999, Iron and Steel Society: Warrendale, PA. p. 43-57.
40. Wagner, C., *Mechanisms of the Reduction of Oxides and Sulphides to Metals.* Trans. Metals, 1952. **4**: p. 214.
41. Bahgat, M., et al., *The effect of grain boundaries on iron nucleation during wustite reduction process.* ISIJ International, 2004. **44**(12): p. 2023-2028.
42. CHANG, M. and L.C.D. JONGHE, *Whisker growth in reduction of oxides.* Trans Metall B, 1884. **15B**: p. 685.
43. Joseph, T., Trans. AIME, 1936. **120**: p. 72.
44. Yang, J.-J. and W.-K. Lu, *Comparative studies of commercial iron ore pellets.* ISS-AIME., 1985. **44**: p. 111.
45. Hayashi, S. and Y. Iguchi, *Factors Affecting the Sticking of Fine Iron Ores During Fluidised Bed Reduction.* ISIJ Inter., 1992. **32**: p. 962.

46. Lu, W.-K., *Observation of whisker growth during iron ore reduction.* Scand. J. Metall., 1977. **2**: p. 273.
47. Neuschutz, P. and T. Hasler, *Concept and present state of a coal-based reduction process for iron ore fines.* Steal. Res., 1989. **60**: p. 113.
48. Grebe, K., *Swelling behaviour of roasted iron ore pellets with variable gangue volume and gangue composition.* Stalh. Eisen., 1973. **93**: p. 472.
49. Nakibogly, F., *The gaseous reduction of solid calcio-wutites in carbon dioxide/carbon monoxide ratios and hydrogen/water gas mixtures.* Trans. Metall., 1986. **17B**: p. 375.
50. Gudenau, H., H. Eisen, and Y. Qi, Stalh. Eisen, 1991. **111**: p. 35.
51. Hayashi, S., S. Jawai, and Y. Iguchi, ISIJ, 1993. **33**: p. 1078.
52. Fredrickson, H. and I. Svensson, *On the Mechanism of Catastrophic Swelling of Cold-Bonded Pellets.* Scand. Metall., 1974. **3**: p. 185.
53. Honeyands, T., *Item 3.3: Statistical Validation of Surface Iron Morphology*. 2002, BHP-Billiton: Newcastle.
54. Guardiola, J., G. Ramos, and A. Romero, *Electrostatic behaviour in binary dielectric/conductor fluidised beds.* Powder Technology, 1992. **73**: p. 11.
55. Collinson, D., *Instruments and techniques in palaeomagnetism and rock magnetism.* Rev. Geophys. Space Phys., 1975. **13**: p. 659.
56. Neel, L., *Some theoretical aspects of rock magnetism.* Advanc. Phys., 1955. **4**: p. 191.
57. Runcorn, S., *Rock Magnetism: Geophysical aspects.* Adv. Phys., 1955. **4**: p. 245.
58. Hays, D., *Role of Electrostatics in Adhesion*, in *Fundamentals of Adhesion*, L.-H. Lee, Editor. 1991, Plenum: New York. p. 249-278.
59. Isrealachvili, J., *Intermolecular and surface forces*. Second Edition ed. 1995, USA: Academic Press. 205-207.
60. Erts, D., et al., *Force interactions and adhesion of gold contacts using a combined atomic force microscope and transmission electron microscope.* Appl. Surf. Sci., 2002. **188**: p. 460.
61. Autumn, K., et al., *Adhesive force of a single gecko foot-hair.* Nature, 2000. **405**: p. 681.
62. Iwadate, Y. and M. Horio, *Prediction of agglomerates sizes in bubbling fluidized beds of group C powders.* Powder Technology, 1998. **100**: p. 223.
63. Kuwagi, K., T. Mikami, and M. Horio, *Numerical simulation of metallic solid bridging particles in a fluidized bed at high temperature.* Powder Technology, 2000. **109**: p. 27.
64. Kuczynski, G., *Self-diffusion in sintering of metallic powders.* Trans. Am. Inst. Min. (Metal.) Engrs., 1949. **185**: p. 169.
65. Coblenz, W.S., et al., *Initial stage solid state sintering Models. A critical analysis and Assessment.* Proceedings of the 5th International Conference on Sintering and Related Phenomena, 1979: p. 141.
66. Pejovnik, S. and M. Ristic, eds. *Recent developments in the theoretical analysis of solid state sintering*. Material Science Monographs. Vol. 14. 1982, Elsevier: Amsterdam.
67. Matsumura, G., *Sintering of Iron Wires.* Acta. Metall., 1971. **19**: p. 851.
68. Ashby, M., *A first report on sintering diagrams.* acta. Metall., 1974. **22**: p. 275.
69. Swinkels, F. and M. Ashby, *A Second Report on Sintering Diagrams.* Acta. Metall., 1981. **29**: p. 259.
70. Ducker, W.A., T.J. Senden, and R.M. Pashley, *Direct measurement of colloidal forces using an atomic force microscope.* Nature, 1991. **353**: p. 239-241.

71. Biggs, S. and P. Mulvaney, *Measurement of forces between gold surfaces in water by atomic force microscopy.* J. Chem. Phys., 1994. **100**: p. 8501-8505.
72. Ducker, W.A. and T.J. Senden, *Measurement of forces in liquids using a force microscope.* Langmuir, 1992. **8**: p. 1831-1836.
73. Hao, H.W., A.M. Baro, and J.J. Saenz, *Electrostatic and contact forces in force microscopy.* J. Vac. Sci. Technol. B., 1991. **9**: p. 1323-1328.
74. Gotzinger, M. and W. Peukert, *Dispersive forces of particle-surface interactions: direct AFM measurements and modelling.* Powder Technology, 2003. **130**: p. 102-109.
75. Ouyang, Q., K. Ishida, and K. Okada, *Investigation of micro-adhesion by atomic force microscopy.* Applied Surface Science, 2001. **169-170**: p. 644-648.
76. Milling, A., P. Mulvaney, and I. Larson, *Direct measurement of repulsive van der Waal's interactions using an atomic force microscope.* Journal of Colloid and Interface Science, 1996. **180**: p. 460-465.
77. Erts, D., et al., *Force interactions and adhesion of gold contacts using a combined atomic force microscope and transmission electron microscope.* Applied Surface Science, 2002. **188**: p. 460.
78. Craig, V.J., *An historical review of surface force measurement techniques.* Colloids and Surfaces, 1997. **129-130**: p. 75-94.
79. Cappella, B. and G. Dietler, *Force-distance curves by atomic force microscopy.* Surface Science reports, 1999. **34**: p. 1-104.
80. Mahanty, J. and B. Ninham, *Dispersion Forces*. 1976, London: Academic Press.
81. Dobson, J. and J. Wang, *Successful test of a Seamless van der Waal's density functional.* Phys. Rev. Lett., 1999. **82**: p. 2123.
82. Dobson, J., et al., *Prediction of Dispersion Forces: Is There a Problem?* Aust. J. Chem., 2001. **54**: p. 513.
83. Kittel, C., *Solid State Physics*. 1996, New York: Wiley & Sons.
84. Cleveland, J.P., et al., *A non-destructive method for determining the spring constant for scanning force microscopy.* Rev. Sci. Instrum., 1993. **64**: p. 403-405.
85. Franco, S., *Electric Circuits Fundamentals*. 1995, Orlando: Harcourt Brace College.
86. Ellis, H., ed. *Book of Data*. Revised ed. Nuffield Advanced Science. 1984, Addison Wesley Longman: Edinburgh Gate.
87. Chang, D., *Field and Wave Electromagnetics*. Second Edition ed. 1989, Massachusetts: Addison-Wesley.
88. Jiles, D., *Introduction to Magnetism and Magnetic Materials*. Second ed. 1998, London: Chapman and Hall.
89. Tholen, A.R. and Y. Yao, *Strain fields at contacts between small particles.* Journal of Colloid and Interface Science, 2003. **268**: p. 362.
90. Wolf, E.L., *Nanophysics and nano technology: an introduction to modern concepts in nanoscience*. 2004, Chichester: Weinheim.
91. Dobson, J., et al., *Soft Cohesive Forces.* International Journal of Quantum Chemistry, 2004: p. 579-598.
92. Kubaschewski, O. and B.E. Hopkins, *Oxidation of Metals and Alloys*. 1962, London: Butterworths.
93. Rydberg, H., et al., *van der Waal's density functional for layered structures.* Physical Review Letters, 2003. **91**: p. 126402.
94. Johnson, K.L., K. Kendall, and A.D. Roberts, Proc. Roy. Soc. London A., 1971. **324**: p. 301.

95. Derjaguin, B.V., V.M. Muller, and Y.P. Toporov, *Effect of Contact Deformations on the Adhesion of Particles.* J. Colloid Interface Sci., 1975. **53**: p. 314.
96. Tabor, D. and R.H.S. Winterton, Proc. Roy. Soc. London A., 1975.
97. Schwarz, U., *A Generalised analytical model for the elastic deformation of an adhesive contact between a sphere and a flat surface.* Surface Science, 2003. **261**: p. 99.
98. Banerjea, A., J. Ferrante, and J. Smith, *Adhesion at metal interfaces*, in *Fundamentals of Adhesion*, L.-H. Lee, Editor. 1991, Plenum: New York. p. 325-348.
99. Ferrante, J. and J. Smith, *Theory of bimetallic interfaces.* Phys. Rev. B, 1985. **31**: p. 3427.
100. Mullins, W., *Theory of thermal grooving.* J. Appl. Phys., 1956. **28**: p. 333.
101. Mullins, W., *Theory of thermal grooving.* J. Appl. Phys., 1957. **28**: p. 333.
102. Mullins, W., *Flattening of a nearly plain solid surface due to capillarity.* J. Appl. Phys., 1959. **30**: p. 77.
103. King, R. and W. Mullins, *Theory of a surface scratch to flatness.* Acta. Metall., 1962. **10**: p. 601.
104. Blakely, J. and H. Mykura, *Studies of vacuum annealed surfaces.* acta. metall., 1963. **11**: p. 399.
105. H'ai, T.O.W. and Y. Kaganovskiy, *Investigation of self diffusion at (100), (110) and (111) surfaces of Copper single crystals by the method of the smoothing out of scratches.* Fiz. metal. metalloved, 1973. **35**: p. 190.
106. Tolmon, F. and J. Wood, J. Sci. Instr., 1956. **33**: p. 236.
107. Bonzel, H. and N. Gjostein, Appl. Phys. Lett, 1967. **258**.
108. Herring, C., in *Physics of Powder Metallurgy*, W. Kingston, Editor. 1951, MacGraw Hill: New York.
109. Herring, C., *The use of classical macroscopic concepts in surface-energy problems*, in *Structure and Properties of Solid Surfaces*, R. Gomer and C. smith, Editors. 1953, University of Chicago Press: Chicago. p. 5-71.
110. Neumann, G. and G.M. Neumann, *Surface Self-Diffusion*. Diffusion Monograph Series. Vol. 1. 1972, Ohio: Diffusion Information Centre. 61.
111. Tritscher, P. and P. Broadbridge, *Grain boundary grooving by surface diffusion: an analytic nonlinear model for a symmetric groove.* Proc. R. Soc. Lond. A., 1995. **450**: p. 569.
112. Blakely, J. and H. Mykura, *Surface diffusion measurements on Nickel by mass transfer method.* Acta. Metall., 1961. **9**: p. 23.
113. McCormick, N., *Confocal scanning optical microscopy*, in *Surface Characterisation*, D. Brune, Editor. 1997, Scandinavian Science Publisher: Weinheim. p. 57-76.
114. Hamilton, D. and T. Wilson, *Surface Profile Measurement using the confocal microscope.* Journal of Applied Physics, 1982. **53**: p. 5320.
115. Whitlow, H., *Reference data tables*, in *Surface Characterisation: A users source book*, D. Brune, Editor. 1997, Scandinavian Science Publisher: Weinheim. p. 32-52.
116. Willson, T., *Confocal Microscopy*. 1990, London: Academic Press. 1-21.
117. Zapuskalov, N. and R. Dippenaar. *In-situ observation of microtopography of metal surface at elevated temperature*. in *The Brimacombe Memorial Symposium Poster Proceedings*. 2000. Vancouver, British Columbia, Canada: METSOC.

118. Zapuskalov, N. and R. Dippenaar, *Determination of surface diffusion by in-situ observation*. 2001, University of Wollongong: Wollongong.
119. McLean, D., *Mechanical Properties of Metals*. 1962, New York: John Wiley & Sons.
120. Nii, K. and K. Yoshihara, *The effect of oxygen potential on the surface self-diffusion of α–Iron.* Transactions JIM, 1979. **20**: p. 523.
121. Jr., L.B.S., *On the fundamental nature of metal-metal adhesion.* Trans. ALSE, 1977. **21**: p. 285.
122. Yoon, E.-S., et al., *The effect of contact area on nano-micro scale friction.* Wear, 2005. **259**: p. 1424.
123. Isrealachvili, J., *Skimming the Surface.* Nature, 2005. **435**: p. 893.
124. Luan, B. and M. Robbins, *The breakdown of continuum models for mechanical contacts.* Nature, 2005. **435**: p. 929.
125. Easterling, K.E. and A.R. Tholen, *A study of sintering using hot-stage electron microscopy.* Metal Science Journal, 1970. **4**: p. 130.
126. Easterling, K.E. and A.R. Tholen, *Surface energy and adhesion at metal contacts.* Acta Metallurgica, 1972. **20**: p. 1001.
127. Mesarovic, S.D. and K.L. Johnson, *Adhesive contact of elastic-plastic spheres.* Journal of the Mechanics and Physics of Solids, 2000. **48**: p. 2009.
128. Jernot, J., et al., *Sintering Diagrams for Cobalt, Nickel and Iron.* Mat. Res. Bull., 1982. **17**: p. 815.
129. Frost, H.J. and M.F. Ashby, *Deformation mechanism maps: The plasticity and creep of metals and ceramics*. 1982, Oxford: Pergamon Press. 60-63.
130. MOON, S.-C., *The influence of austenite grain size on hot ductility of steels*, in *Materials Engineering*. 2003, University of Wollongong: Wollongong.
131. Honeycombe, R.W.K. and H.K.D.H. Bhadeshia, *Steels: Microstructure and Properties*. second ed. Metallurgy and Materials Science, ed. R.W.K. Honeycombe and H.K.D.H. Bhadeshia. 1995, Oxford: Butterworth and Heinemann.
132. Cheng, D., *Field and Wave Electromagnetics*. Second Edition ed. 1989, Massachusetts: Addison-Wesley.
133. Smithells, C.J., ed. *Metals reference book*. Plenum Press: New York.
134. Sargent, L., *On the fundamental nature of metal-metal adhesion.* Trans. ASLE, 1977. **21**: p. 285.
135. Kumikov, V.K. and K.B. Khokonov, *On the measurement of surface free energy and surface tension of solid metals.* J. Appl. Phys., 1983. **54**: p. 1346.
136. Kumikov, V.K., *The measurement of the surface tension of some pure metals in the solid state.* Materials Science and Engineering, 1983. **60**: p. L23-L24.
137. Blundell, D., *The agglomeration of iron ore particles in a fluidised bed cascade*, in *Materials Science*. 2005, University of Wollongong: Wollongong.